Schweizerische Eidgenossenschaft
Confédération suisse
Confederazione Svizzera
Confederaziun svizra

Eidgenössisches Departement des Innern EDI
**Bundesamt für Meteorologie und Klimatologie MeteoSchweiz**

**Veröffentlichung MeteoSchweiz Nr. 87**

# Ensemble Simulations of Convective Storms

*Manuel Bischof*

**Herausgeber**
Bundesamt für Meteorologie und Klimatologie, MeteoSchweiz, © 2011

MeteoSchweiz
Krähbühlstrasse 58
CH-8044 Zürich
T +41 44 256 91 11
www.meteoschweiz.ch

**Weitere Standorte**
CH-8058 Zürich-Flughafen
CH-6605 Locarno Monti
CH-1211 Genève 2
CH-1530 Payerne

**Veröffentlichung MeteoSchweiz Nr. 87**

**ISSN: 1422-1381**

# Ensemble Simulations of Convective Storms

***Manuel Bischof***

**Masterarbeit**

**Betreuung**
Dr. Daniel Leuenberger, MeteoSchweiz
Prof. Dr. Heini Wernli, Institut für Atmosphäre und Klima, ETH

**Bitte zitieren Sie diese Veröffentlichung folgendermassen**
Bischof, M: 2011, Ensemble Simulations of Convective Storms, *Veröffentlichungen der MeteoSchweiz*, **87**, 120 pp.

**Herausgeber**
Bundesamt für Meteorologie und Klimatologie, MeteoSchweiz, © 2011

MeteoSchweiz
Krähbühlstrasse 58
CH-8044 Zürich
T +41 44 256 91 11
www.meteoschweiz.ch

**Weitere Standorte**
CH-8058 Zürich-Flughafen
CH-6605 Locarno Monti
CH-1211 Genève 2
CH-1530 Payerne

# Abstract

This study presents ensemble simulations of idealized convective storms with the non-hydrostatic atmospheric COSMO model. Wind speed, temperature and humidity of the environmental sounding are perturbed for the ensemble generation. The impact of different perturbation amplitudes on the storm structure and evolution in the individual ensemble members and the resulting statistical ensemble characteristics are investigated. It was found that all three variables are suited for perturbation. Perturbations in the wind profile lead to differences in the vertical vorticity, which determine the storm structure, whereas temperature and humidity perturbations affect the convective available potential energy, the updrafts, and the vertical vorticity distribution. A combined perturbation of wind speed and temperature turned out to be particularly useful. The modeling setup, derived in this study, is judged as a suitable testbed for ensemble data assimilation methods, such as the Ensemble Kalman Filter.

# Contents

**1 Introduction** **4**
1.1 Numerical Weather Prediction and Ensemble Forecast . . . . . 6
1.2 Basic Concepts of Convective Storms . . . . . 8
1.3 Idealized Simulations of Convective Storms . . . . . 14
1.4 Aims of this Study . . . . . 15

**2 Methods** **16**
2.1 The COSMO Model . . . . . 16
2.2 Experimental Setup . . . . . 17
2.3 Ensemble Verification Tools . . . . . 23

**3 Results** **25**
3.1 Nature Run . . . . . 25
3.1.1 Initial Stage . . . . . 25
3.1.2 Secondary Storm Development . . . . . 27
3.1.3 Vertical Storm Structure . . . . . 29
3.1.4 Surface Winds and Accumulated Precipitation . . . . . 31
3.2 Ensemble Simulations . . . . . 34
3.2.1 Horizontal Wind Perturbation . . . . . 35
3.2.2 Temperature Perturbation with Constant Relative Humidity . . . . 44
3.2.3 Temperature Perturbation with Constant Specific Humidity . . . . 50
3.2.4 Relative Humidity Perturbation with Constant Temperature . . . . 55
3.2.5 Combined Temperature and Wind Speed Perturbation . . . . . 57
3.2.6 Comparison of Ensembles . . . . . 60
3.2.7 Additional Nature Runs . . . . . 64

**4 Summary and Conclusion** **66**

**5 Acknowledgments** **69**

**References** **I**

**Appendix** **III**

# 1 Introduction

Convective storms are frequent weather phenomena which can reach from harmless convective cells over powerful and dangerous multicell storms to highly severe and devastating supercell storms. They can be accompanied by heavy rainfall, strong winds, damaging hail, or even destructive tornadoes. Intensive convective storms can thus be a threat to human life and property (see Figure 1).

Although convective storms occur frequently, have a major impact on society, and have been subject of very active research in the last decades, it is still an extremely difficult task to predict their occurrence and intensity. This is partly due to the fact that numerical weather prediction (NWP) models still have difficulties to adequately simulate convective storms (see web page [21]) because of

- the non-linear and chaotic atmospheric flow across a wide range of scales, highly complex microphysical processes occurring in the subgrid scale, and the sensitivity to many parameters so that even small errors in the initial conditions can have a large impact on the storm development at later times

- model errors as a result of numerical inaccuracies and uncertain parameterizations

- inaccurate specification of external parameters such as soil properties or orography due to limited numerical resolution or missing observations of these quantities

- inaccurate specification of the model's initial state due to missing or inexact observations of the atmosphere and inappropriate data assimilation methods to feed the observations to the model

Figure 1: A tornado destroyed the city Joplin, Missouri U. S., May 22, 2011 (from [23])

Therefore, numerical models are steadily developed, their spatial resolution is increased, and data assimilation methods are improved to allow a better usage of modern observations, such as radar and satellite observations, which lead to a more accurate initial model state. Moreover, the steadily increasing computational power nowadays allows an estimation of the uncertainty of numerical simulations by means of ensemble prediction.

Ensemble simulations estimate the probability density of weather events, are useful for improving the accuracy of the average forecasts, and give an estimation of the forecast skill as a function of forecast lead time (e.g. Sivillo et al., 1997). The ensemble spread as a forecast error estimate is also successfully used in ensemble data assimilation, such as the Ensemble Kalman Filter (EnKF), for the optimal combination of a short model forecast and observations based on their error statistics (Evensen, 1994). The resulting ensemble provides the atmospheric fields to initialize the ensemble forecasts. The main difficulty, particularly in storm-scale applications, is the production of an ensemble with statistics that appropriately represent actual forecast uncertainty and the maintenance of the ensemble spread in order that data assimilation stays successful over time (Dowell and Wicker, 2009).

In the current thesis, an attempt is made to enhance the knowledge of numerical ensemble simulations of convective storms in an idealized setting in order to

(i) gain a better understanding of the sensitivity of such simulations to different ensemble perturbations, and

(ii) provide a testbed for future ensemble assimilation methods.

To this end, ensemble simulations of idealized convective storms using different perturbations are investigated with an operational NWP model.

Section 1.1 provides the basic ideas of ensemble forecasting following Buizza (2000), Wallace and Hobbs (2006), and Weigel (2011). In Section 1.2, the basic principles of convective storms will be briefly summarized, mainly based on the more detailed discussion in Wallace and Hobbs (2006).

## 1.1 Numerical Weather Prediction and Ensemble Forecast

The weather plays a key role for life on this planet, affecting the nature as well as social and economical aspects of the society. Therefore, weather forecasting has become more and more important in the past century. From meteorology, which was based solely on experience and intuition, it evolved into a whole science including theory, numerical modeling and the development of sophisticated observing systems. Although considerable progress could be made, it is still extremely difficult to predict the weather adequately for a longer period. The reason lies in the complexity of the atmosphere consisting of different gases, liquid and solid water droplets, and aerosols. All of them obey physical laws and are influenced by many different physical processes on a wide range of scales. Therefore, the atmosphere is a chaotic and highly nonlinear system and has a nearly infinite number of degrees of freedom. Such a system can be extremely sensitive to disturbances. For instance, even small errors in the initial conditions can grow over weeks and influence or completely dominate the weather evolution. Thus, it is impossible to predict the atmospheric motion accurately over a few weeks.

The chaotic behavior of the atmosphere was first studied by Edward N. Lorenz in the 1960s when he experimented with simple atmospheric models at MIT. By rerunning one experiment that forecasts the weather for several days, he got completely different outputs although he used the same experimental setup. In fact, he was not able to duplicate his weather forecast. The reason lay in round-off errors of his computer in the last significant digit, as he found later. These errors grew eventually to the magnitude of the variations in the individual model runs. Although the atmosphere is much more complex than the highly simplified model of Lorenz, already a few physical laws are able to explain the system appropriately. These laws include the conservation of mass, momentum, and energy for air and water, and the equation of state. The weather evolution is, therefore, determined approximately by a set of differential equations which build the basis of numerical models.

The advent of numerical models brought a significant increase in weather forecast accuracy. In the 1950s, pioneering work in numerical weather prediction was done by using primitive equation models. Simultaneously to the fast development of computer technologies, the models could be refined and the forecast skill could be improved remarkably. For instance, many physical processes, such as surface and boundary layer processes, radiation, and moist processes, can now be included by parameterization schemes and allow more realistic atmospheric simulations.

A huge amount of global observations, such as surface reports, radiosonde data, flight level and satellite data, can be used to determine the initial conditions for a NWP model. However, these measurements of pressure, temperature, wind, and moisture are sparse in space and time and affected by measurement errors, which lead to uncertainties in the initial conditions. Although such errors can be accounted for observing and data assimilation systems, the remaining uncertainty partially determines the accuracy of the

numerical weather prediction. Another factor limiting the forecast skill is the inability of the models to represent and resolve atmospheric processes, i.e. the so-called model errors. Due to runtime constraints and limited computer resources, the model should not exceed a certain degree of complexity. To summarize, numerical weather prediction will always be affected by uncertainties and initially small errors can amplify rapidly due to the chaotic behavior of the atmosphere.

To estimate the degree of uncertainty of numerical weather forecasts, ensemble simulations start to get computationally feasible. The idea of ensemble simulations is simple: Instead of using the most probable initial conditions as model input and obtain one deterministic forecast, in ensemble forecasting, a sample of possible initial conditions is used to simulate many different forecasts. They provide a sample of the probability distribution of the future atmospheric evolution and, thus, an indicator of forecast uncertainty.

In reality, it is impossible to cover all initial conditions in the uncertainty range. Therefore, it is essential to take a suitable selection of atmospheric states for the initiation. Consequently, ensembles can be generated by proper perturbations of the initial conditions. But in practice, not only the initial conditions, but also the models and boundary conditions are affected by errors. Therefore, different models, varied model parameterization, or perturbed boundary conditions can also be the basis for ensemble simulations.

NWP and ensemble forecasting is especially challenging and interesting for convective systems due to their complexity and nonlinearity. In consideration of the advantages of ensemble forecast, it is not surprising that many researches make use of this powerful tool in order to improve the predictability of convective systems, or convective systems are used as case studies with the purpose of enhancing ensemble forecasts. One difficulty in ensemble simulation is, for instance, to maintain an ensemble spread relatively constant over time, which is important for data assimilation processes (see Section 2.3 for more details about the ensemble spread). For this reason, Dowell and Wicker (2008) developed an additive noise method for initializing ensemble forecasts of convective storms and maintaining significant ensemble spread during data assimilation. It was tested for a simplified numerical cloud model and radar observations of a supercell occurred at Oklahoma City. Snyder and Zhang (2003) examined the potential of the Ensemble Kalman Filter to assimilate radar observations in a cloud-scale model. They used a bubble in a horizontally uniform model environment to initialize supercell storms. The unperturbed simulation was used as a reference run and the ensembles were constructed by adding random observational error to the radial velocity. These observations were assimilated by means of the Ensemble Kalman Filter. The results were satisfactory but they speculated that improving the initial ensemble is important for the Ensemble Kalman Filter at convective scales.

## 1.2 Basic Concepts of Convective Storms

The sun, which is responsible for most weather phenomena, is also the driving mechanism for convective storms. If solar energy is absorbed by the Earth's surface, heat is transferred to the lowest atmospheric layer which gives rise to buoyancy of air masses. This process is called convection. *Shallow convection* is referred to convective air circulations in the lowest 1 or 2 kilometers of the atmosphere, whereas more vigorous convection is called *deep convection*. Large cumulonimbus clouds (Figure 2), reaching up to the tropopause and often causing local heavy rainfall and strong winds, are an indicator of deep convection. Although they cover only a small fraction of the Earth's surface area, most of the rainfall in the tropics and in the summer hemisphere over the continents originates in these deep convective clouds.

The vertical profile of temperature and moisture in the atmosphere are crucial for the development of deep convection. Three conditions are necessary for its occurrence. First, the atmosphere should be conditionally unstable. Second, the boundary-layer should contain a substantial amount of moisture. Third, there must be lifting of air in the low atmosphere as a result of convergence or orography. Figure 3 helps to get a better understanding of these conditions. The atmosphere is conditionally unstable if the ambient temperature decreases faster with height than the temperature of a lifted saturated air parcel but slower than a dry air parcel (i.e., $\Gamma_s < \Gamma \leq \Gamma_d$, where $\Gamma$ represents the environmental lapse rate, $\Gamma_s$ the saturated lapse rate, and $\Gamma_d$ the dry adiabat). Assuming that an air parcel at point O is in equilibrium with its environment and is displaced by some mechanism, such as convergence or orographic lifting, it follows the dry adiabat toward point A. If the driving force ceased, the air parcel would move back toward point O at

Figure 2: Clouds observed over the south China Sea. In the background, cumulonimbus clouds reach up to the tropopause, whereas shallow convective clouds occurred in the foreground. (from Wallace and Hobbs (2006))

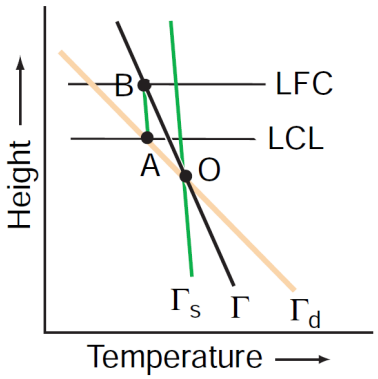


Figure 3: The atmosphere is conditionally unstable if the lapsrate $\Gamma$ is larger than the wet adiabat $\Gamma_s$ and smaller than the dry adiabat $\Gamma_d$ (from Wallace and Hobbs (2006))

any point on this path due to the parcel's lower temperature with respect to the environment. At point A, the parcel arrives at its *lifting condensation level (LCL)*, i.e., the point at which saturation is reached and the water vapor in the parcel starts to condensate. This point marks the bottom edge of a cumulus cloud and is obviously depending on the amount of moisture contained in the air parcel. If the parcel is lifted further, it follows the wet adiabat in this temperature-height plot (Figure 3). The release of latent heat during the condensation of the water vapor yields that the temperature decreases slower with height. At some height, the temperature of the parcel equals the temperature of the environment. This level is called *level of free convection (LFC)*. A small displacement would lead to free convection because the air parcel would be warmer and thus less dense than the environment. In other words, the parcel experiences a buoyant force and rises unhindered. This force is dependent on the temperature difference between the air parcel and its environment, i.e., small temperature differences lead to weaker buoyancy than large differences. The force ceases at the so called *equilibrium level (EL)*. This is the level, at which the temperature of the air parcel equals the environmental temperature again. An inversion layer is essential for the occurrence of this level. If there is no such layer in the troposphere, the parcel rises up to the tropopause where a large inversion layer marks the lower stratosphere. This is the case for deep convection. The different levels are marked in Figure 4.

To sum up, if the atmosphere is conditionally unstable and air is lifted over the level of free convection, convective clouds occur which reach slightly over the equilibrium level. In this case, convection is fed by the potential energy inherent in the moisture and temperature stratification. This energy is called *convective available potential energy (CAPE)*. It is a measure of atmospheric instability and determines the intensity of convection.

However, the CAPE is not the only quantity that is relevant for convective storms. If most of the air parcels reached their LFC, the CAPE would never become large enough to support vigorous deep convection. Therefore, the so-called *convective inhibition (CIN)*

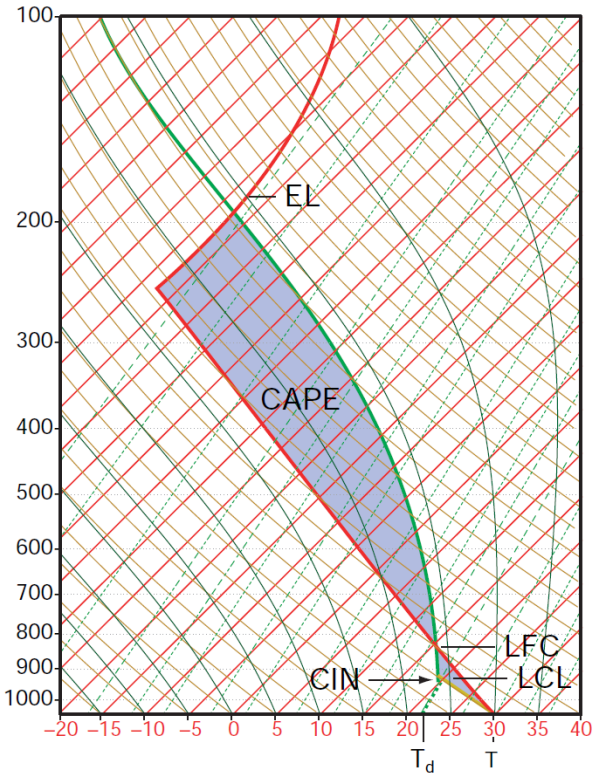


Figure 4: The skew-T log-p diagram shows a hypothetical temperature profile of the environment in red and of an air parcel with its origin at the surface in green. Different levels are sketched, such as the lifting condensation level (LCL), the level of free convection (LFC), and the equilibrium level (EL). The convective available potential energy (CAPE) and the convective inhibition (CIN) are shaded in gray. (from Wallace and Hobbs (2006))

plays a crucial role for convective storms. It describes the energy required to lift an air parcel over its level of free convection, which happens usually due to orography or convective lifting. Orographic lifting occurs if air masses flow over sufficiently high elevations of the surface whereas absorbed solar radiation at the ground gives rise to buoyant air masses, which leads to convective lifting. Therefore, to form convective storms, the CIN has to be overcome by lifting of air and the CAPE has to be large enough to activate deep convection.

The movement, evolution, and structure of convective storms are, additionally, strongly affected by the vertical wind profile. They often form in an environment manifesting a vertical wind shear, i.e., an increasing wind speed with height. Weak shears lead to convective cells, where the downdrafts hinder the updrafts from supplying the storm, whereas strong shears enhance a tilted structure of the storm where the downdrafts and updrafts interact and supply each other which results in more intense, longer lived storms. The speed of these convective storms approximately equals the vertically averaged, mass

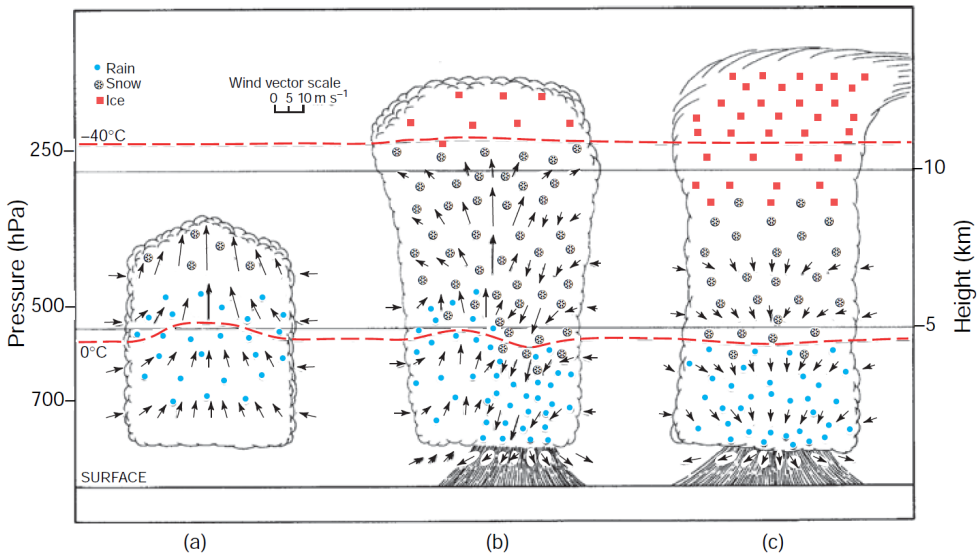


Figure 5: Single cell storm in cumulus stage (a), mature stage (b) and dissipating stage (c). (from Wallace and Hobbs (2006))

weighted, horizontal wind in the environment. Another factor, that influences the dynamics of convective storms, is the change in wind direction with height. These changes are characteristically for a certain class of convective storms, so-called *supercells*.

Convective storms consist of cells which develop in a first stage, when their growth is fed by the midtropospheric CAPE, mature in a second stage, when their tops reach the equilibrium level at the tropopause and build an anvil, and decay finally. Depending on the vertical wind shear, three classes of convective storms can be differentiated: *single cell storms*, *multicell storms*, and *supercell storms*.

*Single cell storms* are formed in an environment with weak vertical wind shear when local convection produces one cell with a single updraft and downdraft which leads to one main precipitation shower. Figure 5 illustrates schematically the evolution of such a single cell storm. In the cumulus stage (a), warm air rises due to the buoyant force. In these updrafts, large vertical velocities can be reached. After some time, large raindrops are formed and start to fall. Their drag force leads to vigorous downdrafts and heavy precipitation that is characteristic for the mature stage (b). In the dissipating stage (c), the top of the cloud has reached the tropopause and starts to form an anvil. At the same time, the downdrafts have occupied the entire cloud and the updrafts, which fed the storm, cease. This self-destructive mechanism implies a short lived single cell storm. It rarely produces strong winds or hail.

The more severe and longer-lived *multicell storms* develop in a stronger vertical wind

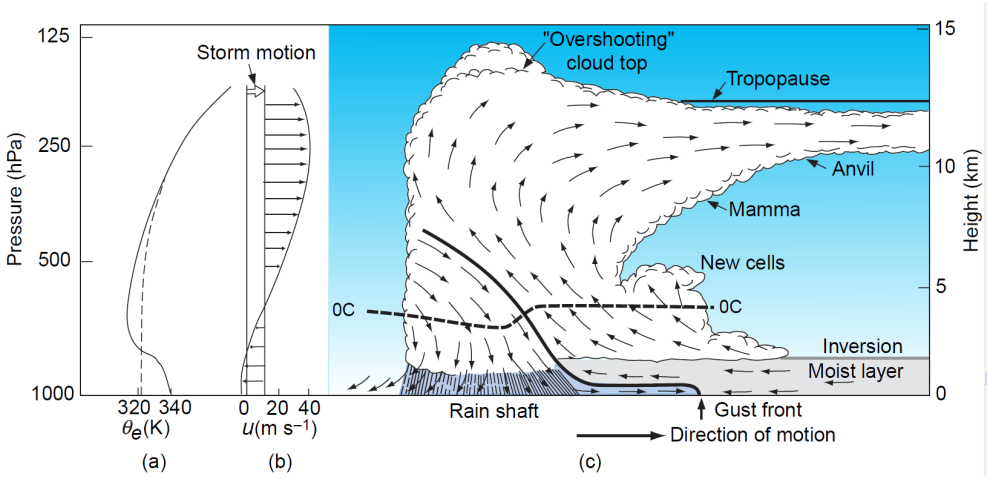


Figure 6: Sketch of a multicell storm. Panel (a) shows a vertical profile of equivalent potential temperature and panel (b) the wind profile which exhibits a strong vertical shear. The arrows in panel (c) indicate the air motion relative to the moving storm. (from Wallace and Hobbs (2006))

shear environment. They consist of many single cells which develop and decay in their own cycles and support the development of new cells, each with a lifetime of about 30 minutes. The vertical wind shear strength defines the degree of organization between the single cells contained in a multicell storm. In a strong wind shear environment, the single cells are tightly integrated in the larger scale entity. New cells form preferably along the so called *gust front*, a cool and dense outflow of air diverging from the base of the downdraft, because it lifts warm moist boundary-layer air over the level of free convection. These new formed cells sustain the multicell storm. Figure 6 shows the schematic dynamics of a multicell storm. Dry environmental air with low wet bulb temperature enters the storm from the rear at middle levels. Due to this inflow, precipitation particles evaporate partly and cool the air. Hence, it experiences a downward buoyant force. This downdraft is even enhanced by the frictional drag of the precipitation particles. At the front, air is lifted and experiences a positive buoyant force which leads to strong updrafts. At the tropopause, the upcoming air diverges and builds a large anvil that can extend over 100 kilometers. This huge cloud can be seen from far away, but the gust front does not arrive before a sudden wind shift and temperature drop can be sensed by an observer. Heavy precipitation and possibly hail follow a few minutes later.

Even stronger wind shear environments favor the development of splitting *supercell storms* with rotating updrafts. Characteristic is the formation of a mesolow (a pressure minimum) within the updraft. Due to increasing rotation with height, a pressure gradient develops which implies an enhancement of the updrafts. This process is responsible for the higher intensity and longer lifetime of supercells compared to multicell storms. The acquirement of rotation can be understood by means of the vertical environmental wind

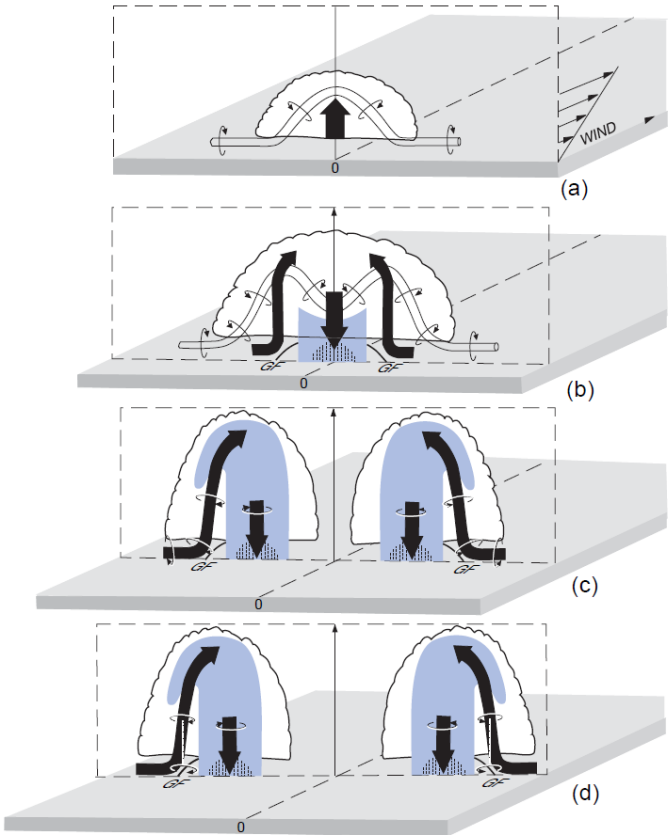


Figure 7: Splitting of a multicell storm into two moving supercell storms. Downdrafts and updrafts are represented by the black arrows whereas the thin tube denotes a cylinder of boundary layer air parcels. The gray shades show radar echoes. (from Wallace and Hobbs (2006))

shear and the associated horizontal vorticity. Updrafts cause vertical movement of boundary layer air which tilts this horizontal vorticity transforming it into vertical vorticity as illustrated in Figure 7(a). The storm develops two symmetric cells rotating clockwise and counterclockwise, respectively. These vortices in the midlevel build up additional pressure gradients which are displaced from the middle and thus widen the updraft (Figure 7(b)). Eventually, the storm splits into two counter-rotating supercell storms (Figure 7(c)). If there is veering in the horizontal wind with height, the two cells do not evolve equally, but one storm is reinforced while the other is suppressed. Supercell storms bring heavy rainfall, strong winds, destructive hail, and even tornadoes can occur.

## 1.3 Idealized Simulations of Convective Storms

In the late 70s and early 80s, the dynamic character of convective storms was started to be investigated by means of numerical simulations in simplified experimental setups. Weisman and Klemp (1982) described the effects of vertical wind shear and buoyancy on the structure and evolution of convective storms and identified these quantities as important in characterizing their dynamics. They found that weak vertical wind shear leads to the development of short-lived single cells, whereas low to moderate shears produce secondary developments, as observed in multicells, and moderate to high shears form split storms which is characteristic for supercells. The ratio of buoyant energy to vertical wind shear determines the basic features of the particular storm structures. Furthermore, the rotation of wind direction with height has a strong influence on the evolution of the storms. Supercells and multicells often emerge from the same split storm depending on the directionally varying wind shears (Weisman and Klemp, 1984).

Since computational capabilities have grown remarkably in the last decades, more complex and higher resolution models can nowadays be used for simulating convective storms. Fiori et al. (2010) investigated deep moist convective processes of supercell storms with the COSMO model in a cloud-scale ($0.1-1$ km grid spacing) simplified experimental setup. They showed that for an appropriate storm simulation, not only the grid resolution defines the storm structure but, in combination, a suitable turbulence parameterization has to be chosen.

However, not only the structure and evolution of convective storms have been studied, but also their occurrence and initialization have been elaborated in more detail. Morel and Senesi (2001) investigated the relationship between European mesoscale convective systems development and environmental conditions by using satellite information. They tracked many convective storms and found that the convective trigger is strongly correlated with orography. Many mesoscale convective systems are observed nearby mountain ranges which leads to the conclusion that orographic lifting is a dominant source of triggering. Furthermore, they showed that most initializations of these convective storms occur around 3 pm local solar time and the storms last about 5.5 hours. Mountain barriers act not only as trigger, but also interfere with the airflow such that mesoscale convective systems have not enough time and space to develop to large and highly destructive storms, as found in the Midwestern United States and the Great Plains (Schiesser et al., 1994).

## 1.4 Aims of this Study

The current thesis investigates the development and structure of a convective storm, typical for Swiss summer conditions, by using numerical ensemble simulations in an idealized experimental setting. In order to get familiar with the chosen convective storm and the COSMO model, a high-resolution simulation is run with the COSMO model as a first step. Questions of interest in this part of the thesis are how the storm develops and how it can sustain different generations of interacting convective cells. Emphasis is put on precipitation, midlevel vorticity, divergence, and near-surface winds since these are the most relevant quantities related to convection.

In the second and main part of this work, the influence of perturbations in the initial profiles of wind, temperature, and humidity on the convective storm simulations are studied. The main questions here are:

- Which quantities, describing the storm environment, are suitable to be perturbed for ensemble generation?
- How large are meaningful perturbation amplitudes for the different perturbed quantities?
- How do the different perturbations affect the storm development of the individual ensemble members?
- What is the effect on the ensemble mean and spread of accumulated precipitation?
- How do the storm intensities vary among the ensemble members, regarding precipitation and near-surface winds?

To answer these questions, integral and isolated storm characteristics, such as accumulated areal precipitation, maximum precipitation intensity, the size of the precipitation area, maximum wind gusts, and the temporal storm evolution at specific points within the storm track are examined during 5 hours of simulation. All results give an idea of the predictability of convective storms. Ensemble members help to estimate the accuracy of the simulations by evaluating their dispersion and facilitate the determination of quantities affecting the storm development.

In Section 2, the numerical model, the experimental setup, and the diagnosis tools are introduced. The results of the simulations are presented and discussed in Section 3. Section 4 gives a summary and concluding remarks.

# 2 Methods

## 2.1 The COSMO Model

The COSMO model (Doms and Schättler, 2001, Schättler et al., 2009), is a non-hydrostatic, fully compressible, numerical weather prediction model designed for operational and research purposes and was developed in 1998 at Deutscher Wetterdienst (DWD). It is based on the primitive thermo-hydrodynamical equations, describing the compressible flow in a moist atmosphere and features parameterizations for a variety of subgrid physical processes important for the simulation of severe weather events on scales from 500 m to 50 km. On these scales, nonhydrostatic effects start to have a major influence on the evolution of the atmospheric flow. Together with a number of additional components, such as data assimilation or chemical transport schemes, the COSMO model is run operationally for numerical weather prediction in Germany, Switzerland, Italy, Greece, Poland, Romania, and Russia. These countries build the *Consortium for Small-Scale Modelling* (COSMO) and help to improve and maintain the COSMO model.

The COSMO model includes different time integration algorithms including a 3rd-order Runge-Kutta scheme which has been applied in this thesis. The parameterizations of physical processes include grid-scale precipitation, vertical turbulent diffusion, radiation, shallow convection, deep convection, soil processes, and soil-atmosphere interactions. In the current study, only the grid-scale precipitation and the vertical turbulent diffusion parameterizations are used. The grid-scale precipitation scheme describes the physical processes concerning water phase transitions and aggregation in clouds (condensation, evaporation, sublimation, melting, freezing, deposition, accretion, riming, and shedding) and simulates the prognostic evolution of water vapor, cloud water (cloud droplets smaller than 50 $\mu$m), rain water (liquid-phase spherical drops with non-negligible fall velocity), snow (large rimed ice particles and rimed aggregates), and graupel which allows an explicit simulation of deep convective clouds. The vertical turbulent diffusion simulates processes concerning the turbulent kinetic energy. It includes the transition of turbulence to very small scales. Other available physical parameterizations, such as radiation, moist convection, parameterization of surface fluxes, or soil processes, have been turned off in simulations of this thesis since they are of minor importance for the idealized convective storms. Furthermore, the high resolution model setup implies no need for the subgrid-scale cumulus convection parameterization.

At MeteoSwiss, COSMO-7 and COSMO-2, with a grid spacing of 7 km and 2 km, respectively, are run operationally. The high-resolution model COSMO-2 is able to simulate explicitly severe weather events triggered by deep moist convection, such as supercell thunderstorms, prefrontal squall-line storms, intense mesoscale convective complexes, and heavy snowfall from wintertime mesocyclones.

## 2.2 Experimental Setup

In order to investigate the impact of different perturbations on the convective ensemble storms, the following experimental setup is defined: A highly idealized model setup is chosen in order to keep the simulations as simple as possible. This allows the investigation of the ensemble simulations in a well-defined and controllable model environment. As a first step, a convective storm with a high resolution is simulated to define the model setup, such as the domain size, and the model settings, such as time step or the numerical schemes. This storm is called "nature run" since it serves as reference or "truth" for the ensemble simulations. In a second step, lower resolution ensemble storms are computed by using the same model setup as the nature run and different ensemble perturbations are tested. Several diagnostic measures are computed for the ensembles, such as ensemble mean or spread, and comparisons with the nature run are done.

### Nature Run

For this study, a convective storm is chosen which is representative for Swiss conditions. The storm environment, i.e., the vertical profiles of temperature, pressure, height, relative humidity, and wind speed are extracted from the sounding of Payerne valid at 12 UTC 30 July 2008, right before a severe thunderstorm occurred over Switzerland. The radar images on this day show evidently how convective cells were triggered at the Jura Mountains and the foothills of the Alps and how they started to organize and intensify. Figure 8 shows the radar image at 1430 UTC, i.e., 2.5 hours after the sounding was taken. The storm evolved and grew during this period and moved eastward. It was accompanied by heavy precipitation.

In order to improve the representation of the thermodynamical profile, the input profile for the COSMO model has been slightly moistened in the lower layers according to surface measurements at the same time and at different altitudes in Switzerland such as Säntis (2502 m), Pilatus (2106 m), Napf (1404 m), Lucerne (454 m), and Wynau (422 m). The resulting profile, interpolated to the model levels, is illustrated in Figure 9. The wind direction has been set to 270 ° for every vertical level to get a constant west wind flow in order to simplify the model setup further.

A topographically flat area of 396 km × 300 km with a horizontally homogeneous atmosphere, using the above mentioned profile, builds the environment in the COSMO model for the convective storm simulations. A combined relaxation and radiative lateral boundary treatment allows for a constant forcing at the lateral boundaries with the initial profile while minimizing reflections of waves at the boundaries. These boundary conditions allow to choose a small domain and, thereby, sufficiently controlled boundary effects. In the vertical direction, the model exhibits 64 levels with a gradually increasing distance between the levels. Their smallest separation of $\sim 100$ m is near the surface and increases steadily with height to $\sim 600$ m at 22 km. The horizontal mesh size was chosen

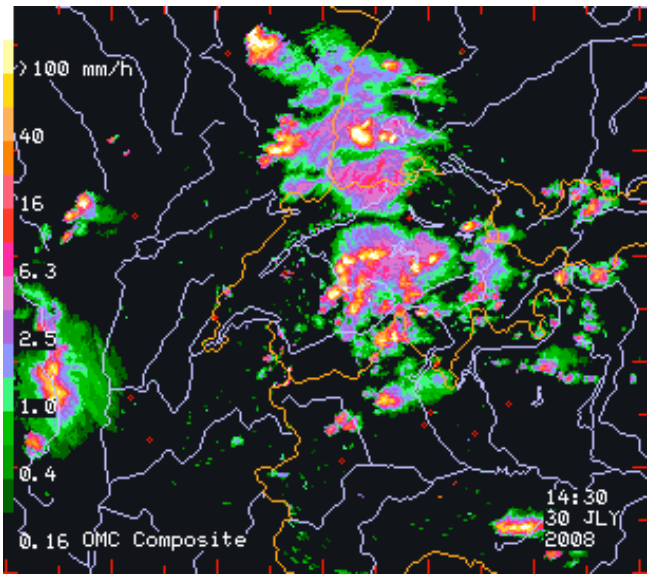


Figure 8: Radar image on 1430 UTC 30 July 2008. Heavy precipitation indicates the intensity of the thunderstorm on this day. (from MeteoSwiss)

to be 1 km for the nature run.

Convection is triggered by an axially symmetric thermal perturbation which decreases gradually to the environmental temperature on the edge. The initiation of convection is similar as in Weisman and Klemp (1982). The artificial warm air bubble describes a three dimensional cosine square shaped disturbance with a maximum temperature excess of 6 K and a size of 30 km × 30 km × 3 km. The center of the bubble is set at 1.4 km above the ground and at the coordinates (90 km | 150.5 km). At time 0, the bubble is released. It raises and triggers convection which leads to the development of the convective storm. The dynamical evolution of several atmospheric quantities, such as horizontal and vertical wind components, temperature, pressure, specific humidity, cloud water content, cloud ice content, specific water contents of rain, snow, and graupel, as well as the total surface amount of rain, snow, and graupel is simulated out to 5 hours. The specific water contents of rain, snow, and graupel are combined to the precipitating hydrometeor content in the atmosphere and, likewise, the sum of the total surface amount of rain, snow, and graupel build the total amount of surface precipitation. The examination of these quantities, representing the convective storms, is topic of Section 3.

### Ensemble Initial Conditions

For the ensemble simulations, the same experimental setup as in the nature run is used except for the horizontal mesh size, which is chosen to be 2 km. This difference in the grid has two reasons: First, the nature run, which is used as reference for the ensemble

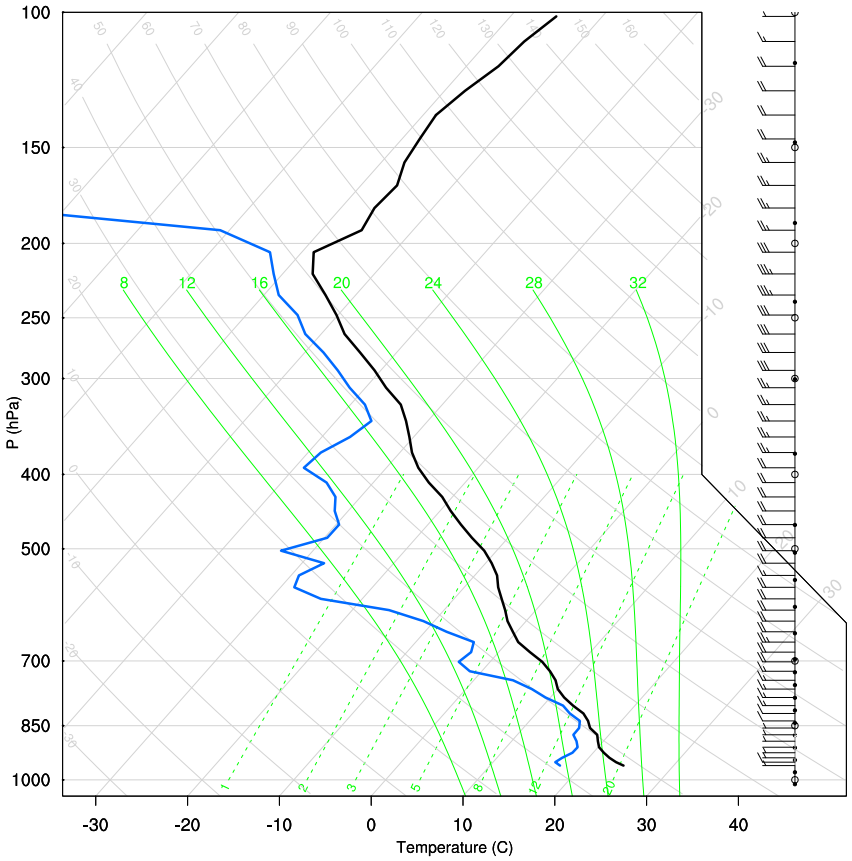


Figure 9: Skew-T log-p diagram representing the vertical profile of temperature (black), dewpoint temperature (blue), and horizontal wind (the wind barbs represent $10\,\mathrm{m\,s^{-1}}$), obtained by interpolating the sounding of Payerne at 12 UTC 30 July 2008 to grid levels. The CAPE amounts $2323\,\mathrm{J\,kg^{-1}}$.

simulations, is simulated with higher precision and differs from the unperturbed ensemble simulation. Second, the coarser grid requires less computational resources.

The ensemble perturbations are chosen to affect the environmental sounding in which the storm develops. The initial profile is disturbed accounting for the uncertainties in the environmental sounding measurement. Following Aksoy et al. (2009), a perturbation $\phi'$ is added to a specific quantity $\phi^0$, such as temperature, horizontal wind speed, or relative humidity to get the profile

$$\phi_i(z) = \phi^0(z) + \phi_i'(z)$$

for each ensemble member $i$, where

$$\phi_i'(z) = \sum_{j=0}^{3} A_{i,j} \cos\left(\varphi_{i,j} + 2\pi j \frac{z}{H}\right)$$

and $H = 20\,\mathrm{km}$. The perturbation is thus a superposition of sinusoidal variations with

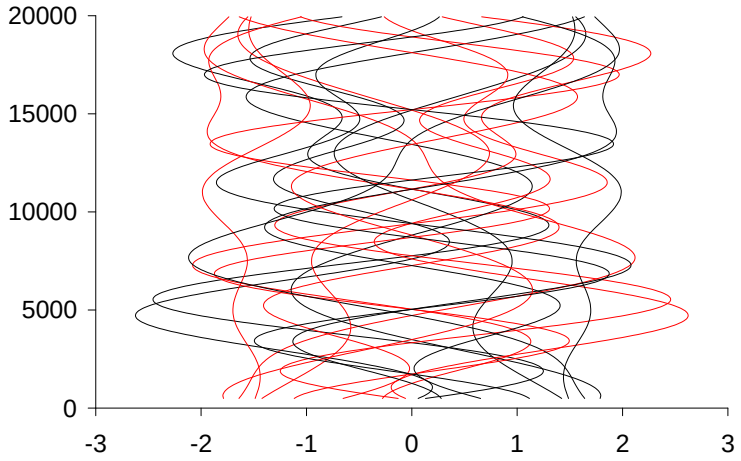


Figure 10: Perturbations in dependence of height of 18 ensemble members with a standard deviation $\sigma_\phi = 1$. The positive perturbation is plotted in black, the corresponding negative perturbation in red. The ordinate represents the height in m, the abscissa shows the perturbation amplitude.

random amplitudes $A_{i,j}$. They are drawn from a Gaussian distribution with zero mean and standard deviation $\sigma_\phi$ and phase shifts $\varphi_{i,j}$ drawn from an uniform distribution in $[0, \pi]$. For each level $k$, the standard deviation

$$\hat{\sigma}_{\phi k} = \sqrt{\frac{1}{N-1}\sum_{i=1}^{N}\left[\phi'_{i,k} - \overline{\phi'_k}\right]^2}$$

is calculated, where N is the number of ensemble members. Then, the perturbations are scaled such that the standard deviation equals $\sigma_\phi$:

$$\phi_{ik} = \phi^0_k + \frac{\sigma_\phi}{\hat{\sigma}_{\phi k}}\phi'_{ik}$$

The perturbation variables $\phi$ include horizontal wind, temperature and humidity. The perturbations are made symmetric such that there is a member with $\phi_i$ and one with $-\phi_i$ ($i = 1...\mathrm{N}/2$) for each ensemble. Figure 10 shows the perturbations of 18 ensemble members with a standard deviation of $\sigma_\phi = 1$. To each positive perturbation (in black), corresponds a negative perturbation (in red).

First, three ensembles were generated with variations in the horizontal wind speed. The standard deviations are chosen according to the order of magnitude in the measurement uncertainties. Second, the temperature profiles are perturbed in a way that either the relative humidity or the specific humidity stayed constant. The former perturbation implies a change in the specific humidity, whereas the latter leads to a change in the relative humidity. Furthermore, three ensembles exhibit a variation in the relative humidity profile at constant temperature. Last, perturbations in horizontal wind and the

temperature are combined. Table 1 shows the 13 ensembles, simulated in this study, with their perturbations and standard deviations. The last two columns exhibit the vertical vorticity and the CAPE with their value ranges. They are important quantities which affect the storm structures and developments. The values show the lowest and highest quantity maxima of all ensemble members.

| **Ensemble** | **Perturbed Quantities** | **Standard Deviation** | **Correlated Quantities** | **Range of Change** |
|---|---|---|---|---|
| ens001 | horizontal wind | $0.5\,\mathrm{m\,s^{-1}}$ | vertical vorticity | $0.00387\,\mathrm{s^{-1}} - 0.00433\,\mathrm{s^{-1}}$ |
| ens002 | horizontal wind | $1\,\mathrm{m\,s^{-1}}$ | vertical vorticity | $0.00364\,\mathrm{s^{-1}} - 0.00463\,\mathrm{s^{-1}}$ |
| ens003 | horizontal wind | $2\,\mathrm{m\,s^{-1}}$ | vertical vorticity | $0.00304\,\mathrm{s^{-1}} - 0.00551\,\mathrm{s^{-1}}$ |
| ens004 | temperature | $0.25\,\mathrm{K}$ | vertical vorticity | $0.00392\,\mathrm{s^{-1}} - 0.00442\,\mathrm{s^{-1}}$ |
| | relative humidity | constant | CAPE | $2013\,\mathrm{J\,kg^{-1}} - 2652\,\mathrm{J\,kg^{-1}}$ |
| ens005 | temperature | $0.5\,\mathrm{K}$ | vertical vorticity | $0.00337\,\mathrm{s^{-1}} - 0.00470\,\mathrm{s^{-1}}$ |
| | relative humidity | constant | CAPE | $1793\,\mathrm{J\,kg^{-1}} - 2948\,\mathrm{J\,kg^{-1}}$ |
| ens006 | temperature | $1\,\mathrm{K}$ | vertical vorticity | $0.00260\,\mathrm{s^{-1}} - 0.00467\,\mathrm{s^{-1}}$ |
| | relative humidity | constant | CAPE | $1123\,\mathrm{J\,kg^{-1}} - 3547\,\mathrm{J\,kg^{-1}}$ |
| ens007 | temperature | $0.1\,\mathrm{K}$ | vertical vorticity | $0.00398\,\mathrm{s^{-1}} - 0.00433\,\mathrm{s^{-1}}$ |
| | specific humidity | constant | CAPE | $2209\,\mathrm{J\,kg^{-1}} - 2370\,\mathrm{J\,kg^{-1}}$ |
| ens008 | temperature | $0.25\,\mathrm{K}$ | vertical vorticity | $0.00371\,\mathrm{s^{-1}} - 0.00453\,\mathrm{s^{-1}}$ |
| | specific humidity | constant | CAPE | $2043\,\mathrm{J\,kg^{-1}} - 2669\,\mathrm{J\,kg^{-1}}$ |
| ens009 | temperature | $0.5\,\mathrm{K}$ | vertical vorticity | $0.00336\,\mathrm{s^{-1}} - 0.00509\,\mathrm{s^{-1}}$ |
| | specific humidity | constant | CAPE | $1967\,\mathrm{J\,kg^{-1}} - 2628\,\mathrm{J\,kg^{-1}}$ |
| ens010 | relative humidity | $2\,\%$ | vertical vorticity | $0.00367\,\mathrm{s^{-1}} - 0.00437\,\mathrm{s^{-1}}$ |
| | temperature | constant | CAPE | $1683\,\mathrm{J\,kg^{-1}} - 2330\,\mathrm{J\,kg^{-1}}$ |
| ens011 | relative humidity | $4\,\%$ | vertical vorticity | $0.00310\,\mathrm{s^{-1}} - 0.00444\,\mathrm{s^{-1}}$ |
| | temperature | constant | CAPE | $1680\,\mathrm{J\,kg^{-1}} - 2981\,\mathrm{J\,kg^{-1}}$ |
| ens012 | relative humidity | $6\,\%$ | vertical vorticity | $0.00273\,\mathrm{s^{-1}} - 0.00452\,\mathrm{s^{-1}}$ |
| | temperature | constant | CAPE | $1054\,\mathrm{J\,kg^{-1}} - 2973\,\mathrm{J\,kg^{-1}}$ |
| ens013 | horizontal wind<br>temperature<br>relative humidity | $1\,\mathrm{m\,s^{-1}}$<br>$0.25\,\mathrm{K}$<br>constant | vertical vorticity<br><br>CAPE | $0.00379\,\mathrm{s^{-1}} - 0.00443\,\mathrm{s^{-1}}$<br><br>$2013\,\mathrm{J\,kg^{-1}} - 2652\,\mathrm{J\,kg^{-1}}$ |

Table 1: List of ensemble simulations. The perturbations were applied to the horizontal wind, temperature, and relative humidity profiles and scaled in a way that all ensemble members exhibit a certain standard deviation which is an indicator of the perturbation strength. The perturbations influence different quantities which have an effect on the storm development. The determining quantities are mentioned in column 4 with their maximal value range within the ensemble members in column 5.

## 2.3 Ensemble Verification Tools

In order to determine the appropriateness of an ensemble, different verification tools are common to use. The most important quantity, concerning ensemble forecasts, is the reliability of an ensemble. A reliable ensemble gives a probability distribution that matches the frequencies of observed outcomes (Weigel, 2011). In this study, the reliability is, however, difficult to determine, because the idealized experimental setup does not exhibit a real observation and the ensembles are not tested for a variety of cases. As a consequence, it is not focused primarily on simulating a large number of ensembles in order to get meaningful statistics, but it is tried to find ensembles that result in reasonable convective storms. For this purpose, useful verification tools are selected.

### Ensemble Spread and RMS

A common measure for the predicted uncertainty and the ensemble dispersion is the ensemble spread (Weigel, 2011). Following Aksoy et al. (2009) the domain-mean ensemble spread $\langle s^f \rangle$ of an ensemble f is defined by

$$\langle s^f \rangle = \sqrt{\frac{1}{M} \sum_{i=1}^{M} \left[ \frac{1}{N-1} \sum_{j=1}^{N} \left( x_{i,j}^f - \overline{x}_i^f \right)^2 \right]}$$

The ensemble contains N members, where $x_{i,j}^f$ represents the i$^{\text{th}}$ forecast of member $j$ and $\overline{x}_i^f$ the ensemble mean of the i$^{\text{th}}$ forecast. M represents the number of forecasts within a certain domain, which are mostly a number of grid points in this study.

In contrast to the ensemble spread, which contains no information about the observation, the root mean square error of the ensemble mean (RMS) is used for the forecast accuracy (Weigel, 2011). It is defined as

$$\langle r^f \rangle = \sqrt{\frac{1}{M} \sum_{i=1}^{M} \left( y_i^f - \overline{x}_i^f \right)^2}$$

with the observation $y_i^f$ corresponding to the ensemble mean $\overline{x}_i^f$. In this study, the observation is taken from the nature run interpolated to the 2 km grid. For reliable ensemble it has been argued that the spread and RMS are correlated, i.e., a high uncertainty in the prediction implies a large deviation between the ensemble mean and the observation and vice versa. Hamill et al. (2004), however, showed, that the so-called *spread-skill relationship* is not always a good measure of ensemble quality.

### Box Plots

An appropriate method for visualizing ensembles are box plots. They allow a quick overview over the distribution of ensemble members and their spread. The diagram exhibits boxes with their so-called whiskers, representing five values concerning the ensemble statistics. The box includes three lines: the upper quartile at the top, the median, and the lower quartile at the bottom. The upper quartile marks the value, which is larger than the value of 75% of the ensemble members, whereas 25% of the data are less or equal than the lower quartile. The median divides the data into two equal parts. The ensemble maximum and minimum values define the outermost points of the whiskers. Box plots contain much information about the ensemble distribution. By definition, 50% of the data lie within the boxes and the length of the box is thus a measure for the spread. Figure 11(a) shows a tiny box which is correlated to a small spread compared to Figure 11(b) whose data exhibits a large dispersion. For a symmetric distribution of the ensemble data, the median is located in the middle of the box (Figure 11(c)) whereas a displacement of the median indicates the skewness of the data (Figure 11(d)). Long whiskers are a sign for outliers as illustrated in Figure 11(e). The reference value is marked by a red circle whereas the full blue circle represents the ensemble mean. In contrast to the boxes, which are independent of extreme values, the ensemble mean is affected by outliers and its position has to be taken carefully, as a consequence.

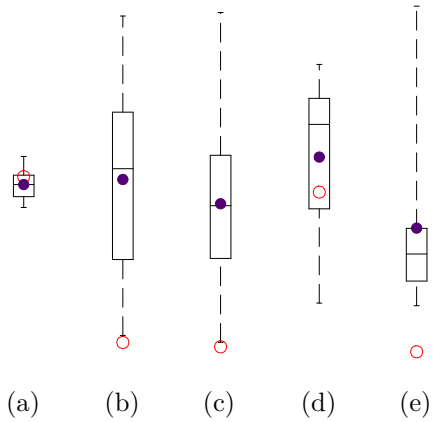


Figure 11: Box plots are a useful tool to visualize the distribution of an ensemble. The size of the box is an indicator of the spread of an ensemble, i.e., small boxes represent small spreads (a) and big boxes large spreads (b). The median exhibits information about the skewness of an ensemble as shown in (c) and (d) and the whiskers illustrate extreme values (e).

# 3 Results

## 3.1 Nature Run

The nature run is a convective storm, simulated with the COSMO model in the horizontally homogeneous environment described in Section 2.2. It serves as control run for later ensemble simulations and exhibits much information about the evolution and structure of the convective storm.

### 3.1.1 Initial Stage

The initial convective cell is triggered by a warm air bubble, resulting in a single cell with an updraft of over $40\,\mathrm{m\,s^{-1}}$. Figure 12 shows a vertical cross-section through the center of the cell at $y = 151\,\mathrm{km}$, illustrating a significant amount of precipitating hydrometeors contained in the cumulus cloud above 6 km after 27 minutes of the simulation (shaded in

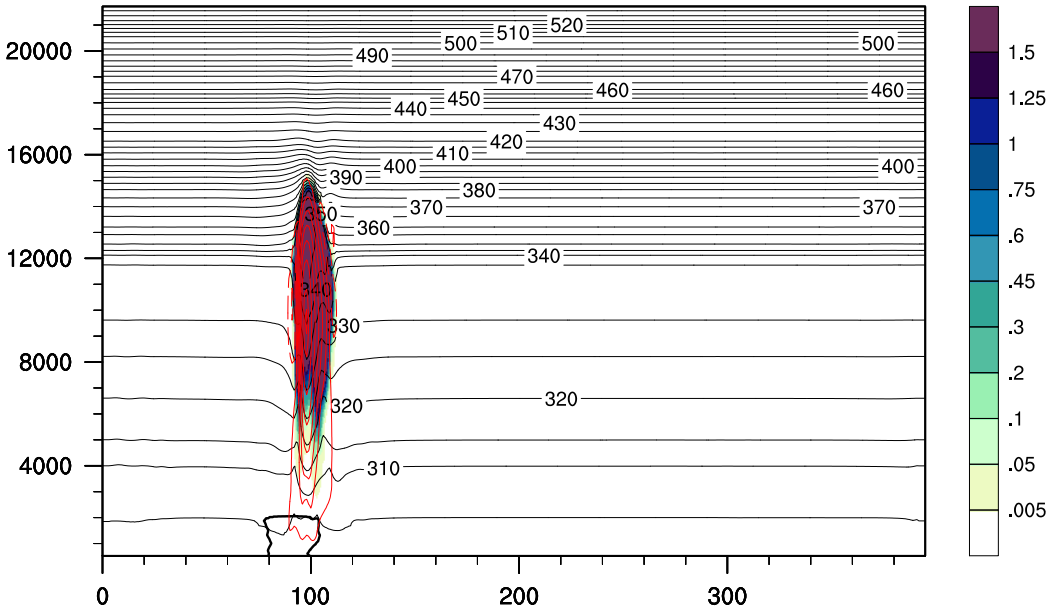


Figure 12: Vertical slice through the center of the storm at $y = 151\,\mathrm{km}$ after $27\,\mathrm{min}$ of simulation. The ordinate represents the height in units of m and the abscissa exhibits the x-direction of the area in kilometers. The color contours denote the water, snow, and graupel content in the atmosphere in units of $\mathrm{g\,kg^{-1}}$ and the vertical wind speed is denoted by red contours (contour spacing of $6\,\mathrm{m\,s^{-1}}$). The thin black lines correspond to isolines of potential temperature whereas the thick black solid line marks a surface temperature anomaly of $-0.5\,\mathrm{K}$. The single cell with the strong updraft and the overshooting top is nicely illustrated.

purple). The isolines of potential temperature indicate the unstable troposphere, where the separation of the isolines is large, and the stable stratosphere above 12 km. The condensation of the moist warm air leads to a release of latent heat and, thus, to an increased potential temperature within the convective cloud. Moreover, an overshooting top, i.e., air rising over the tropopause due to buoyant energy, is prominent. The updrafts reach up to an altitude of 15 km. The cell has already moved about 10 km in x-direction due to the vertical shear of the horizontal wind. This shear has, however, not only an influence on the movement of the cell but also on the vertical component of the vorticity. The strong updrafts convert the initially horizontal vorticity into vertical vorticity. Figure 13 shows the vertical vorticity distribution at 4242 m shaded in blue (negative) and red (positive), the relative horizontal wind at the same height (the initial horizontal wind flow has been subtracted), and vertical wind contours in red at 4600 m. The division of the initial cell into two counter-rotating parts is nicely visible. Another feature that attracts attention is the ellipsoidal shape of the updraft cell which indicates the ongoing splitting of the cell.

After 39 minutes of simulation, the vertical wind speed reaches its maximum of $44\,\mathrm{m\,s^{-1}}$ but, at the same time, the downdraft is enhanced to wind speeds of $-26\,\mathrm{m\,s^{-1}}$ due

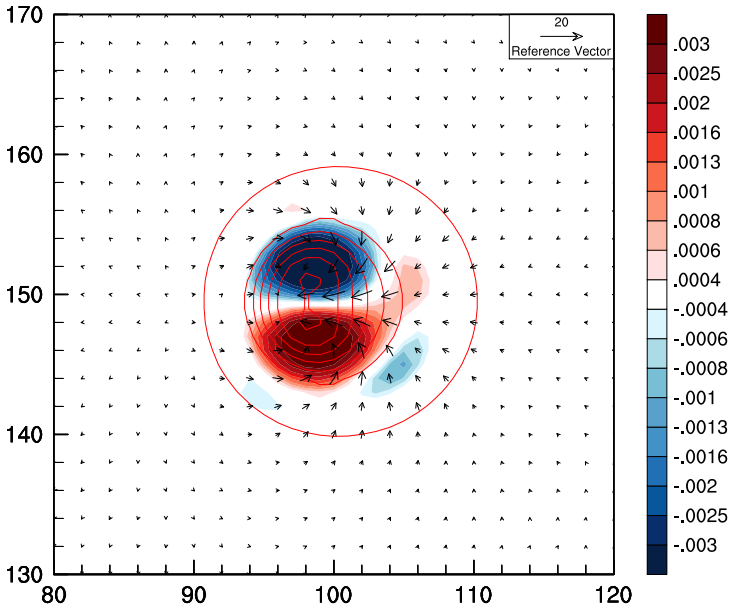


Figure 13: Horizontal view of the storm after $27\,\mathrm{min}$. The axes represent grid points in units of km and show a detail of the whole area of $396\,\mathrm{km} \times 300\,\mathrm{km}$. The vorticity at $4242\,\mathrm{m}$ is shaded in red and blue in units of $\mathrm{s^{-1}}$, the vectors stand for the horizontal wind at the same height, and the vertical wind speed at $4600\,\mathrm{m}$ is denoted by the fine red contours with a separation of $3\,\mathrm{m\,s^{-1}}$. The plot illustrates the two counter-rotating parts of the single cell.

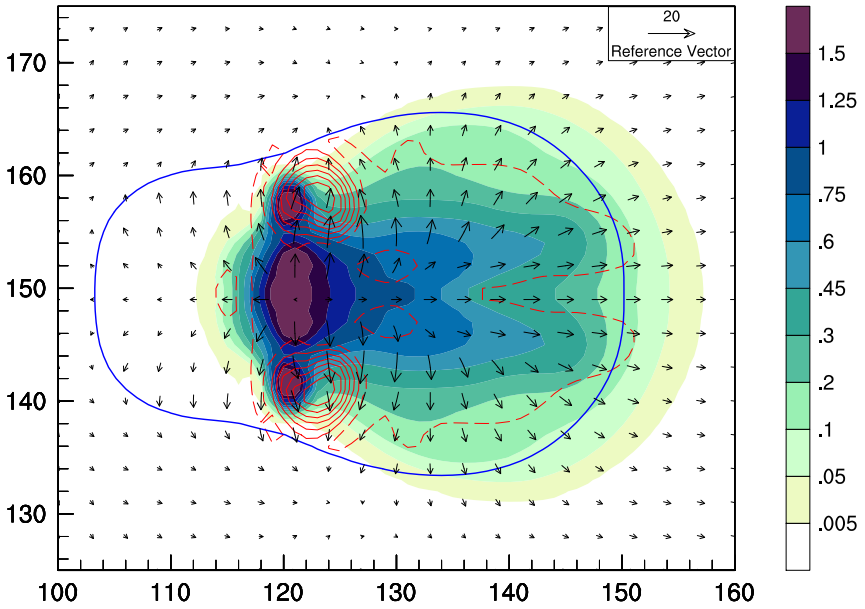


Figure 14: Horizontal storm structure after $90\,\mathrm{min}$ of simulation. The axes are grid points in units of km and the filled contours represent the rain, snow, and graupel content in the lowest atmospheric level in units of $\mathrm{g\,kg^{-1}}$. The wind vectors stand for the horizontal wind at the same level whereas the red solid (dashed) lines denote the positive (negative) vertical wind speed at $4600\,\mathrm{m}$ with a separation of $3\,\mathrm{m\,s^{-1}}$. The cold air pool is shown by the blue line which marks a surface temperature anomaly of $-0.5\,\mathrm{K}$.

to the drag force of heavy grown precipitating hydrometeors. These particles reach the ground as precipitation about 50 minutes after the initiation. The precipitation reaches its maximal intensity at the base of the convective cell. Meanwhile, the cell diverges at the tropopause and forms an anvil. Figure 14 shows the storm after 90 min. Heavy rainfall occurs at the surface and the initial cell is split into two updraft cells (red contours). At the front, downdrafts, which lead to strong outflows at the surface (wind vectors), dominate the storm structure. These downdrafts bring cold air from midlevels to the ground and, together with evaporative cooling in the precipitation areas, they lead to a cold pool which spreads out following the outflow. This negative temperature anomaly of $-0.5\,\mathrm{K}$ is indicated by the solid blue line. The outflow of cold air leads to convergence along the edge of the cold pool, the so-called gust front, which is nicely displayed by the blue contours in Figure 15. Large divergence occurs preferably at the locations of heavy precipitation. The outflow shows, furthermore, a slight wavelike structure.

### 3.1.2 Secondary Storm Development

The convergence along the gust front is essential for new cell development. The cold outflowing air lifts the warmer moist air above the level of free convection and triggers

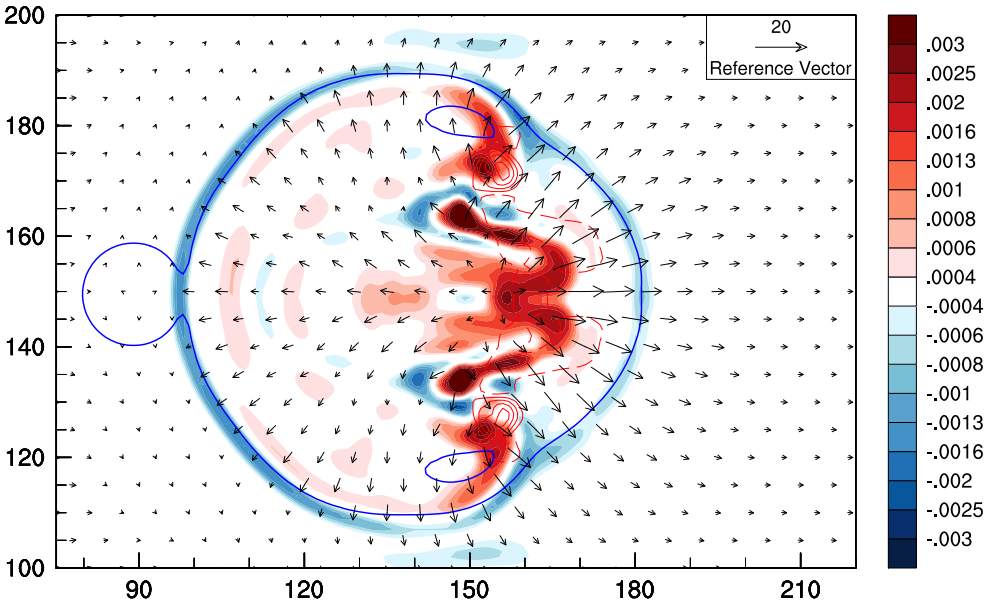


Figure 15: Horizontal zoom of the storm after $2\,\mathrm{h}\,30\,\mathrm{min}$ of storm simulation. Similar to Figure 14, the grid points are labeled on the axes in units of km, the red solid (dashed) lines denote the positive (negative) vertical wind speed at $4600\,\mathrm{m}$ with a separation of $3\,\mathrm{m\,s^{-1}}$, the blue line shows the cold air pool, and the horizontal wind at the lowest level is represented by the vectors. The filled contours represent the lowest level divergence in red and convergence in blue in units of $\mathrm{s^{-1}}$.

new convection. As a result, two new cells form along the storm-induced cold outflow around 3 hours of simulation, as shown in Figure 16(a). They interact and produce strong convergence along the cold pool (Figure 16(b)). A local maximum of convergence develops in between and triggers a third cell which reaches a maximal vertical wind speed of nearly $44\,\mathrm{m\,s^{-1}}$ after 3 hours and 50 minutes. Although the updraft equals the intensity of the initial cell updraft, the maximal downdrafts of $-20\,\mathrm{m\,s^{-1}}$, which developed 5 minutes later, are slightly weaker. In contrast to the initial cell development, the new cell is nourished by convergence and sustains an updraft of more than $35\,\mathrm{m\,s^{-1}}$ for over 30 minutes. The further development is, however, similar. The upward moving air diverges as soon as it reaches the tropopause and builds an anvil. The three cells exhibit equal features concerning the vorticity. Figure 17(a) shows the vertical vorticity distributions at midlevels after 4 hours of simulation. Interestingly, every cell (red contour lines of vertical wind) includes two counter-rotating parts, i.e., the left part rotates counterclockwise whereas the right part shows negative vorticity. These rotations induce a separation of the three cells which causes a spread of the precipitation over a larger area (cf. Figure 17(b)). Additionally, the cell in the middle widens and splits into three updraft cells. Their intensities decline, however, rapidly due to water loading, whereas the two flank

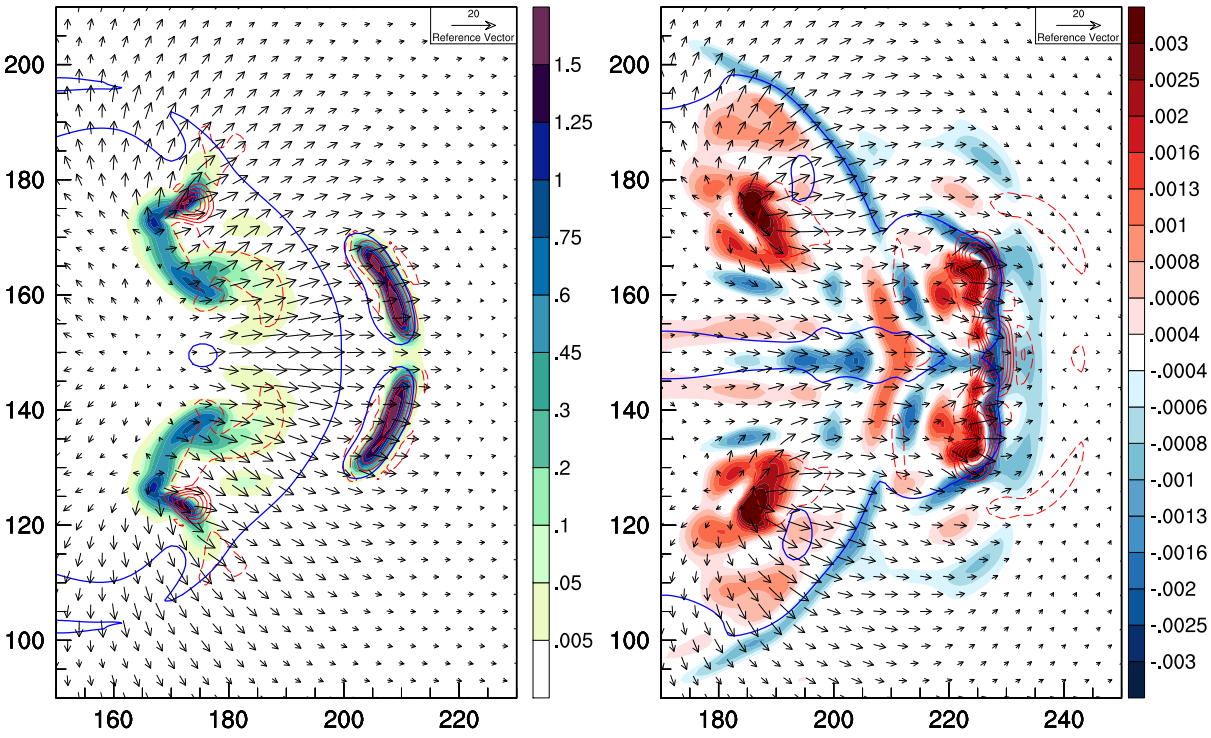


Figure 16: Horizontal plot of precipitating hydrometeors in units of $\mathrm{g\,kg^{-1}}$ at the lowest level after $3\,\mathrm{h}$ (a) and of divergence in units of $\mathrm{s^{-1}}$ after $3\,\mathrm{h}\,30\,\mathrm{min}$ (b). The positive (negative) vertical wind speed at $4600\,\mathrm{m}$ are represented by the red solid (dashed) lines with a separation of $3\,\mathrm{m\,s^{-1}}$, the blue line shows the cold air pool, and the horizontal wind at the lowest level is represented by the vectors.

cells gain energy because they lie closer to the gust front which favors inflowing air.

### 3.1.3 Vertical Storm Structure

Interesting features can be observed in a vertical cross-section after 4 hours of simulation (cf. Figure 18). The first feature, that stands out, is the powerful updraft cell (red solid contours) with the overshooting top in the center of the storm. Strong downdrafts (red dashed contours) can be observed on its left and right. The horizontal wind contours (blue lines) exhibit a strong divergence at the tropopause which leads to the anvil shaped storm. Below $4000\,\mathrm{m}$, warm, humid air enters the storm from the front, whereas midlayer air enters the storm at around $7000\,\mathrm{m}$ from the rear. The first enhances the updrafts whereas the latter augments the downdrafts. This storm structure looks similar to that

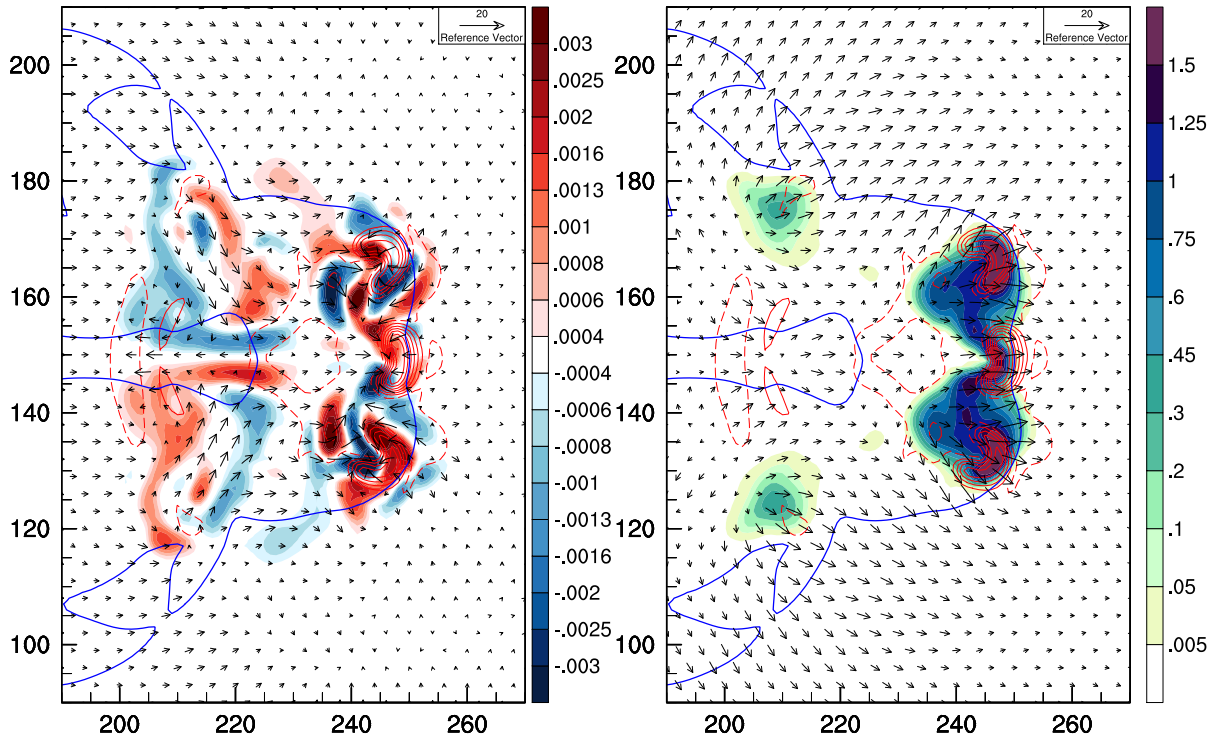


Figure 17: Horizontal slice after $4\,\mathrm{h}$ of simulation. Plot (a) represents the vorticity in units of $\mathrm{s}^{-1}$ at $4242\,\mathrm{m}$ and plot (b) shows the lowest level precipitating hydrometeor (rain, snow, and graupel) content in units of $\mathrm{g\,kg}^{-1}$. The horizontal wind is sketched by the vectors at the same level as vorticity and precipitation respectively. The red solid (dashed) lines denote the positive (negative) vertical wind speed at $4600\,\mathrm{m}$ with a separation of $3\,\mathrm{m\,s}^{-1}$. The cold air pool is shown by the blue line which marks a surface temperature anomaly of $-0.5\,\mathrm{K}$.

of the schematic sketch in Figure 6. The downdrafts lead to an outflow at the surface which builds the cold pool. The solid black line marks the $-0.5\,\mathrm{K}$ surface temperature anomaly. The gust front exhibits its characteristic shape, its bulbous head with air circulation. Right behind the gust front, there is a surface pressure maximum which exceeds the environmental pressure by about $1.5\,\mathrm{hPa}$. The head of the gust front is responsible for the location of the new triggered cells. It should be mentioned, that the cells, that trigger after about 3 hours (cf. Figure 16(a)), are located about $5\,\mathrm{km}$ ahead of the surface gust front which corresponds approximately to the location of the gust front about $1500\,\mathrm{m}$ above the ground.

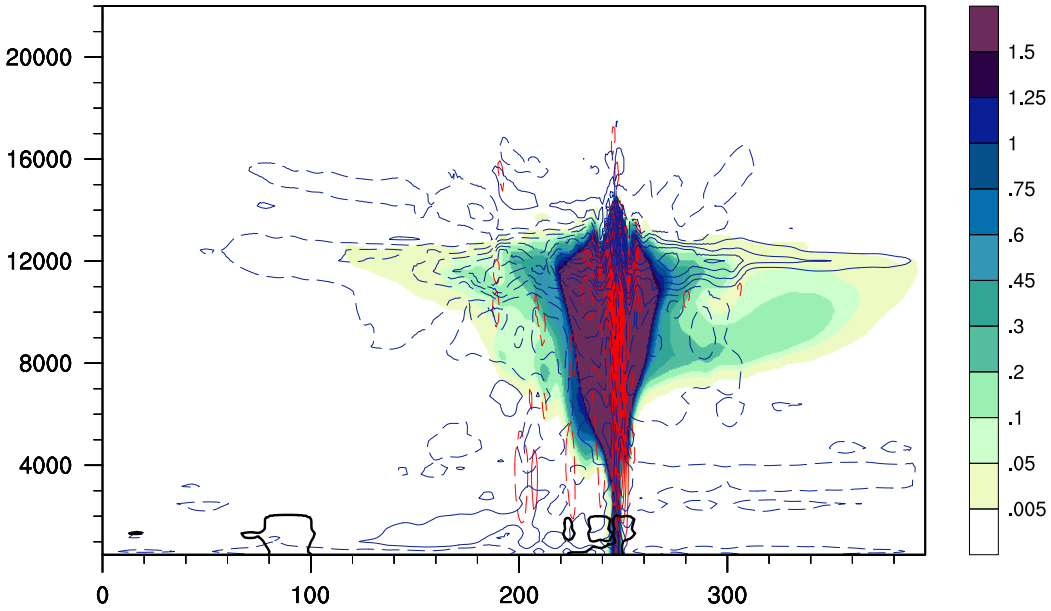


Figure 18: Vertical plot through the middle of the area in y-direction at $y = 151\,\mathrm{km}$ after $4\,\mathrm{h}$ of simulation. The ordinate describes the height in units of m and the abscissa displays the x-direction of the area in kilometers. The filled contours represent the precipitating hydrometeor content in the atmosphere in units of $\mathrm{g\,kg^{-1}}$ and the vertical wind speed is contoured by the red lines with a separation of $3\,\mathrm{m\,s^{-1}}$. The black solid line marks a cold air pool with a surface temperature anomaly of $-0.5\,\mathrm{K}$ and the solid (dashed) blue lines illustrate the positive (negative) horizontal wind in x-direction. The mature convective storm with an updraft cell illustrates the air flow and precipitating hydrometeor content of the storm.

### 3.1.4 Surface Winds and Accumulated Precipitation

Even though precipitation occurs only for a few minutes at a specific location, the cold pool lasts much longer. Figure 19 shows the cold pool (blue solid line) together with the surface wind after 5 hours of simulation. It can be observed that the cold air, which was brought to the ground during an early stage of the convective storm, has not been removed a few hours later. The surface wind contours point out that the wind maxima occur close to heavy downdrafts and right behind the gust front. The wind maxima lie around $20\,\mathrm{m\,s^{-1}}$ for this storm. Another interesting feature is the wavelike structure of the surface wind with an amplitude of approximately $2\,\mathrm{m\,s^{-1}}$. These waves in the wind field are consistent with the waves in the divergence field.

Figure 20, which shows the accumulated surface precipitation 5 hours after the initiation of the storm, summarizes many aforementioned features. The accumulated surface precipitation illustrates nicely the development of the different cells, i.e., the split of the initial cell which leads to a v-shaped form at the beginning, the triggering of the two new

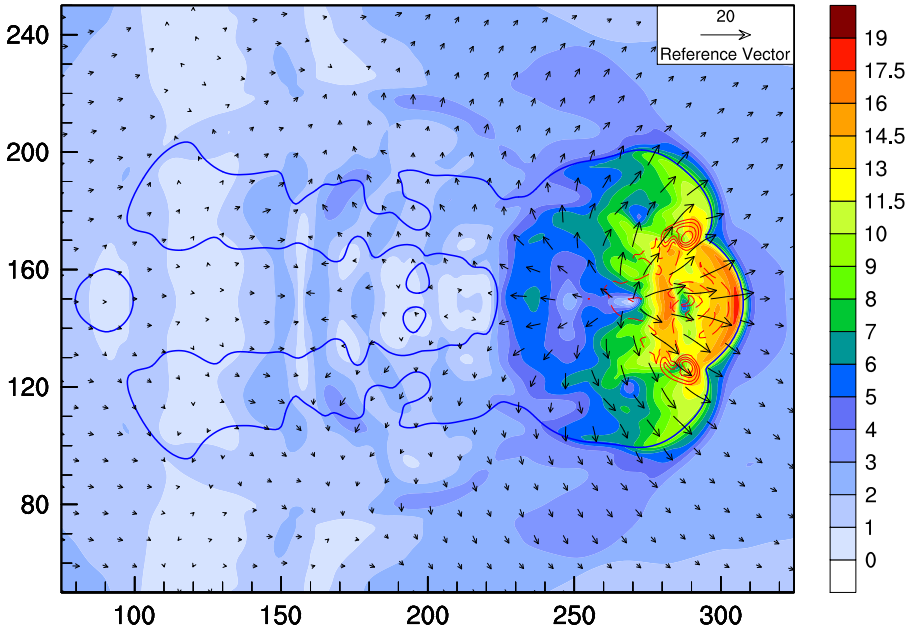


Figure 19: Near-surface horizontal wind in units of $\mathrm{m\,s^{-1}}$ after 5 hours of simulation. The vertical wind at $4600\,\mathrm{m}$ is shown in red lines with a contour interval of $3\,\mathrm{m\,s^{-1}}$ and the cold pool is indicated with the blue contour line which defines a surface temperature anomaly of $-0.5\,\mathrm{K}$.

cells which brought heavy precipitation between 210 km and 250 km, and the third cell with its splitting into three between 250 km and 290 km. It can be concluded, that the heavy precipitation occurs beyond the updraft cells of the simulated convective storm. As a consequence, intense precipitation maxima arise preferably when convective cells with vigorous updrafts start to load water, i.e., after about 1 hour and 3 hours 20 minutes of simulation, as shown in Figure 21. It further illustrates, that the secondary cell produces more intense precipitation, with maxima over $100\,\mathrm{mm\,h^{-1}}$, than the initial cell of the storm.

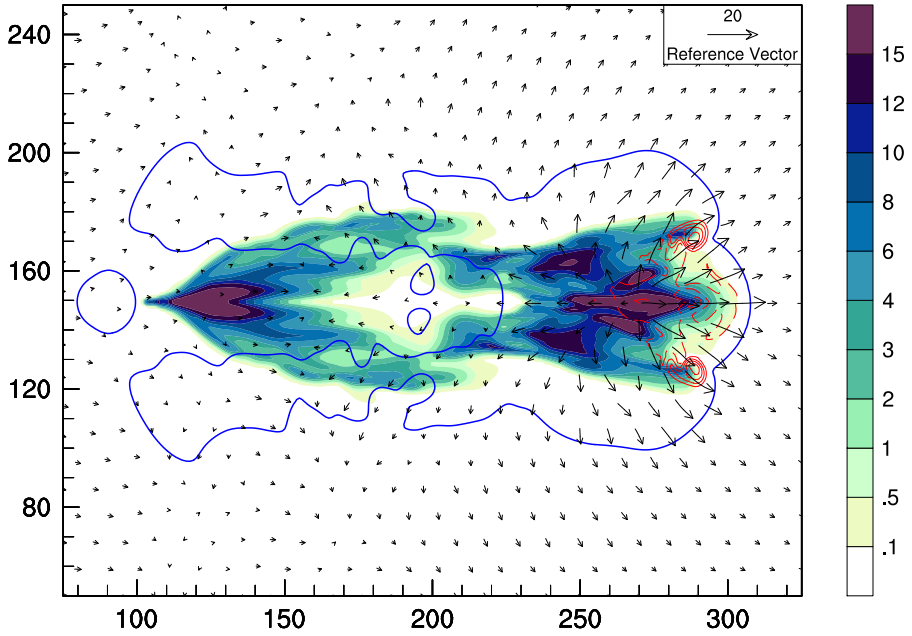


Figure 20: Accumulated surface precipitation in units of $\mathrm{kg\,m^{-2}}$ together with the cool air pool within the blue contour line, which marks a surface temperature anomaly of $-0.5\,\mathrm{K}$, and vertical wind at $4600\,\mathrm{m}$ (red lines with contour spacing of $3\,\mathrm{m\,s^{-1}}$) after $5\,\mathrm{h}$ of simulation.

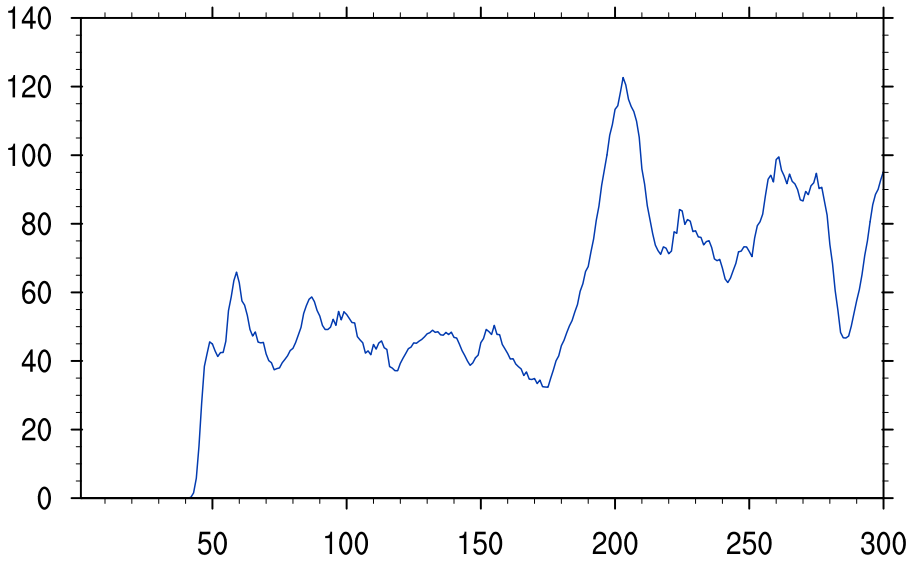


Figure 21: Maximum precipitation intensity in units of $\mathrm{mm\,h^{-1}}$ as a function of time in units of $\mathrm{min}$.

## 3.2 Ensemble Simulations

Convective storms are highly sensitive to certain changes in the atmospheric environment. Ensemble simulations can give insight into these sensitivities by using perturbed initial conditions that influence the storm evolution and structure in a certain way. For quantities with a large impact on the storm development, even small perturbations lead to evident differences in the storm simulations, whereas large disturbances in the initial conditions of other quantities can have only a minor influence. In the current thesis, the investigation focuses on three quantities, namely, horizontal wind, temperature, and humidity. All three play a key role for convective storm development. For 18 ensemble members, the initial profiles are perturbed sinusoidally with a random phase and amplitude, as described in Section 2.2. The standard deviation determines the strength of the perturbation. It is important to choose sensible initial condition perturbations in order to obtain meaningful ensembles. On the one hand, the perturbations must not be too small for observing significant differences in the storm simulations, but on the other hand, large perturbations can lead to a considerable spread in the ensemble members reaching from unrealistic intense storms to no storms at all. The uncertainties in the measurement of the sounding are taken as rough guidance value for the applied standard deviations.

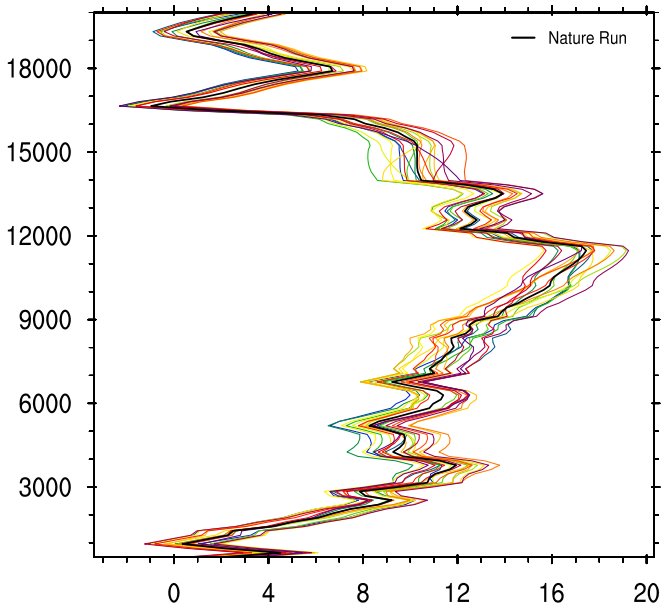


Figure 22: Horizontal wind profiles of the ensemble members of ens002. The black line denotes the reference run profile. The abscissa represents the wind speed in $\mathrm{m\,s^{-1}}$ and the altitude in m is shown on the ordinate.

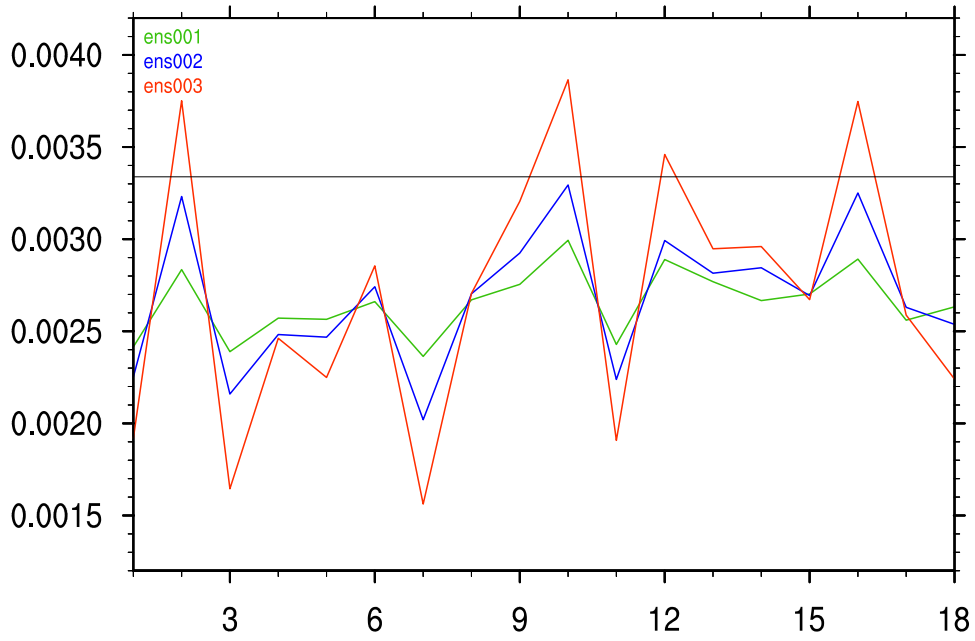


Figure 23: Maximal vertical vorticity of the ensembles ens001, ens002, and ens003 after 30 minutes of simulation. The x-axis shows the 18 ensemble members whereas the y-axis exhibits the vorticity in units of $s^{-1}$. The thin black line marks the vorticity of the nature run.

### 3.2.1 Horizontal Wind Perturbation

First, the influence of the horizontal wind perturbations on the convective ensemble members is examined. Three ensembles, ens001, ens002, and ens003, are generated with perturbation standard deviations of $0.5\,\mathrm{m\,s^{-1}}$, $1\,\mathrm{m\,s^{-1}}$, and $2\,\mathrm{m\,s^{-1}}$. Figure 22 shows the symmetric perturbation with a standard deviation of $1\,\mathrm{m\,s^{-1}}$ around the unperturbed nature run profile of ensemble ens002. The plot illustrates the vertical wind shear with height which varies in intensity for the different ensemble members. As a result, not only the storm propagation speed is affected, but also the initial horizontal vorticity. A weak (strong) shear implies small (large) horizontal vorticity which leads to weaker (stronger) vertical vorticity after the updrafts have lifted the boundary layers. Figure 23 shows the distribution of the maximal vertical vorticity for the three ensembles after 30 minutes of simulation. This instant of time is representative for the initial vertical vorticity that has been built due to the transformation of horizontal rotation into vertical vorticity. The thin black line is the reference value of the nature run which surmounts the ensemble mean remarkably. It can be seen that high-resolution convective storms exhibit larger vertical vorticity than the coarser grid ensemble simulations. Another, not really surprising feature, is illustrated in Figure 23: a larger perturbation implies larger differences in the ensemble member maximal vorticities. The effect of these discrepancies are visible in Figure 24, which shows the panel plots of the accumulated surface precipitation after 5

hours of simulation of the ensemble ens003. The degree of splitting of the initial updraft cell is highly correlated with the maximal vertical vorticity. Strong vorticity enhances the splitting which can be observed in the storms 002, 010, or 016. In contrast, the members 001, 003, or 011 show only a weak separation of the initial storm cell. This process is crucial for the further development of the storms. Convective cells with large vorticity start to split earlier which favors early precipitation occurring between the split cells. The split cells are, thus, close to the gust front and are nourished by lifted boundary air masses. Small vorticity, on the other hand, inhibits an early separation of the initial updraft cell. This leads to a diminution of the vertical winds as soon as precipitation initiates. The resulting cold pool spreads and the gust front moves away from the updraft cell hindering the further development of the storm. There is a tendency that storms with weak initial wind shear show a narrow structure whereas stronger wind shear result in a broader precipitation distribution.

Another feature, that occurs due to the wind perturbation, is the difference in the storm propagation speed which equals approximately the vertically averaged, mass weighted horizontal wind (Wallace and Hobbs, 2006). By comparing the precipitation distribution, it can be observed that the ensemble member storms reach different positions in the x-direction. The precipitation of the ensemble member 008, for instance, reaches an x-coordinate of only 250 km whereas storm 012 passes 320 km. These discrepancies are responsible for the ensemble mean to become smoothed out and loose structure. The locations of heavy rainfall, however, look similar in the nature run and the ensemble mean.

Not surprising is the fact that the dissimilarities in the storm structures are correlated to the strength of the perturbation. Figures 25(a) and 25(b) show the nature run as reference, the ensemble means, the ensemble spreads, and the differences between the nature run and the ensemble means for the ensembles ens002 and ens001 with standard deviations of $1\,\mathrm{m\,s^{-1}}$ and $0.5\,\mathrm{m\,s^{-1}}$, respectively. The comparison between the ensemble means of the three cases (cf. Figures 24, 25(a), and 25(b)) shows that the spread in the ensemble members decrease with smaller perturbations. The ensemble means are less smoothed out and exhibit more structures in the accumulated precipitation distribution. The bottom right panels of Figures 25(a) and 25(b) show that the ensemble mean overestimates the surface precipitation in most regions, shaded in blue, except for the ones which show heavy precipitation in the nature run simulations (red contours). The differences lie in the range of around $-10\,\mathrm{kg\,m^{-2}}$ to $+10\,\mathrm{kg\,m^{-2}}$ which is significant. However, it has to be considered that the ensemble means are smoothed out due to the different storm speeds of the ensemble members. The bottom left panels illustrate that the mean spread decreases with a smaller perturbation and increases with the evolution of the storms. Secondary cell developments differ more in the ensemble members than the development of the first cells, which is a direct result of initializing each member with the same warm bubble. In other words, the spread, and equivalently the uncertainty, increases with time.

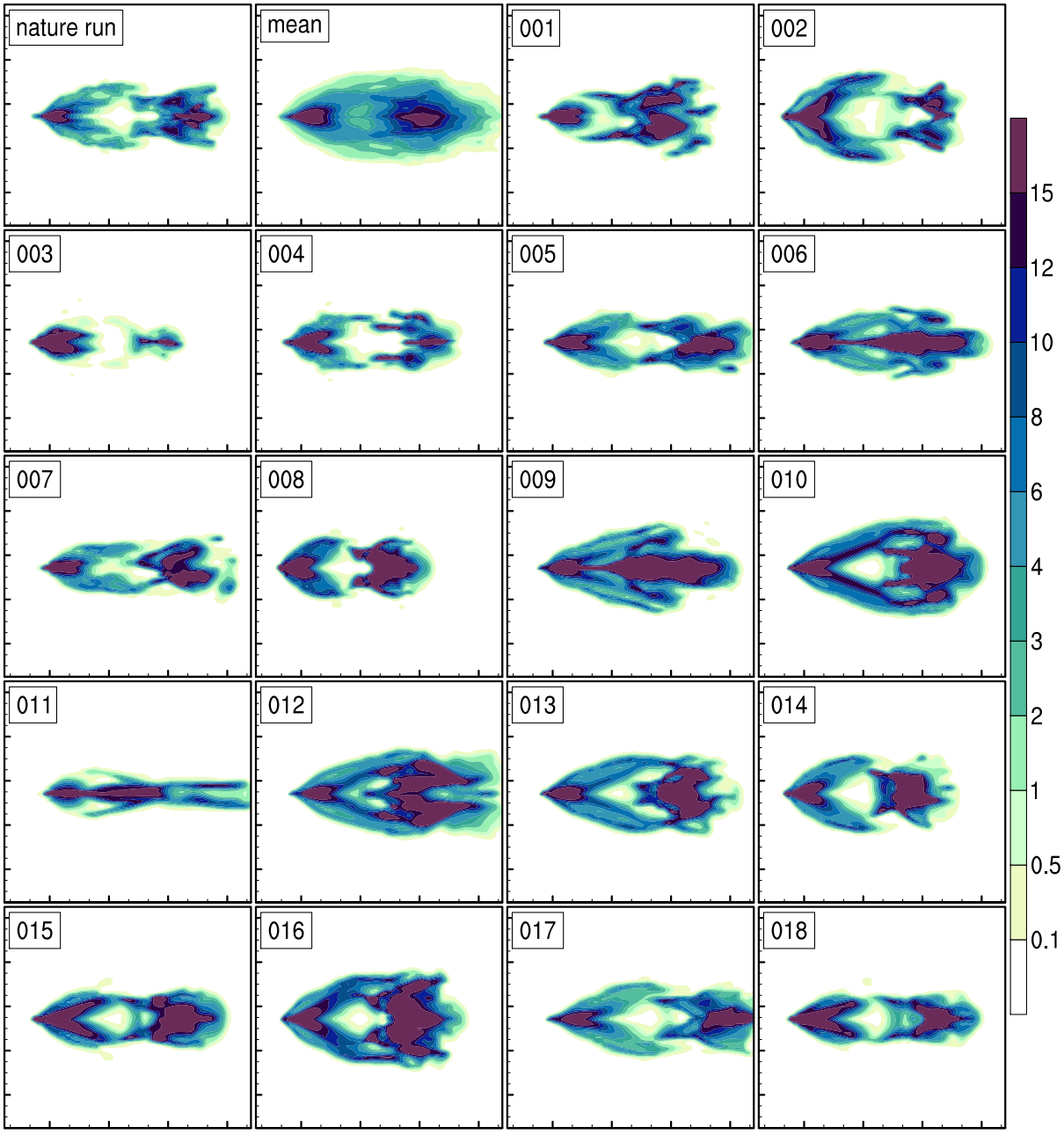


Figure 24: Ensemble ens003. The panels show the accumulated surface precipitation after 5 hours of simulation in units of $\mathrm{kg\,m^{-2}}$ in an area of $75\,\mathrm{km} - 325\,\mathrm{km}$ in x-direction and $50\,\mathrm{km} - 250\,\mathrm{km}$ in y-direction for the nature run, the ensemble mean, and the 18 ensemble members.

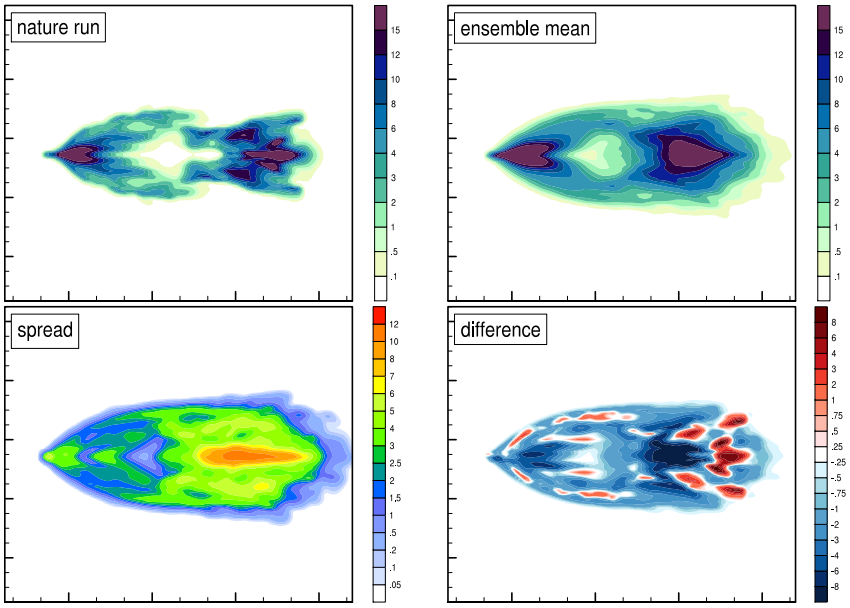


(a) ens002

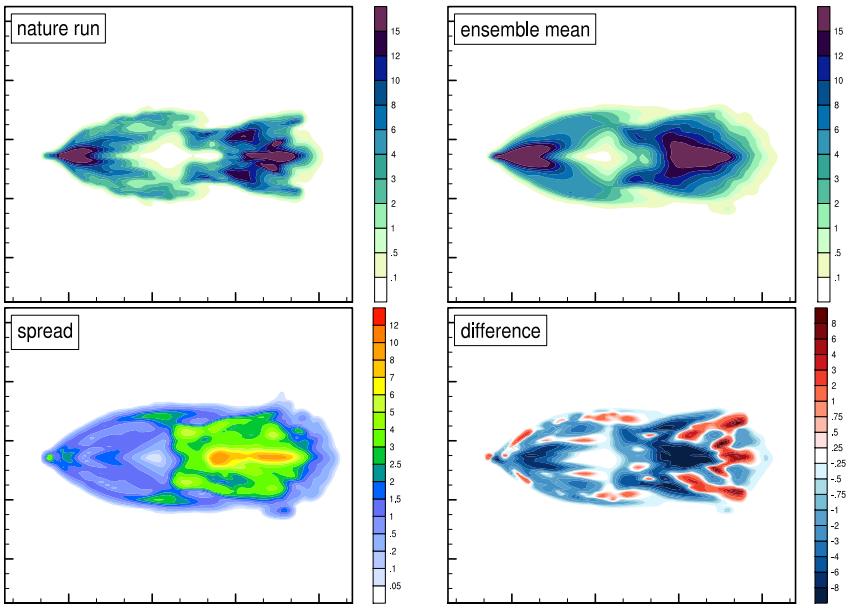


(b) ens001

Figure 25: Ensembles ens002 (a) and ens001 (b). The accumulated surface precipitation in units of $\mathrm{kg\,m^{-2}}$ is plotted in the top left panels for the nature runs and in the top right panels for the ensemble means. The bottom panels exhibit the standard deviation on the left and the differences between the nature runs and the ensemble means on the right (red (blue) colors for larger nature run (ensemble mean) values).

Figure 26 shows the area of surface precipitation as a function of time. Each box represents the amount of grid points exhibiting a density of precipitating hydrometeors exceeding $0.01\,\mathrm{g\,kg^{-1}}$, in the lowest atmospheric layers. The widening of the boxes with progressing time and growing storm complexity give an idea of the increasing uncertainty of the storm simulations. By looking at the nature run, marked in red circles, another feature becomes evident: The ensemble mean, marked with blue dots, exhibits a larger area of precipitation than the nature run. The reason of this bias lies in the different resolution of the ensemble members (2 km) and the nature run (1 km). The coarser grid simulations produce thus more extensive precipitation in the simulations than the fine grid simulation.

Similar features can also be observed by plotting the maximal values of precipitation as a function of time (cf. Figure 27). Precipitation is not only more widespread in coarser resolution simulations, but also more intense. The spread of the precipitation maxima seems, however, small. Furthermore, the storm evolution can be traced by analyzing the position of the boxes. It includes the initiation of precipitation after 50 minutes, the intensification of the initial cell, the following decline after 1 hour 50 minutes, the development of new cells close to 3 hours, their life cycles, and new cell formation around 4 hours. The life cycle of the convective storm looks sinusoidally with a cumulative intensification with time, as seen in a box plot of maximum surface winds (Figure 28). Similarly to precip-

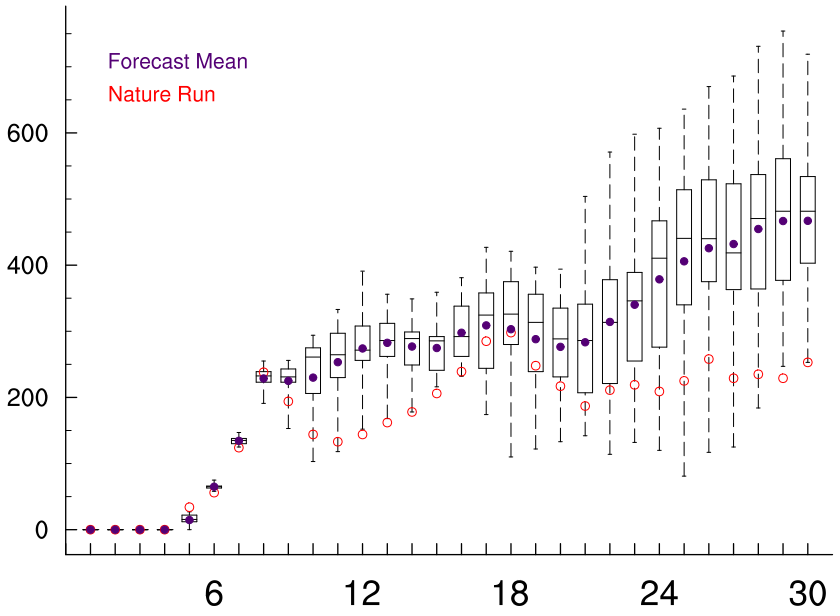


Figure 26: Box plot of the area of precipitating hydrometeors in the lowest level over time for the ensemble ens002. The x-axis represents the time evolution in steps of 10 minutes whereas the y-axis shows the number of grid points ($2\,\mathrm{km} \times 2\,\mathrm{km}$) where the density of precipitating hydrometeors surmounts $0.01\,\mathrm{g\,kg^{-1}}$.

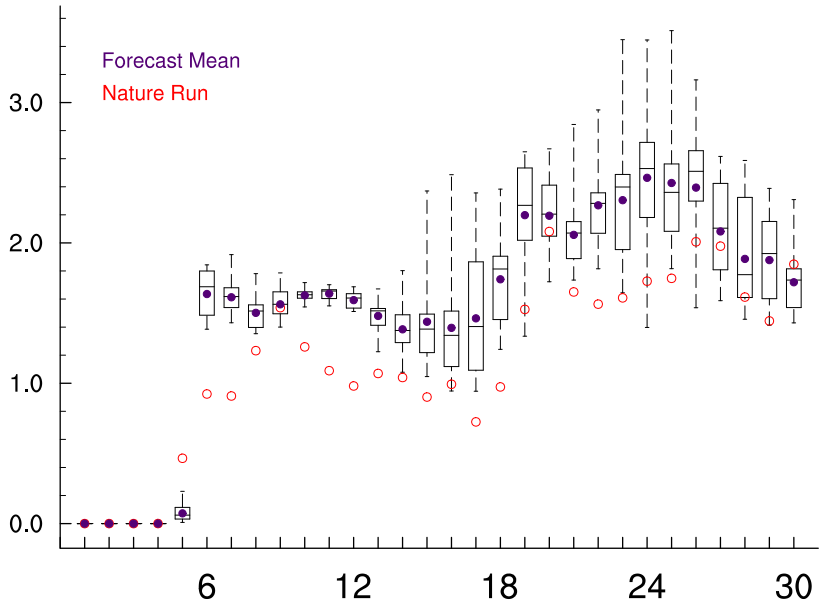


Figure 27: Box plot of the precipitation maxima as a function of time for the ensemble ens002. Time steps of 10 minutes are shown on the x-axis whereas the y-axis represents the precipitating hydrometeor density in units of $\mathrm{g\,kg^{-1}}$.

itation, the nature run systematically produces weaker surface winds than the ensemble simulations. A spread in wind speed is evident already after 10 minutes of simulation. This is caused by the initial perturbation of the horizontal wind.

Figure 29 shows the time evolution of precipitation, surface wind, and temperature at a specific point in the midplane of the storm trace at 250 km in the x-direction, i.e., a place where an intense cell of the nature run passes by. The question of interest was how an observer, located at this point, would sense the passage of this convective storm. The box plots reveal different characteristics of a storm passage. These can be observed at this point approximately 4 hours after the storm initiation. A slight decrease in the wind speed followed by a steep increase (Figure 29(b)) due to the storm's gust front indicates the advent of the convective storm. This change is accompanied by a sudden drop in temperature of 2 K to 3 K (Figure 29(c)) and initiating precipitation (Figure 29(a)) which lasts for about 1 hour. After the passage of the storm, the wind decreases to initial speeds, the temperature increases, however, only slightly and stays cooler than the environment for a longer period.

The ensemble simulation shows that the gust front of every ensemble member passes this point, the exact time, however, differs (compare Figure 29(c)): The first storm member shows the temperature drop already after 3 hours 40 minutes, whereas the last member not until 4 hours 20 minutes. Not only the time, but also the intensity varies for the

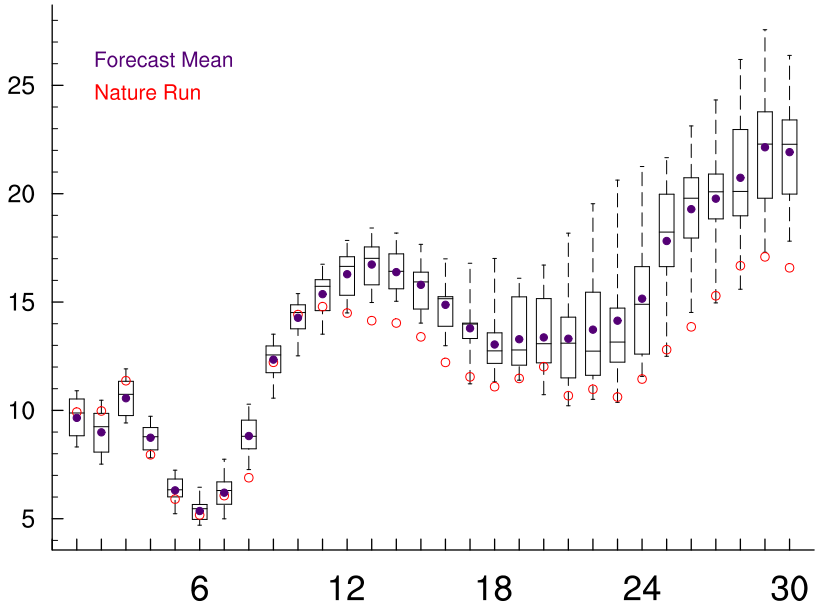


Figure 28: Box plot of the surface wind speed maxima as a function of time for the ensemble ens002. The x-axis represent the time evolution in steps of 10 minutes whereas the y-axis show the wind speed in units of $\mathrm{m\,s^{-1}}$.

ensemble members. Some members show weak surface winds and no precipitation at all at this specific point, other storms bring heavy precipitation and squalls of over $20\,\mathrm{m\,s^{-1}}$. This example illustrates the difficulty in forecasting the exact time and intensity of convective storms at a specific place.

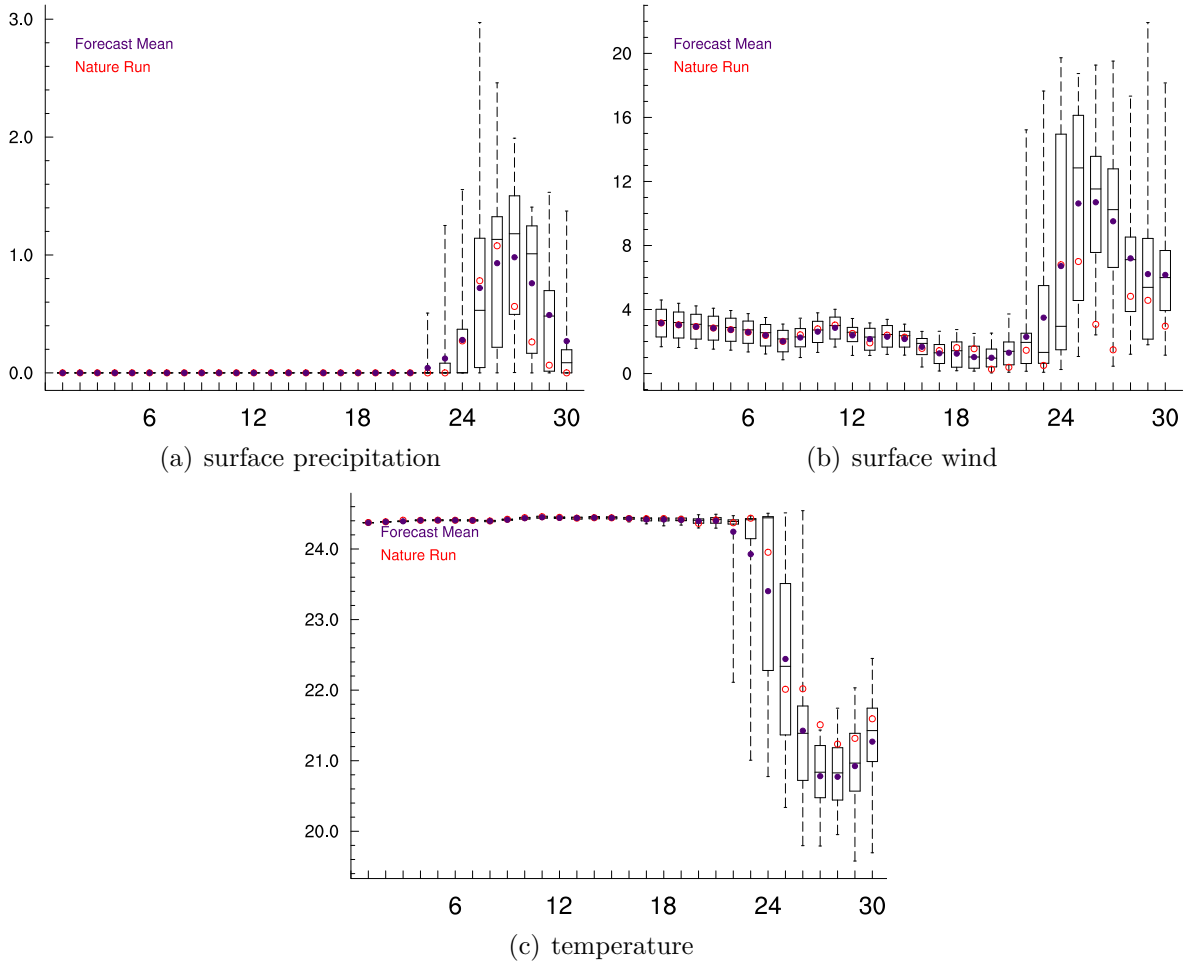


(a) surface precipitation

(b) surface wind

(c) temperature

Figure 29: Time evolution of (a) precipitating hydrometeor density in the lowest atmospheric levels (in $\mathrm{g\,kg^{-1}}$), (b) surface wind (in $\mathrm{m\,s^{-1}}$), and (c) temperature difference in K of a point at the coordinates $(125 \mid 74)$ in the $2\,\mathrm{km}$ grid of the ensemble members of ens002.

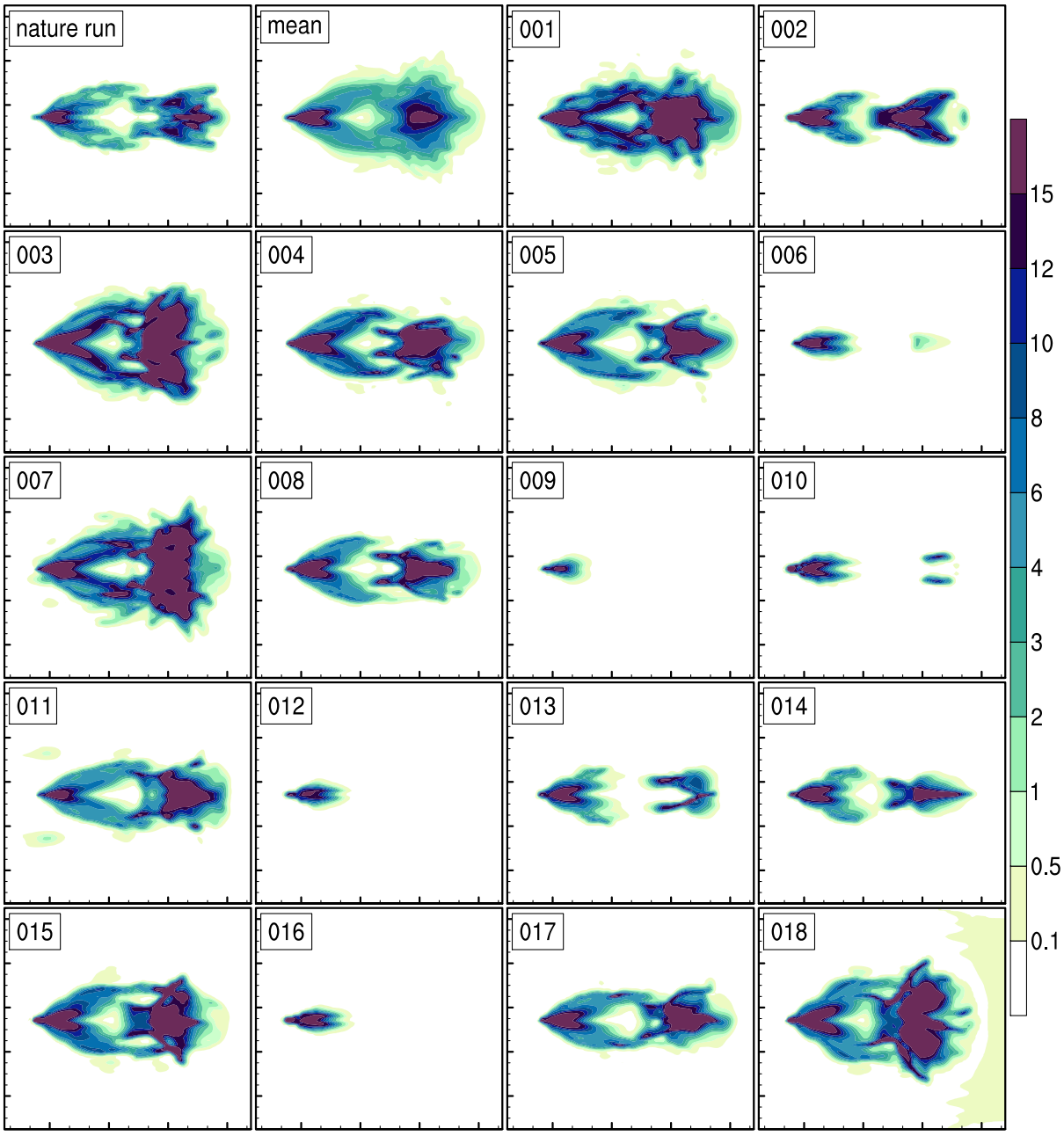


Figure 30: Ensemble ens005. The panels show the accumulated surface precipitation after 5 hours of simulation in units of $\mathrm{kg\,m^{-2}}$ in an area of $75\,\mathrm{km} - 325\,\mathrm{km}$ in x-direction and $50\,\mathrm{km} - 250\,\mathrm{km}$ in y-direction.

### 3.2.2 Temperature Perturbation with Constant Relative Humidity

Ensembles ens004, ens005 and ens006 are generated by perturbation of the environmental temperature. The perturbation amplitudes are chosen such that the standard deviations amount to 0.25 K, 0.5 K, and 1 K. The specific humidity is adapted so that the relative humidity is constant in all ensemble members.

In contrast to the perturbed wind field, a perturbation of the temperature profile results in a constant storm propagation speed for all members, but in a variation of convective available potential energy (CAPE). The spread of the CAPE is mainly caused

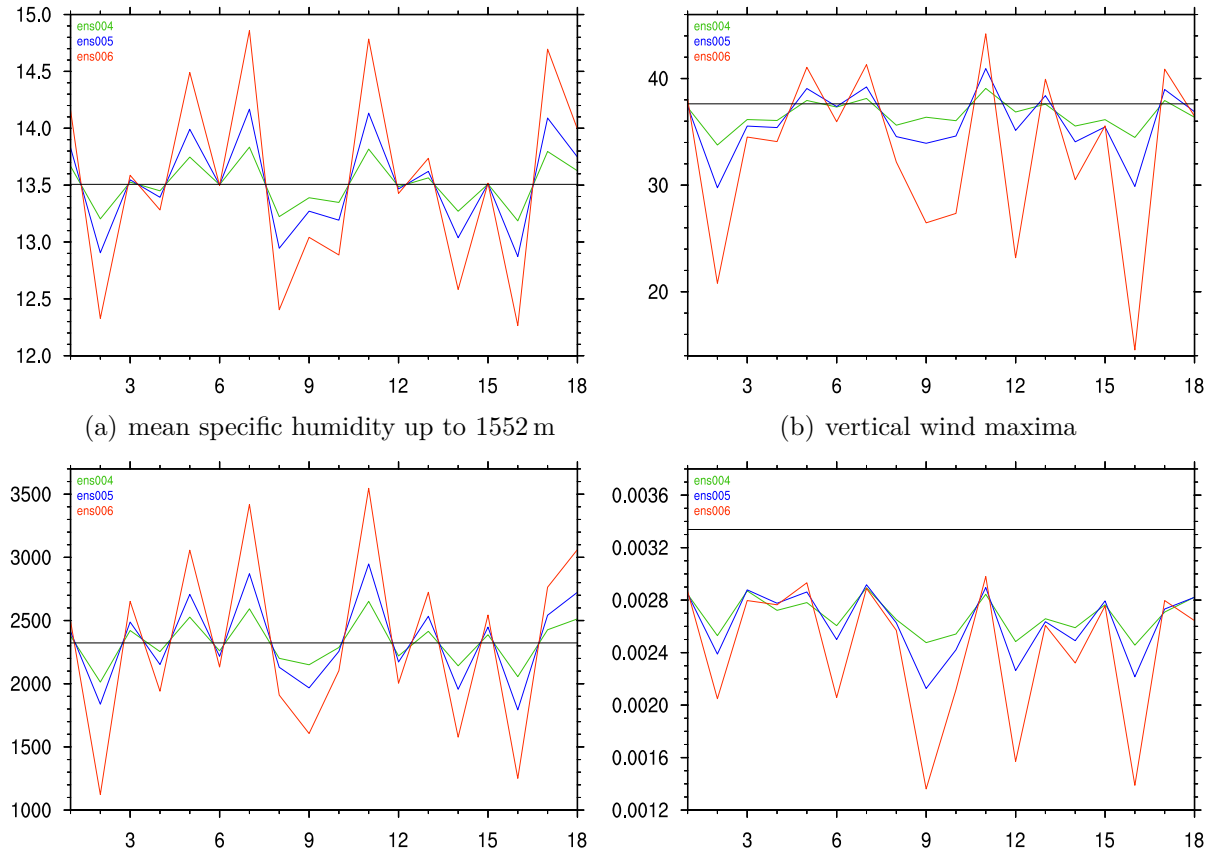


(a) mean specific humidity up to 1552 m

(b) vertical wind maxima

(c) CAPE

(d) vertical vorticity maxima

Figure 31: Specific humidity averaged in the lowest atmospheric levels up to an altitude of 1552 m in $\mathrm{g\,kg^{-1}}$ (a), vertical wind speed maxima in $\mathrm{m\,s^{-1}}$ (b), convective available potential energy in $\mathrm{J\,kg^{-1}}$ (c), and vertical vorticity maxima in $\mathrm{s^{-1}}$ (d) for the ensembles ens004, ens005, and ens006. The vertical wind and vorticity maxima correspond to 30 minutes lead time. The x-axes exhibit the 18 ensemble members whereas the y-axes show the scale for each quantity. The thin black lines stand for the reference values of the nature run.

by variations in the low-level specific humidity, but also by the change in temperature, which influences the buoyancy above the level of free convection. The results confirm the well-known fact that especially low-level disturbances determine the storm development. By cooling the lowest levels, the specific humidity is decreased which implies a decrease of the CAPE, whereas low-level heating leads to an increase of specific humidity and a destabilization of the atmosphere. Figures 31(a) and 31(c) illustrate the strong correlation between the mean specific humidity of the lowest levels (up to an altitude of 1552 m) and the CAPE. The change in the temperature profile in the midlevels affects the CAPE less, although, the buoyancy and, thus, the updrafts are influenced. Nevertheless, these effects sum up and lead to large differences in the CAPE for the ensemble members as listed in Table 1. For instance, the members of the ensemble ens005 exhibit CAPE values that reach from $1800\,\mathrm{J\,kg^{-1}}$ to $2900\,\mathrm{J\,kg^{-1}}$. As a consequence, the atmospheric stability varies remarkably between the ensemble members, leading to extremely different convective storm evolutions. Figure 30 shows the result of ens005. Obviously, there exist convective storms, such as those of members 009, 012, and 016, which are not intense enough to trigger secondary cells. In contrast, the storms of members 003, 007, and 018 exhibit heavy rainfall and strong winds in the secondary cell development. The discrepancy is even larger for ens006. In this ensemble, members exist, that exhibit an atmosphere which is too unstable. As a consequence, the whole atmosphere starts to rain out and boundary effects dominate the storm simulations.

The CAPE seems to be the determining quantity in these ensembles. By comparing the amount of accumulated surface precipitation of the ensemble members in Figure 30 with the local minima and maxima of Figure 31(c) a correlation can be found, i.e., severe convective storms do preferably develop in environments with a large CAPE. It has been found, that all severe convective storms form in an environment with more than $2400\,\mathrm{J\,kg^{-1}}$ whereas all storms without any secondary developments form in an environment with less than $2300\,\mathrm{J\,kg^{-1}}$ CAPE. The explanation can again be found in the vertical vorticity. The initial CAPE determines the vertical wind speed of the initial cell (cf. Figure 31(d)), i.e., large (small) CAPE leads to strong (weak) updrafts. These updrafts lead to a delay of surface precipitation for highly unstable environments. Therefore, weak storms show a tendency of early precipitation, which reduces the weak updrafts even more and the storm may not be able to form secondary cells. Severe storms, on the other hand, sustain vigorous updrafts over a longer period which is favorable for further cell development. These processes are even enhanced by the vertical vorticity. It has been found that the vertical wind speed maxima correlate with the vertical vorticity maxima, as seen in Figures 31(b) and 31(d). This can be explained by the fact that strong updrafts tilt the horizontal vorticity even more, which implies a larger vertical component of the vorticity. As a result, intense initial updraft cells tend to split earlier and separate faster. It favors the position of the split cells near the gust front where warm, humid air is lifted. In contrast, weak initial updraft cells are weakened by falling precipitation particles and their nourishment from low-level, moist air is blocked by the spreading gust front.

It can be concluded that the CAPE is an important quantity determining convective

storm structures, but not the only one. For instance member 011, exhibiting the largest CAPE, shows only a medium storm intensity. Consequently, it is assumed, that several other processes play an important role in the convective storm development. For instance the convective inhibition and the level of free convection, which are influenced by the temperature perturbation as well, may also have an effect on the storm evolution.

By decreasing the temperature perturbation to a standard deviation of 0.25 K (ens004), the spread decreases and the ensemble becomes comparable to the wind perturbed ensemble ens002 with a standard deviation of $1\,\mathrm{m\,s^{-1}}$. The ensemble mean and the spread show, however, differences compared to the wind perturbation case (compare Figures 32 and 25(a)). First of all, the smoothing out and the stretching of the ensemble mean do not occur in the temperature perturbation case due to the unchanged wind speed. As observed in the spread panel in the bottom left, the initial cells of the ensemble members develop more similarly. The secondary cell development spreads however much more. The differences between the nature run and the ensemble mean lie in a comparable range but are confined to a smaller region. By keeping in mind that the atmospheric instability varies with each member substantially, it is not surprising that the region size, where precipitation occurs, spreads widely in the ensemble. While some ensemble members show no more precipitation after 3 hours of simulation, other convective storms of the ensemble

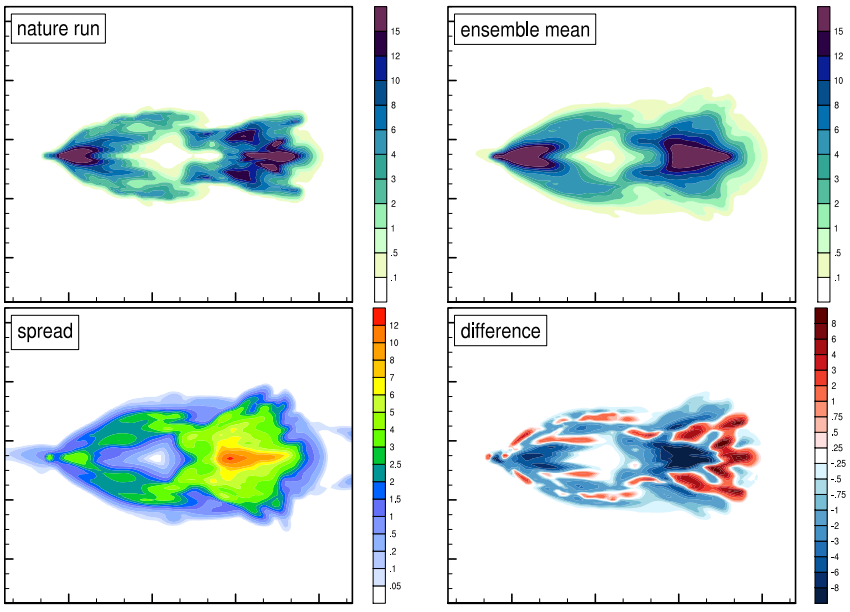


Figure 32: Ensemble ens004. The accumulated surface precipitation in units of $\mathrm{kg\,m^{-2}}$ is plotted in the top left panel for the nature run and in the top right panel for the ensemble mean. The bottom panels exhibit the standard deviation on the left and the differences between the nature run and the ensemble mean on the right (red (blue) colors for larger nature run (ensemble mean) values).

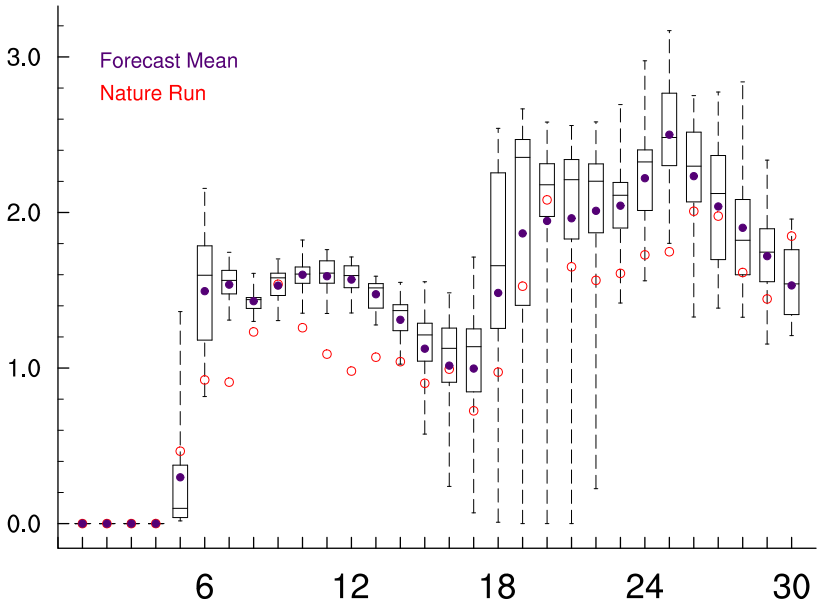


Figure 33: Box plot of the surface precipitation maxima over time for the temperature perturbed ensemble ens004. The x-axis represents the time evolution in steps of 10 minutes whereas the y-axis shows the precipitating hydrometeor density (in $\mathrm{g\,kg^{-1}}$).

produce precipitation in a region that extends over $3200\,\mathrm{km}^2$. The mean maxima of precipitation and wind speed are comparable in the ensembles ens004 and ens002, i.e., the convective storms seem to have similar intensities. As illustrated in Figures 33 and 34, the spread is, however, larger for the temperature perturbed ensemble and it exhibits much more outliers to lower values of precipitation and wind as a result of the weak members without any secondary cell development. The overestimation of precipitation and surface wind with respect to the higher resolution nature run is also present in these ensembles with the temperature perturbations.

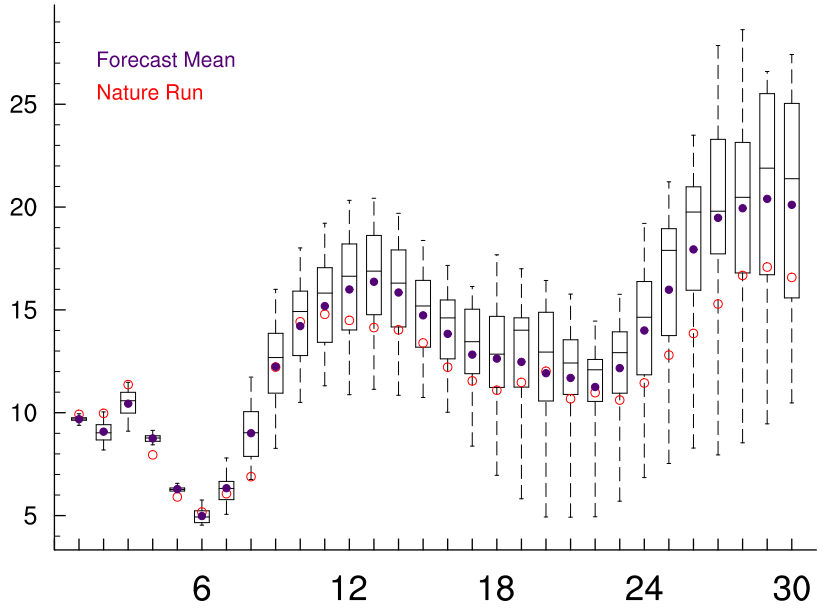


Figure 34: Box plot of the wind speed maxima over time for the ensemble ens004. The wind speed in $\mathrm{m\,s^{-1}}$ is plotted as a function of the time evolution in steps of 10 minutes.

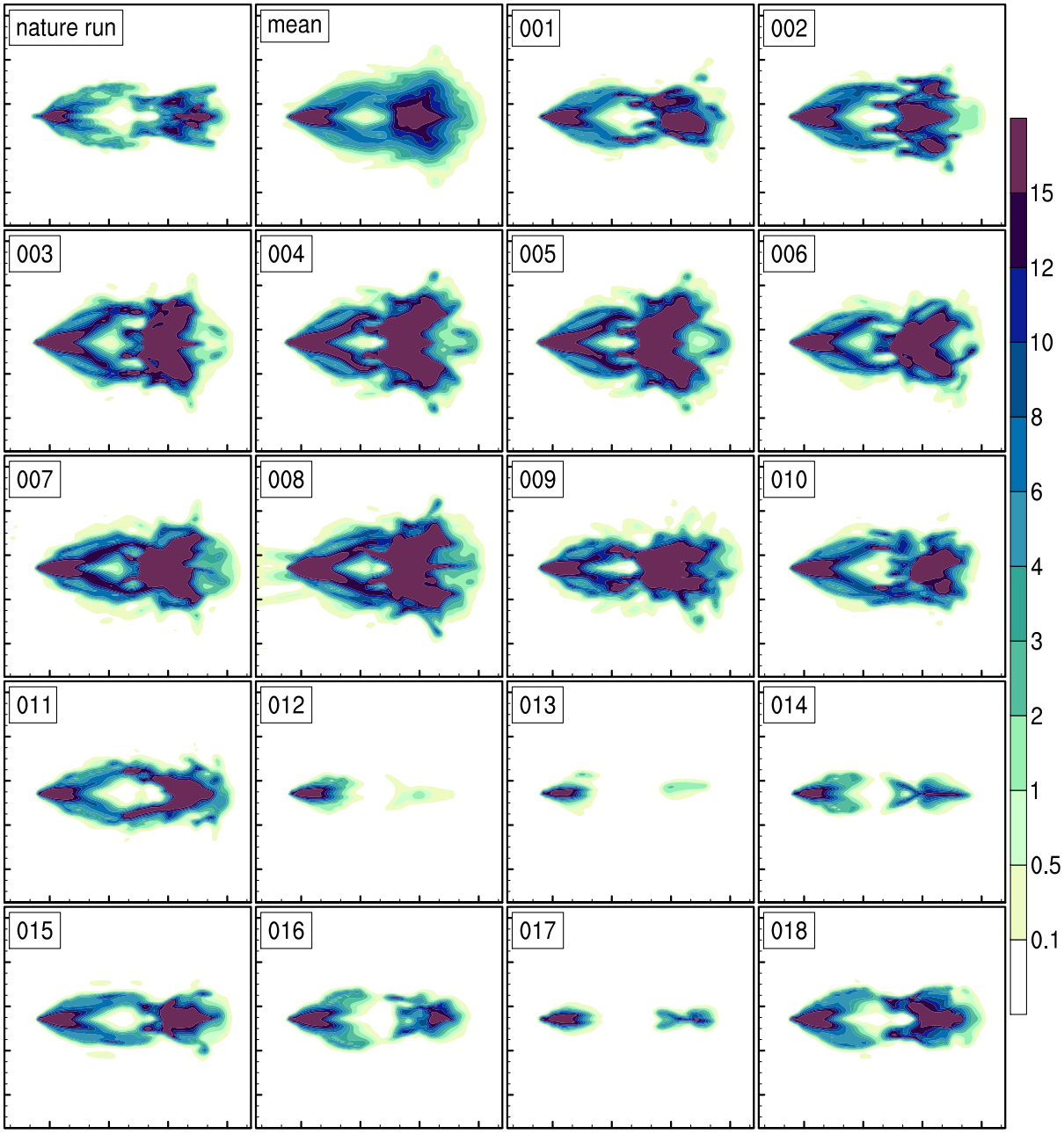


Figure 35: Ensemble ens008. The panels show the accumulated surface precipitation after 5 hours of simulation in units of $\mathrm{kg\,m^{-2}}$ in an area of $75\,\mathrm{km} - 325\,\mathrm{km}$ in x-direction and $50\,\mathrm{km} - 250\,\mathrm{km}$ in y-direction for the nature run, the ensemble mean, and the 18 ensemble members.

### 3.2.3 Temperature Perturbation with Constant Specific Humidity

Ensembles ens007, ens008 and ens009 are generated by perturbation of the temperature profile. The relative humidity is adapted such that the specific humidity stays constant. The perturbation amplitudes exhibit standard deviations of 0.1 K, 0.25 K, and 0.5 K for the three ensembles. Figure 35 shows the accumulated surface precipitation panels for all 18 members of the ensemble ens008 after 5 hours of simulation. The variation among the ensemble members and the ensemble spread are comparable to ens005 (compare with Figure 30). The amount of precipitation is, however, larger for the ensemble ens008,

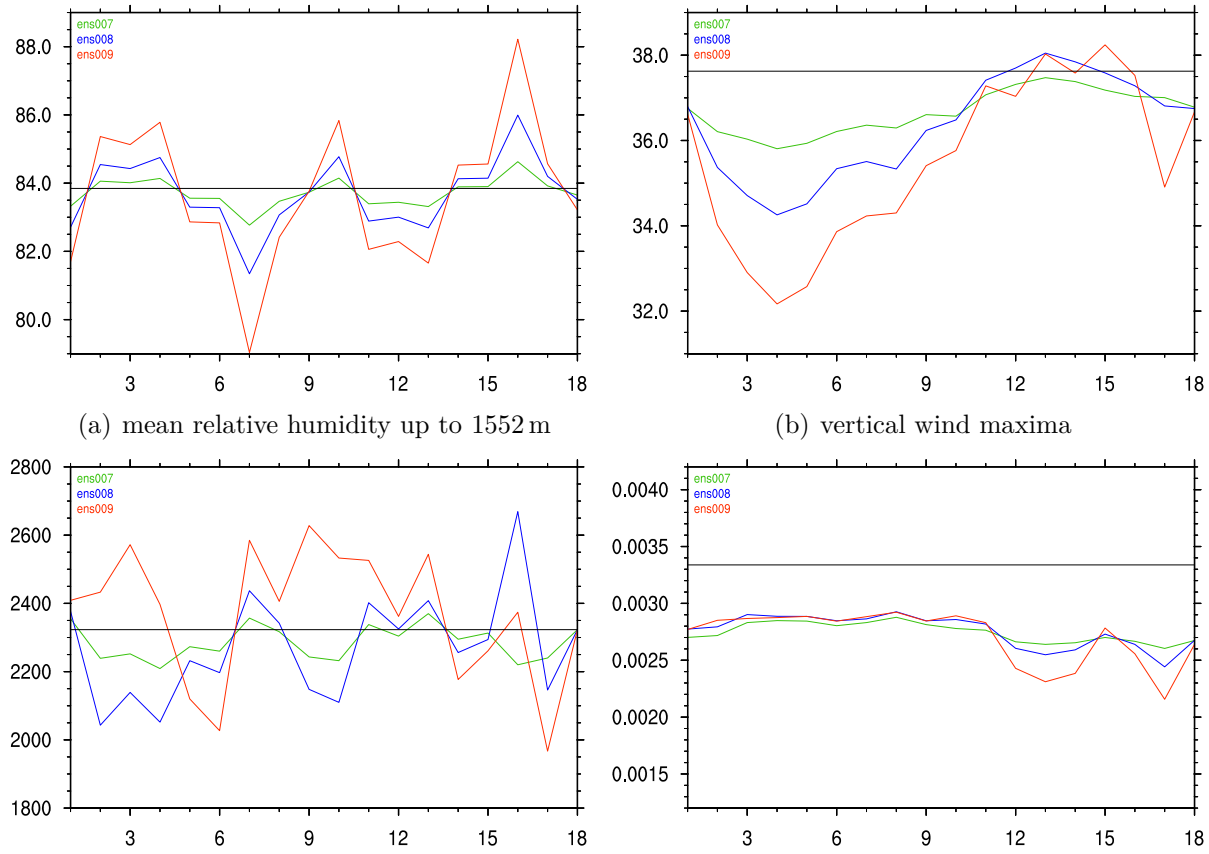


(a) mean relative humidity up to 1552 m

(b) vertical wind maxima

(c) CAPE

(d) vertical vorticity maxima

Figure 36: Relative humidity averaged in the lowest atmospheric levels up to an altitude of 1552 m in % (a), vertical wind speed maxima in $\mathrm{m\,s^{-1}}$ (b), convective available potential energy in $\mathrm{J\,kg^{-1}}$ (c), and vertical vorticity maxima in $\mathrm{s^{-1}}$ (d) for the ensembles ens007, ens008, and ens009. The vertical wind and vorticity maxima correspond to 30 minutes lead time. The x-axes exhibit the 18 ensemble members whereas the y-axes show the scale for each quantity. The thin black lines stand for the reference values of the nature run.

as illustrated in the ensemble mean panel. The storm structures show similar features among the members of ensemble ens008, i.e., the initial cell splittings and movements are comparable in all storms exhibiting secondary cell developments. It seems that the vertical vorticities of the ensemble members do not differ much. Figure 36(d) confirms this assumption by showing a nearly flat vorticity distribution which is accompanied by small differences in the vertical wind maxima (Figure 36(b)). The reason can be found in the small CAPE range of the ensemble. Figure 36(c) shows that the CAPE values of ensemble ens008 reaches only from about $2000\,\mathrm{J\,kg^{-1}}$ to $2400\,\mathrm{J\,kg^{-1}}$ (when the outlier member 016 is neglected). In contrast to the temperature perturbation with constant relative humidity, where the variation in the specific humidity has an influence on the CAPE, a variation in the relative humidity does not affect the CAPE noticeably. There is

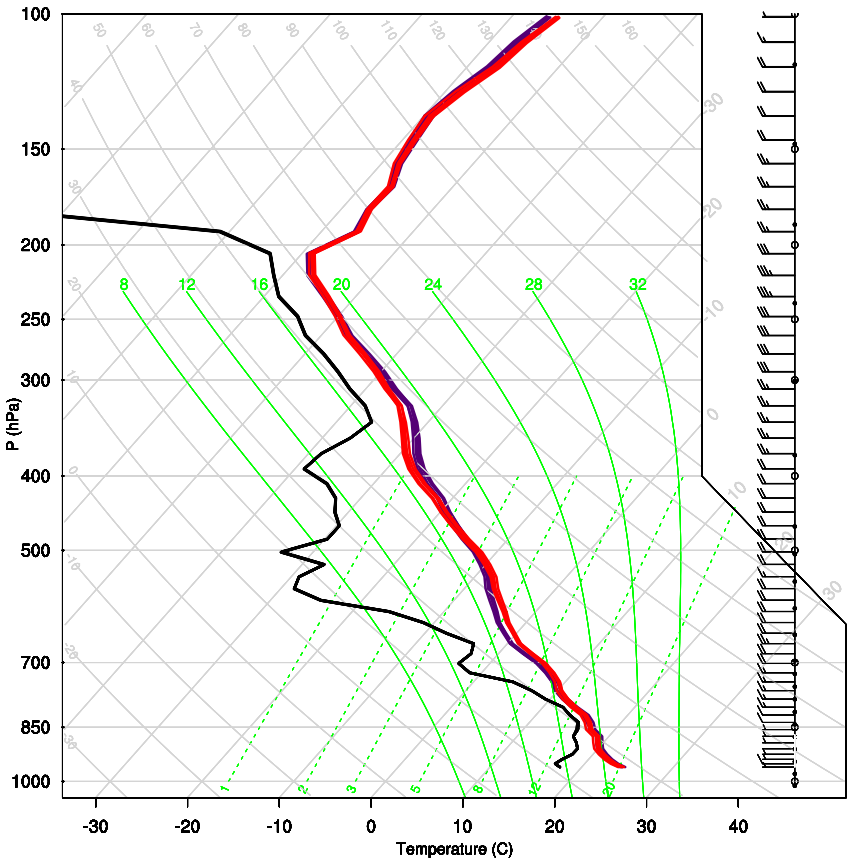


Figure 37: Skew-T log-p diagram for ensemble ens008. The black solid line represents the vertical profile of the dewpoint temperature. The blue lines show the temperature profiles of the members 003, 004, 005, 007, 008 (intense storms) and the red lines indicate the temperature profiles of the members 012, 013, 014, 016, 017 (weak storms). The horizontal wind is represented by the wind barbs which mark $10\,\mathrm{m\,s^{-1}}$.

even an anti-correlation between the CAPE and the mean relative humidity in the lowest levels (cf. Figure 36(a)) which is a feature of the perturbation of the initial temperature profile. By cooling (heating) the temperature in the lowest levels, the atmosphere becomes more stable (unstable), i.e., the CAPE decreases (increases), whereas the relative humidity in these levels increases (decreases) due to the constant specific humidity. Not straight forward is however the reason for different storm developments of the storms because the variation in vorticity or CAPE are of minor importance.

In order to investigate the differences in the storm intensities, the vertical temperature profiles are plotted in Figure 37 for intense storms (members 003, 004, 005, 007, and 008) in blue and for weak storms (members 012, 013, 014, 016, and 017) in red. Although the CAPE shows no evident discrepancy between intense and weak storms, the temperature profiles allow a clear separation of the two storm strengths. The lapse rate of the temperature profiles of intense storms (in blue) indicate, that the atmosphere is more stable between 650 hPa and 330 hPa. As a consequence, the atmospheric stability is decreased between 750 hPa and 650 hPa. Furthermore, the blue lines show that the relative humidity is larger from 800 hPa to 550 hPa for intense storms. This implies a larger buoyant force in these levels. The vertical updrafts are, therefore, enhanced which is crucial for the further storm development. These vertical winds have a positive effect on the low-level convergence (not shown). More warm, humid air converges at the base of the updraft cell and favors vigorous convection over a longer time period. Weak storms produce a smaller

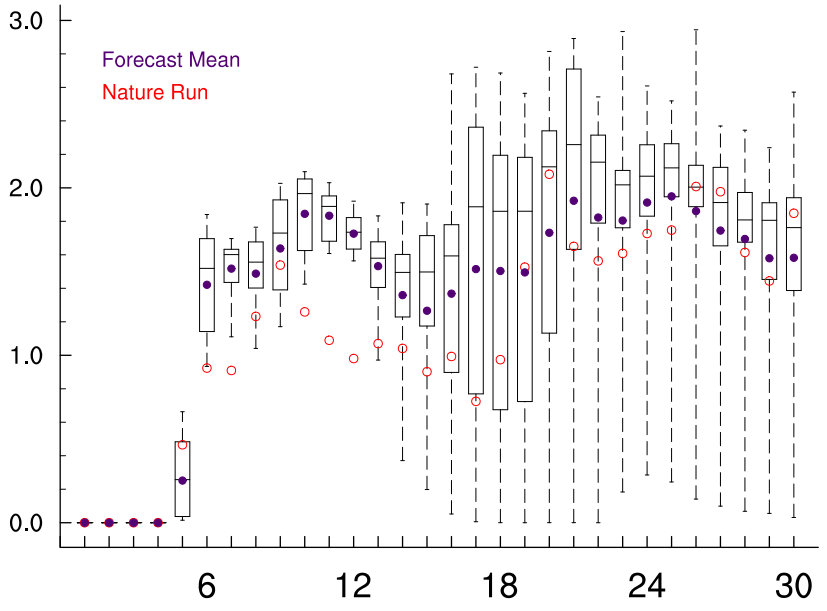


Figure 38: Box plot of the surface precipitation maxima as a function of time for the ensemble ens008. The x-axis represents the time in steps of 10 minutes whereas the y-axis shows the precipitating hydrometeor density (in $\mathrm{g\,kg^{-1}}$).

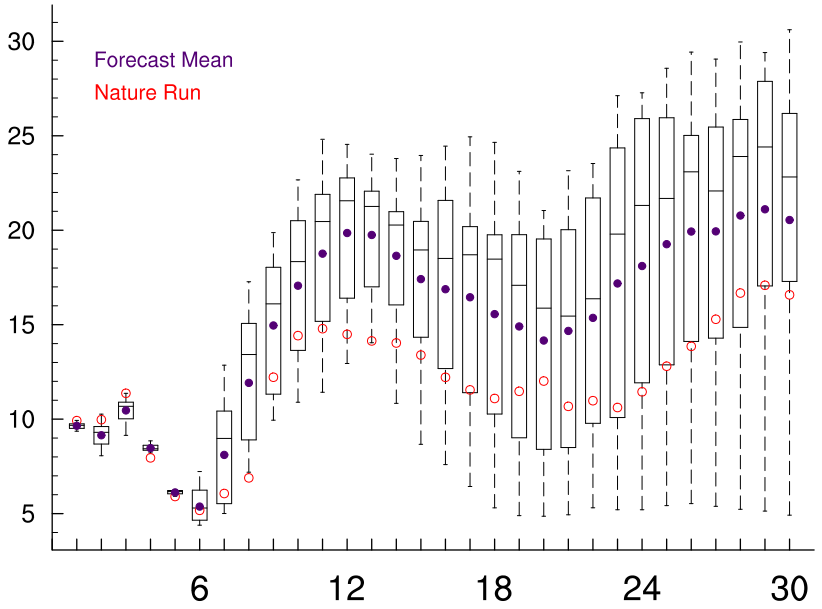


Figure 39: Box plot of the wind speed maxima over time for the ensemble ens008. The wind speed in $\mathrm{m\,s^{-1}}$ is plotted as a function of the time evolution in steps of 10 minutes.

surface layer convergence. For the same reason of buoyancy, the vertical wind speeds of weak storm cells exceed the updraft maxima of intense storms in higher altitudes, above around 4800 m (560 hPa), where the temperature profiles indicate a larger relative humidity for weak storms. This explains the tendency of stronger updrafts for weak storms, as seen in Figure 36(b) after 30 minutes of simulation. The effect can, however, only be observed in an early stage of the storm evolution, before the precipitating hydrometeors reach the ground. Precipitation weakens the updrafts remarkably. Due to the low-level convergence, the intense storms are less affected and can develop secondary cells.

In contrast to the temperature perturbed ensembles with constant relative humidity, ensembles seem to be much more sensitive to a perturbation of the temperature with constant specific humidity. The differences can be observed by comparing the box plots that show the evolution of the precipitation and surface wind speed maxima with time. Figures 38 and 39, showing the maxima of ens008, can be compared with Figures 33 and 34 of ens004. Both ensembles feature identical temperature perturbations, but ens004 has a constant relative humidity profile, whereas ens008 has a constant specific humidity profile. The boxes, representing the precipitation and surface wind speed maxima, show a larger spread of the ensemble ens008 with respect to ens004.

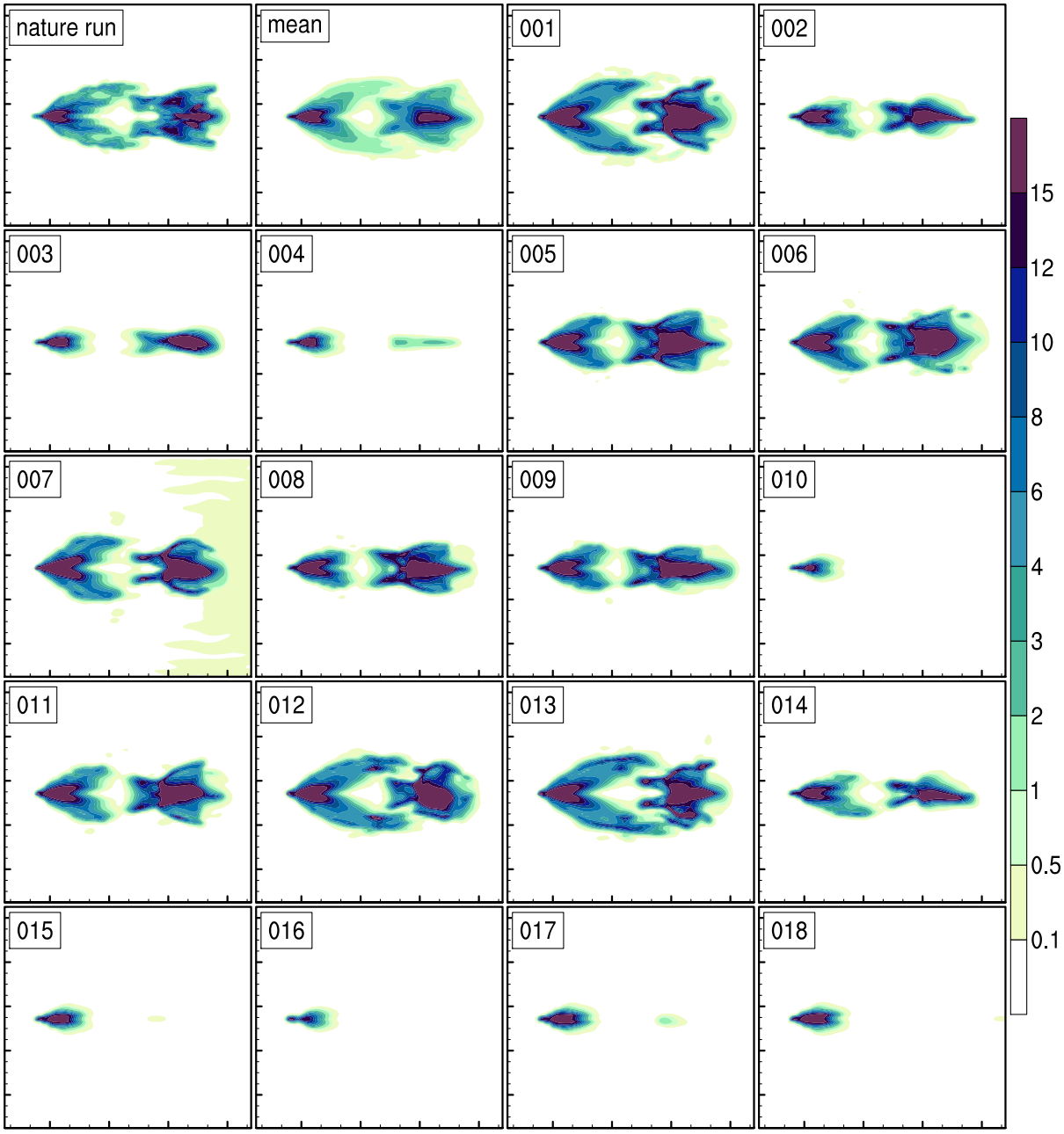


Figure 40: Ensemble ens011. The panels show the accumulated surface precipitation after 5 hours of simulation in units of $\mathrm{kg\,m^{-2}}$ in an area of $75\,\mathrm{km} - 325\,\mathrm{km}$ in x-direction and $50\,\mathrm{km} - 250\,\mathrm{km}$ in y-direction for the nature run, the ensemble mean, and the 18 ensemble members.

### 3.2.4 Relative Humidity Perturbation with Constant Temperature

Ensembles ens010, ens011 and ens012 are generated by perturbing the relative humidity profile. The specific humidity is adapted such that the temperature stays constant. The perturbation amplitudes are chosen such that the standard deviations amount to 2 %, 4 %, and 6 %. Due to the change in specific humidity, CAPE was affected similarly to the ensembles ens004, ens005, and ens006. In contrast to these ensembles, the change of the specific humidity in the lowest level is the only quantity that determines the CAPE due to the constant temperature profile for all ensemble members. The range of the CAPE

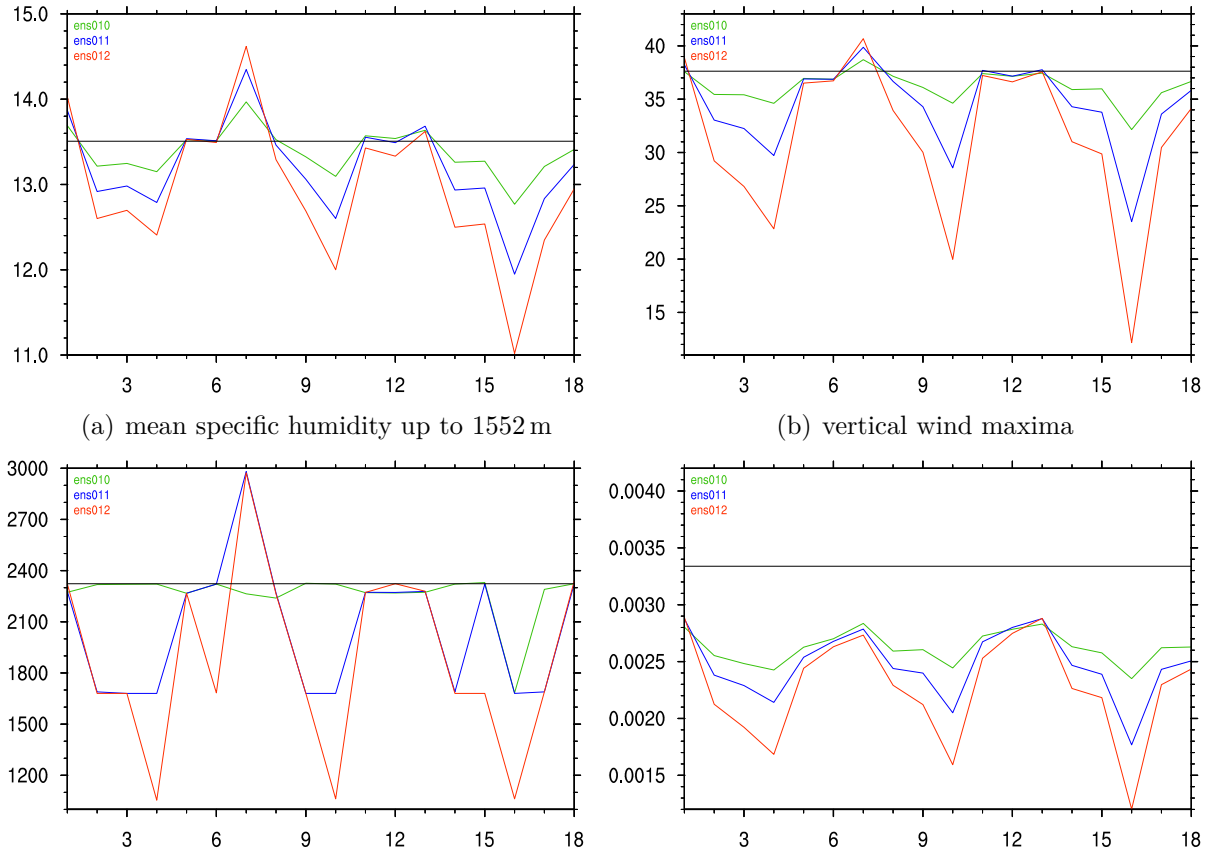


(a) mean specific humidity up to 1552 m

(b) vertical wind maxima

(c) CAPE

(d) vertical vorticity maxima

Figure 41: The panel plots show the specific humidity averaged in the lowest atmospheric levels up to an altitude of $1552\,\mathrm{m}$ in $\mathrm{g\,kg^{-1}}$ (a), the vertical wind speed maxima in $\mathrm{m\,s^{-1}}$ (b), the convective available potential energy in $\mathrm{J\,kg^{-1}}$ (c), and the vertical vorticity maxima in $\mathrm{s^{-1}}$ (d) for the ensembles ens010, ens011, and ens012. The plots of the vertical wind and vorticity represent the maximal values after 30 minutes of simulation. Each quantity is plotted as a function of the 18 ensemble members. The reference values of the nature run are marked by the thin black lines.

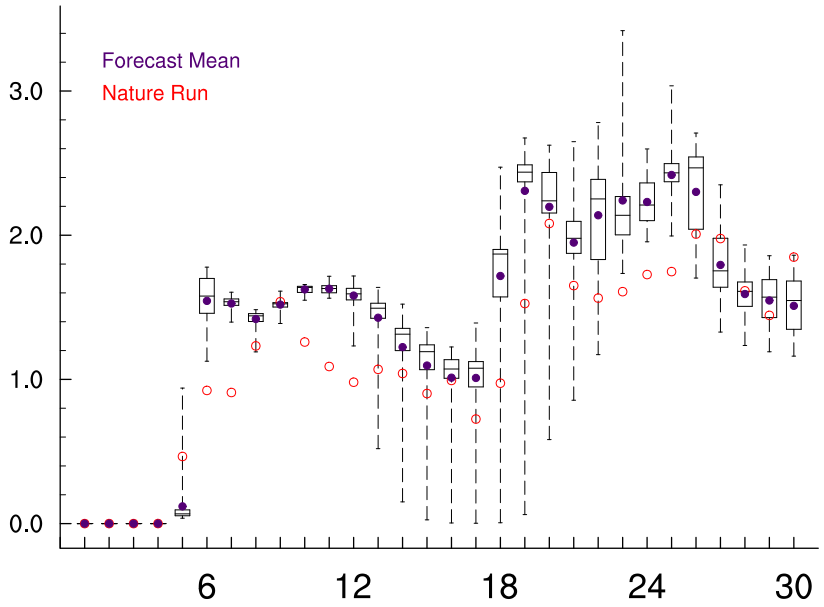


Figure 42: Box plot of the surface precipitation maxima as a function of time for the ensemble ens010. The x-axis represents the time in steps of 10 minutes whereas the y-axis shows the precipitating hydrometeor density (in $\mathrm{g\,kg^{-1}}$).

between the ensemble members is thus smaller for the relative humidity perturbed ensembles ens010, ens011, and ens012 than for the temperature disturbed ensembles ens004, ens005, ens006.

Figure 41 illustrates similar dependencies as seen for the temperature perturbed ensembles with constant relative humidity. The specific humidity in the lowest level determines the CAPE which controls the vertical updrafts and the vertical vorticity component. The vorticity influences the splitting of the initial cells. Depending on the influence, further cell development is either favored or hindered. Crucial for the storm development is, however, not only the specific humidity in the lowest level, which determines the CAPE, but the humidity distribution up to a level of about 750 hPa. That is the reason why the amount of specific humidity, plotted in Figure 41(a) for all ensemble members, correlates best with the storm intensities, illustrated in Figure 40. It shows the accumulated surface precipitation of the nature run, the ensemble mean, and all members of the ensemble ens011. Intense storms, such as those of members 001, 007, 012, or 013, exhibit most humidity in the lowest levels whereas the storms of members 010 and 016, which show the lowest specific humidity in the lower atmosphere, do not produce any secondary cells.

In order to compare the sensitivities of convective storm simulations on a perturbation of the relative humidity and the temperature, respectively, two ensembles, i.e., ens004 and ens010, were chosen. They feature comparable variations in the specific humidity

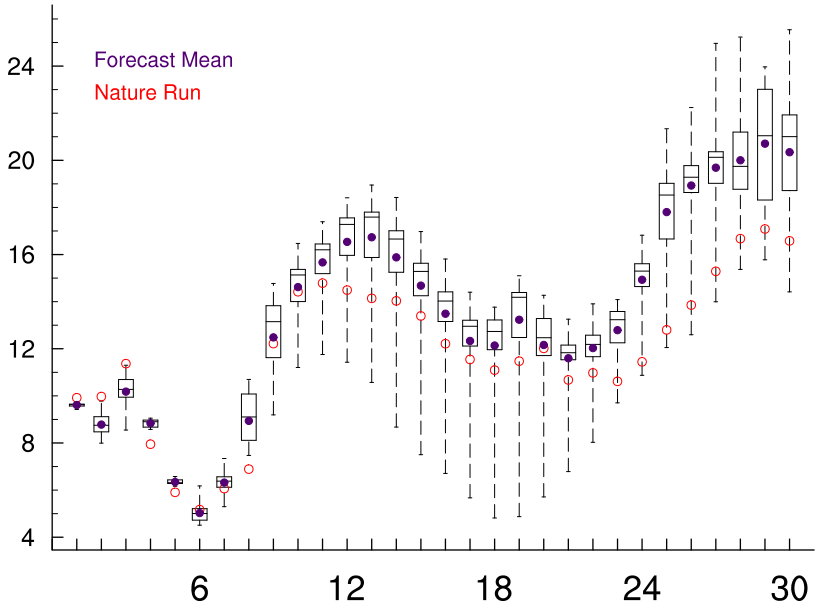


Figure 43: Box plot of the wind speed maxima over time for the ensemble ens010. The wind speed in $\mathrm{m\,s^{-1}}$ is plotted as a function of the time in steps of 10 minutes.

profile. The ensemble ens004, however, includes not only a specific humidity perturbation but likewise changes in the vertical temperature profile which influences the atmospheric stability. It is thus not surprising that ens004 exhibits a larger spread than ens010. The differences can be observed by comparing the surface wind speed and precipitation maxima of ens010 and ens004 (cf. Figures 42 and 43 with the corresponding box plots of ens004 in Figures 33 and 34).

### 3.2.5 Combined Temperature and Wind Speed Perturbation

For the generation of ensemble ens013, perturbations of the horizontal wind and the temperature with constant relative humidity are combined. The ensemble is a combination of ens002 and ens004 with a perturbation exhibiting a standard deviation of $1\,\mathrm{m\,s^{-1}}$ for the horizontal wind and 0.25 K for the temperature profile. In this case, it is interesting to examine the structure of the storms and the change of the spread with respect to the other two ensembles with individual perturbations.

Because the horizontal wind perturbation has no influence on the CAPE distribution in the ensemble, the CAPE of ens013 and ens004 are identical. The vertical vorticity is, however, affected by both the temperature and wind perturbations. Depending on the variations of both quantities, the vorticity differences between the ensemble members is either enhanced or reduced. Figure 44 shows that the vertical vorticity peaks of ens002 and ens004 are anti-correlated. The anti-correlation results from the algorithm of perturbing the horizontal wind, being equal to the one for the temperature. Increasing vertical wind

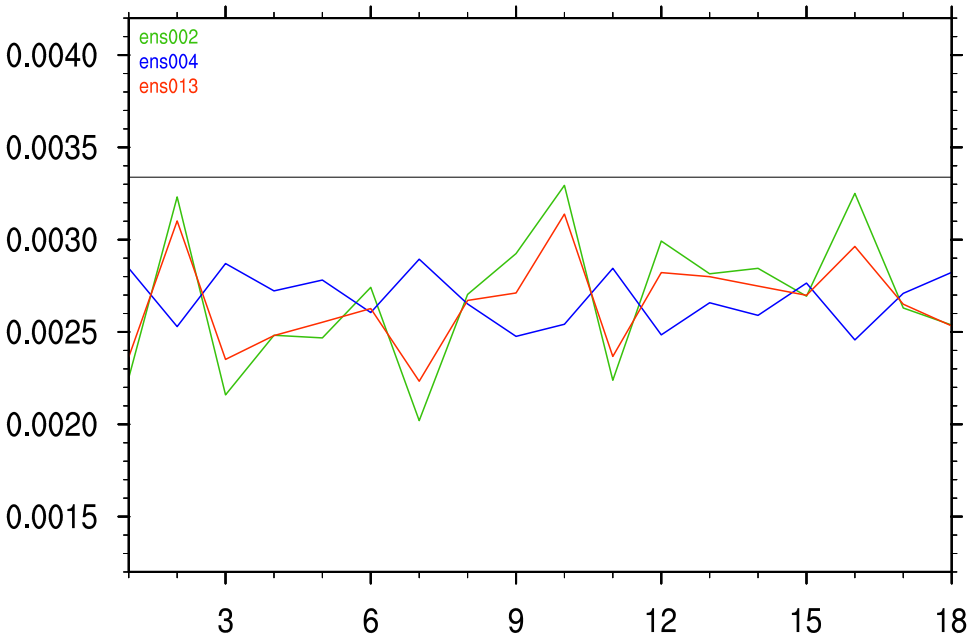


Figure 44: Vertical vorticity maxima in $s^{-1}$ for the ensembles ens002, ens004, and ens013 at 30 minutes lead time as a function of the 18 ensemble members. The thin black lines stand for the reference value of the nature run.

shear in ens002, i.e., weaker horizontal winds in the lower and stronger winds in the upper atmosphere (enhancing the vorticity), implies thus a stabilization of the atmosphere in ens004, i.e., cooling in the lower and heating in the upper atmosphere (decreasing the vorticity due to lower CAPE and weaker updrafts). The net vertical vorticity lies thus in between the two ensembles as observed in Figure 44. As a consequence, a smaller discrepancy between the ensemble members is expected. This is confirmed by the panel plots of the accumulated surface precipitation in Figure 45. The ensemble members look balanced but show, nonetheless, different storm structures contrasting in the initial or secondary cell developments.

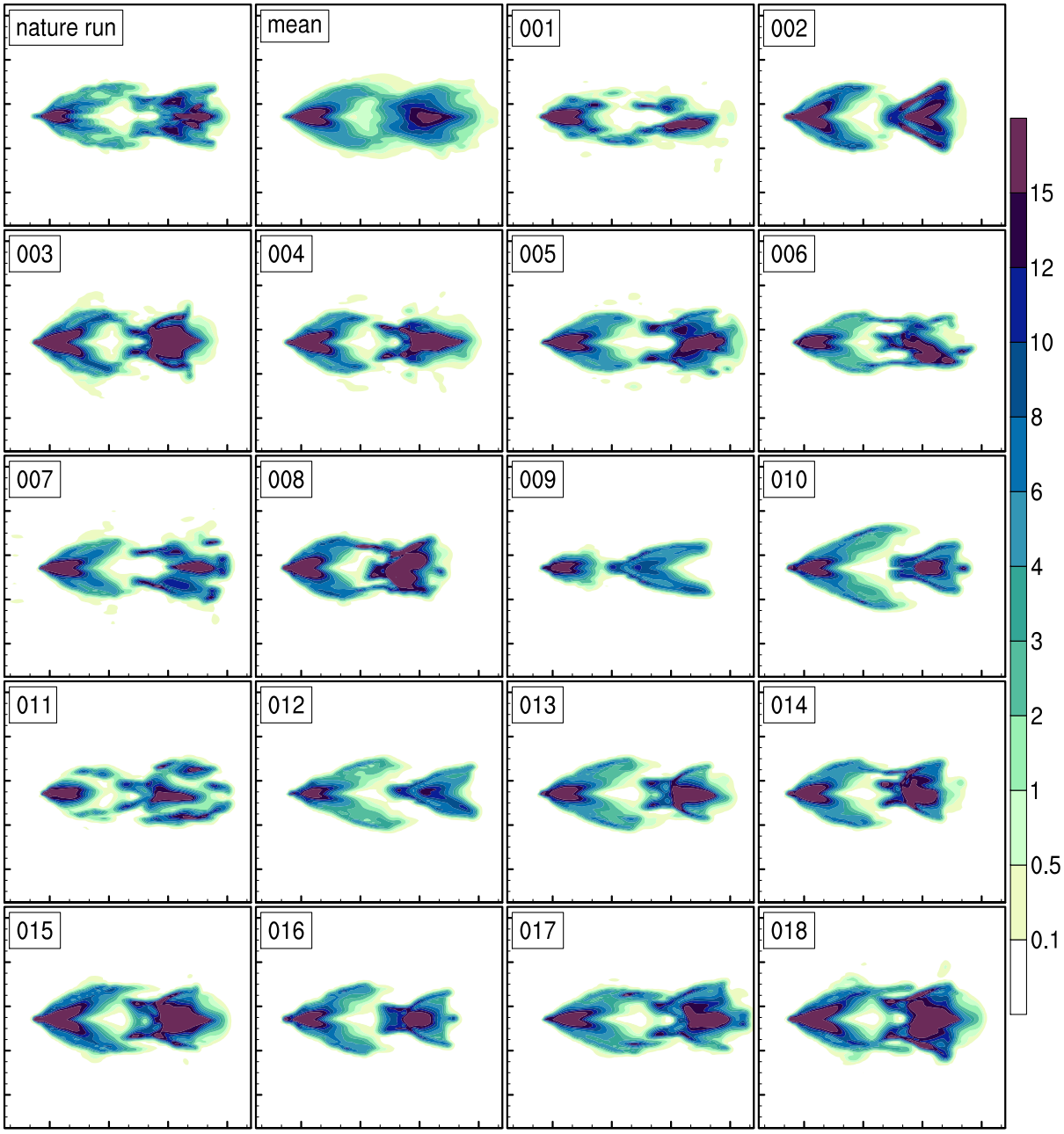


Figure 45: Ensemble ens013. The panels show the accumulated surface precipitation after 5 hours of simulation in units of $\mathrm{kg\,m^{-2}}$ in an area of $75\,\mathrm{km} - 325\,\mathrm{km}$ in x-direction and $50\,\mathrm{km} - 250\,\mathrm{km}$ in y-direction for the nature run, the ensemble mean, and the 18 ensemble members.

### 3.2.6 Comparison of Ensembles

In this section, the ensembles are compared by examining the mean ensemble spread and RMS error for different quantities. The spread can be taken as an indicator for the sensitivity of a storm by taking the strength of perturbation into account. If a small perturbation of a certain quantity leads to a large ensemble spread, the storm is very sensitive to this quantity.

The RMS measures the difference between the ensemble mean and the nature run. It was mentioned in Section 3.2.1, that the different resolutions in the ensemble members and the nature run cause a bias which affects the RMS exceedingly. The bias varies, however, depending on the quantity.

Table 2 contains a selection of averaged spreads, RMS, and their quotient for all ensembles examined in this study. The first six columns describe the values for the time-averaged precipitation maxima and the time-averaged surface wind speed maxima, respectively. These two quantities act as indicators for the intensity of a storm because they only include extreme values. In order to determine the mean spreads and RMS, the time average is calculated. The last three columns contain the accumulated surface precipitation after 5 hours of simulation. These spread and RMS values are calculated by averaging spatially over all grid points with non-zero spread and RMS, respectively.

The spread values indicate that the spread increases with growing perturbation for all perturbations and target quantities. For the first three ensembles, for instance, the spreads

| **Ensemble** | **Precipitation Maxima** | | | **Surface Wind Maxima** | | | **Accumulated Precipitation** | | |
|---|---|---|---|---|---|---|---|---|---|
| | *Spread* | *RMS* | *S/R* | *Spread* | *RMS* | *S/R* | *Spread* | *RMS* | *S/R* |
| ens001 | $0.22\,\mathrm{g\,kg^{-1}}$ | $0.46\,\mathrm{g\,kg^{-1}}$ | 0.48 | $1.20\,\mathrm{m\,s^{-1}}$ | $2.87\,\mathrm{m\,s^{-1}}$ | 0.42 | $0.78\,\mathrm{kg\,m^{-2}}$ | $0.71\,\mathrm{kg\,m^{-2}}$ | 1.10 |
| ens002 | $0.28\,\mathrm{g\,kg^{-1}}$ | $0.48\,\mathrm{g\,kg^{-1}}$ | 0.58 | $1.75\,\mathrm{m\,s^{-1}}$ | $2.80\,\mathrm{m\,s^{-1}}$ | 0.63 | $1.14\,\mathrm{kg\,m^{-2}}$ | $0.70\,\mathrm{kg\,m^{-2}}$ | 1.63 |
| ens003 | $0.38\,\mathrm{g\,kg^{-1}}$ | $0.49\,\mathrm{g\,kg^{-1}}$ | 0.78 | $2.52\,\mathrm{m\,s^{-1}}$ | $2.93\,\mathrm{m\,s^{-1}}$ | 0.86 | $1.55\,\mathrm{kg\,m^{-2}}$ | $0.83\,\mathrm{kg\,m^{-2}}$ | 1.87 |
| ens004 | $0.39\,\mathrm{g\,kg^{-1}}$ | $0.36\,\mathrm{g\,kg^{-1}}$ | 1.08 | $2.95\,\mathrm{m\,s^{-1}}$ | $1.96\,\mathrm{m\,s^{-1}}$ | 1.51 | $0.68\,\mathrm{kg\,m^{-2}}$ | $0.43\,\mathrm{kg\,m^{-2}}$ | 1.58 |
| ens005 | $0.73\,\mathrm{g\,kg^{-1}}$ | $0.31\,\mathrm{g\,kg^{-1}}$ | 2.35 | $5.58\,\mathrm{m\,s^{-1}}$ | $1.09\,\mathrm{m\,s^{-1}}$ | 5.12 | $1.21\,\mathrm{kg\,m^{-2}}$ | $0.58\,\mathrm{kg\,m^{-2}}$ | 2.09 |
| ens006 | $1.03\,\mathrm{g\,kg^{-1}}$ | $0.33\,\mathrm{g\,kg^{-1}}$ | 3.12 | $7.34\,\mathrm{m\,s^{-1}}$ | $1.26\,\mathrm{m\,s^{-1}}$ | 5.83 | $3.30\,\mathrm{kg\,m^{-2}}$ | $1.36\,\mathrm{kg\,m^{-2}}$ | 2.43 |
| ens007 | $0.24\,\mathrm{g\,kg^{-1}}$ | $0.46\,\mathrm{g\,kg^{-1}}$ | 0.52 | $1.86\,\mathrm{m\,s^{-1}}$ | $3.98\,\mathrm{m\,s^{-1}}$ | 0.47 | $0.56\,\mathrm{kg\,m^{-2}}$ | $0.65\,\mathrm{kg\,m^{-2}}$ | 0.86 |
| ens008 | $0.55\,\mathrm{g\,kg^{-1}}$ | $0.38\,\mathrm{g\,kg^{-1}}$ | 1.45 | $5.21\,\mathrm{m\,s^{-1}}$ | $4.14\,\mathrm{m\,s^{-1}}$ | 1.26 | $1.36\,\mathrm{kg\,m^{-2}}$ | $0.89\,\mathrm{kg\,m^{-2}}$ | 1.53 |
| ens009 | $0.84\,\mathrm{g\,kg^{-1}}$ | $0.36\,\mathrm{g\,kg^{-1}}$ | 2.33 | $7.74\,\mathrm{m\,s^{-1}}$ | $4.46\,\mathrm{m\,s^{-1}}$ | 1.74 | $2.90\,\mathrm{kg\,m^{-2}}$ | $1.80\,\mathrm{kg\,m^{-2}}$ | 1.61 |
| ens010 | $0.27\,\mathrm{g\,kg^{-1}}$ | $0.41\,\mathrm{g\,kg^{-1}}$ | 0.66 | $1.60\,\mathrm{m\,s^{-1}}$ | $2.30\,\mathrm{m\,s^{-1}}$ | 0.70 | $0.46\,\mathrm{kg\,m^{-2}}$ | $0.44\,\mathrm{kg\,m^{-2}}$ | 1.05 |
| ens011 | $0.72\,\mathrm{g\,kg^{-1}}$ | $0.34\,\mathrm{g\,kg^{-1}}$ | 2.12 | $4.61\,\mathrm{m\,s^{-1}}$ | $1.16\,\mathrm{m\,s^{-1}}$ | 3.97 | $0.65\,\mathrm{kg\,m^{-2}}$ | $0.39\,\mathrm{kg\,m^{-2}}$ | 1.67 |
| ens012 | $0.78\,\mathrm{g\,kg^{-1}}$ | $0.55\,\mathrm{g\,kg^{-1}}$ | 1.42 | $5.28\,\mathrm{m\,s^{-1}}$ | $2.66\,\mathrm{m\,s^{-1}}$ | 1.98 | $0.72\,\mathrm{kg\,m^{-2}}$ | $0.43\,\mathrm{kg\,m^{-2}}$ | 1.67 |
| ens013 | $0.31\,\mathrm{g\,kg^{-1}}$ | $0.38\,\mathrm{g\,kg^{-1}}$ | 0.82 | $2.07\,\mathrm{m\,s^{-1}}$ | $1.76\,\mathrm{m\,s^{-1}}$ | 1.18 | $0.75\,\mathrm{kg\,m^{-2}}$ | $0.42\,\mathrm{kg\,m^{-2}}$ | 1.79 |

Table 2: Averaged spreads, RMS, and quotients spread/RMS (S/R) of all ensembles evaluated for the precipitation maxima, the surface wind speed maxima, and the accumulated surface precipitation.

of the precipitation maxima, the surface wind maxima, and the accumulated precipitation is approximately doubled from ens001 to ens003. The uncertainties in the storm intensity and storm structure change, thus, similarly with the wind profile perturbation. On the contrary, the perturbation in the relative humidity with constant temperature profile (ens010 to ens012) shows a larger effect on the precipitation and surface wind maxima than on the accumulated precipitation.

For the perturbation strengths of the ensembles, it is paid attention that the spreads of all ensembles lie in the same order of magnitude. Table 2 confirms this tendency. Nonetheless, it can be observed that the spreads increase rapidly with increasing perturbation strengths for some ensembles. For instance, ens006 and ens009 exhibit a large spread in surface wind maxima and accumulated precipitation. The reason can be found in the extremely sensitive reaction of the storm simulations on the temperature perturbations. Moreover, convective storm simulations are also highly sensitive to the perturbations in the humidity. The spreads increase significantly from ens010 to ens011 although the perturbation strength is only doubled. In contrast, perturbations in the horizontal wind speed (ens001, ens002, and ens003) seem to affect the storm simulation less. Compared to the other ensembles, they exhibit the lowest spread in precipitation and wind speed maxima. The spread in the accumulated precipitation is affected by the different storm speeds resulting from the wind perturbation which smooths the ensemble mean out.

In contrast to the spread, the RMS is less affected by the perturbation strengths which suggests that the members spread symmetrically around the ensemble mean and the mean is not strongly affected. This may be a result of the symmetric nature of the perturbations. A low RMS in the precipitation and surface wind maxima show those ensembles which include storms with no secondary cell developments, such as ens005, ens006, ens008, ens009, ens011, and ens012. The storms cease, thus, after 2 hours of simulation. The bias between the ensemble mean and the nature run gets consequently minimized. As a consequence, the ratio of the spread and RMS increases for these ensembles remarkably.

Furthermore, the RMS shows a nice distinction between the different ensemble triples which exhibit different perturbation variables. For example, the surface wind speed shows a larger difference between the ensemble mean and the nature run for ens007 to ens009 than for the ensemble with the wind speed perturbation, the RMS of the precipitation maxima is smaller, however. For ens004 to ens006, the surface wind maxima exhibit a low RMS in all three quantities. This result shows, that the resolution is not the only reason for differences between the ensemble mean and the nature run, but the kind of perturbation plays also a role.

The spread-skill ratio (S/R in Table 2) gives a rough estimate of the skill of the ensemble in predicting the precipitation maxima, the wind speed maxima, and the accumulated precipitation. A value of 1 indicates that the uncertainty of the ensemble and the error is approximately of equal size. The spread-skill ratio gives thus an indication of which perturbation amplitude is most appropriate for this storm case. For example, for the wind perturbation, a standard deviation of $2\,\mathrm{m\,s^{-1}}$ (ens003) gives the best results for precipitation and wind speed maxima (S/R = 0.78 and S/R = 0.86), while for accu-

mulated precipitation, the lowest amplitude $0.5\,\mathrm{m\,s^{-1}}$ is most appropriate (S/R = 1.10). From this analysis it appears that reasonable standard deviations $\sigma_\phi$ are $2\,\mathrm{m\,s^{-1}}$ for wind speed, 0.25 K for temperature and 2 % for relative humidity. A conbination of wind and temperature (ens013) results also in an ensemble with favorable S/R-values. It has to be noted that appropriate perturbation amplitudes are well suited for this case, but is expected to vary considerably from case to case.

Figure 46 illustrates the time evolution of the spread maxima of precipitation. The maximal spread is calculated and plotted as a function of time for all 13 ensembles. Two interesting features can be observed:

- All ensembles have a comparable spread, i.e. there are no ensembles which are extreme outliers. The perturbations are, thus, appropriately chosen.
- All curves nicely follow the development of the convective storms. Many curves exhibit a peak in spread between 30 minutes and 1 hour of simulation. These indicate the initiation of precipitation which is obviously not certain. The initial cell development lies in between 1 and 3 hours. The secondary cell developments

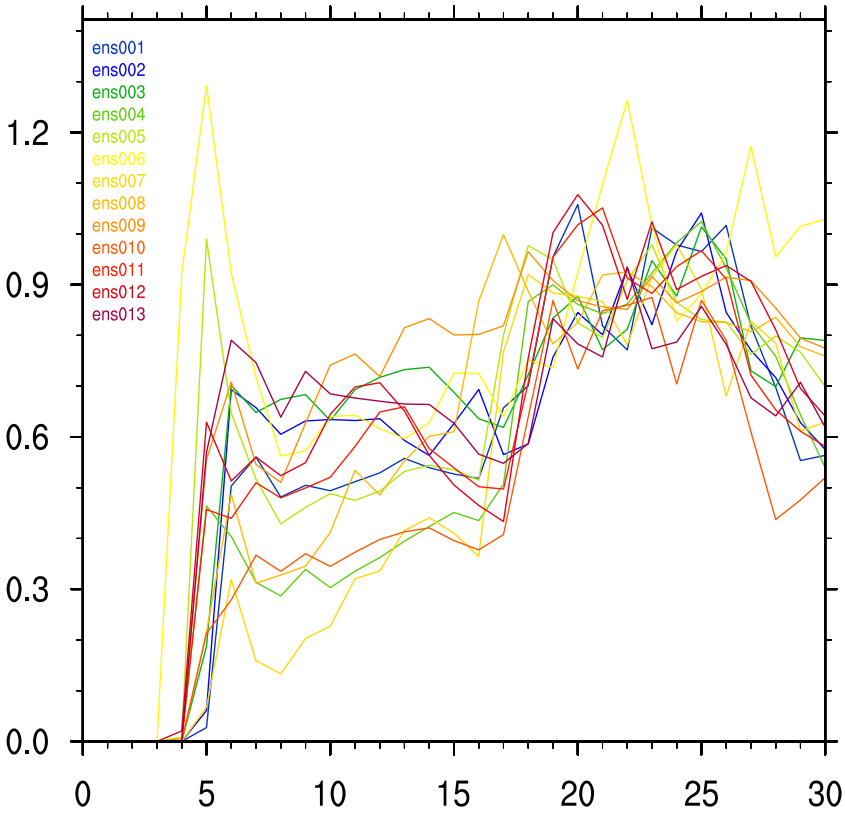


Figure 46: Time evolution of the spreads for all 13 ensembles. The x-axis shows the time in steps of 10 minutes and the y-axis the spread of precipitation in $\mathrm{g\,kg^{-1}}$.

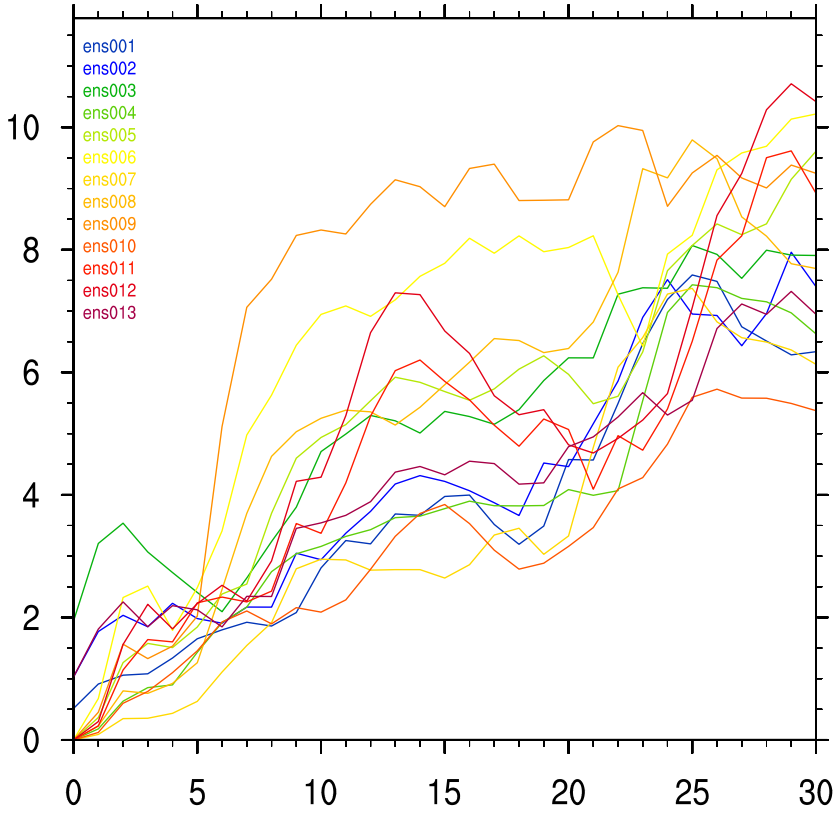


Figure 47: Time evolution of the surface wind speed spreads in $\mathrm{m\,s^{-1}}$ as a function of time in steps of 10 minutes for all 13 ensembles.

around 3 hours of simulation give again rise to an increase of spread and thus a growing uncertainty. The further cell development stays uncertain due to the foregoing unpredictability.

It is, consequently, not easy to predict the exact time when precipitation occurs. Secondary cell developments further lead to an uncertainty which influences the further predictability with time.

Figure 47 shows the spread maxima for the surface wind as a function of time. Similar to the spread maxima of precipitation, all ensembles exhibit a comparable spread evolution with time. In contrast to precipitation, there is a clearer tendency of increasing spread maxima with time for the surface wind. Steep increases in spread can however be observed in some ensembles around 1 hour and close to 4 hours of simulation, i.e. the initiation of heavy precipitation in the initial and secondary cells leads to uncertainties in surface wind speed predictions. Ensembles ens001, ens002, and ens003 show, furthermore, the initial perturbations at time 0.

### 3.2.7 Additional Nature Runs

The last examination compares an ensemble for different nature run storms which vary in the storm triggering bubble. The intention was to study the differences in the ensemble simulations if the initiation strength varies. Two cases are investigated:

- *ens014*: The temperature anomaly, which triggers the convective storm, is decreased to 2 K. The initial updrafts are thus weaker, the storm structure evolves more narrow, and the storm intensity decreases.
- *ens015*: The size of the warm air bubble is increased to $40\,\mathrm{km} \times 40\,\mathrm{km} \times 3\,\mathrm{km}$. The storm is thus larger and brings more extended precipitation.

The perturbations for the ensembles are identical to ens013, i.e., a horizontal wind and temperature perturbation.

Figure 48 shows that the point of initiating precipitation in the nature run and ensemble mean is shifted by a few kilometers between the two ensembles. Due to the weaker bubble of ens014 compared to ens015, the updrafts are weaker, the storm development slower, and precipitation initiates, therefore, later. Due to the weakness of the storm, not all ensemble members exhibit secondary cells which can be seen in the weaker ensemble mean at the front, or the larger spread of ens014. Also the difference image illustrates that precipitation is underestimated especially at the front of the storm. In contrast, the difference image of ens015 looks more balanced because every single ensemble member shows secondary cells.

Table 3, which includes the spreads and RMS of the precipitation maxima, the surface wind maxima, and the accumulated precipitation, illustrates that the accumulated precipitation spreads least for the weakest storm and most for the largest storm. The spread in storm intensity is however largest for the weakest storm which can be explained by the missing secondary cells of some ensemble members. Interesting is the fact, that the RMS is lowest for ens014 and largest for ens015. It seems to have a tendency that the bias to the nature run correlates with the storm intensity.

| **Ensemble** | **Precipitation Maxima** | | | **Surface Wind Maxima** | | | **Accumulated Precipitation** | | |
|---|---|---|---|---|---|---|---|---|---|
| | *Spread* | *RMS* | *S/R* | *Spread* | *RMS* | *S/R* | *Spread* | *RMS* | *S/R* |
| ens013 | $0.31\,\mathrm{g\,kg^{-1}}$ | $0.38\,\mathrm{g\,kg^{-1}}$ | 0.82 | $2.07\,\mathrm{m\,s^{-1}}$ | $1.76\,\mathrm{m\,s^{-1}}$ | 1.18 | $0.75\,\mathrm{kg\,m^{-2}}$ | $0.42\,\mathrm{kg\,m^{-2}}$ | 1.79 |
| ens014 | $0.56\,\mathrm{g\,kg^{-1}}$ | $0.36\,\mathrm{g\,kg^{-1}}$ | 1.56 | $3.80\,\mathrm{m\,s^{-1}}$ | $1.66\,\mathrm{m\,s^{-1}}$ | 2.29 | $0.60\,\mathrm{kg\,m^{-2}}$ | $0.60\,\mathrm{kg\,m^{-2}}$ | 1 |
| ens015 | $0.39\,\mathrm{g\,kg^{-1}}$ | $0.55\,\mathrm{g\,kg^{-1}}$ | 0.71 | $2.43\,\mathrm{m\,s^{-1}}$ | $2.88\,\mathrm{m\,s^{-1}}$ | 0.84 | $0.98\,\mathrm{kg\,m^{-2}}$ | $0.66\,\mathrm{kg\,m^{-2}}$ | 1.48 |

Table 3: Averaged spreads, RMS, and quotients spread/RMS (S/R) of the ensembles ens013, ens014, and ens015 evaluated for the precipitation maxima, the surface wind speed maxima, and the accumulated surface precipitation.

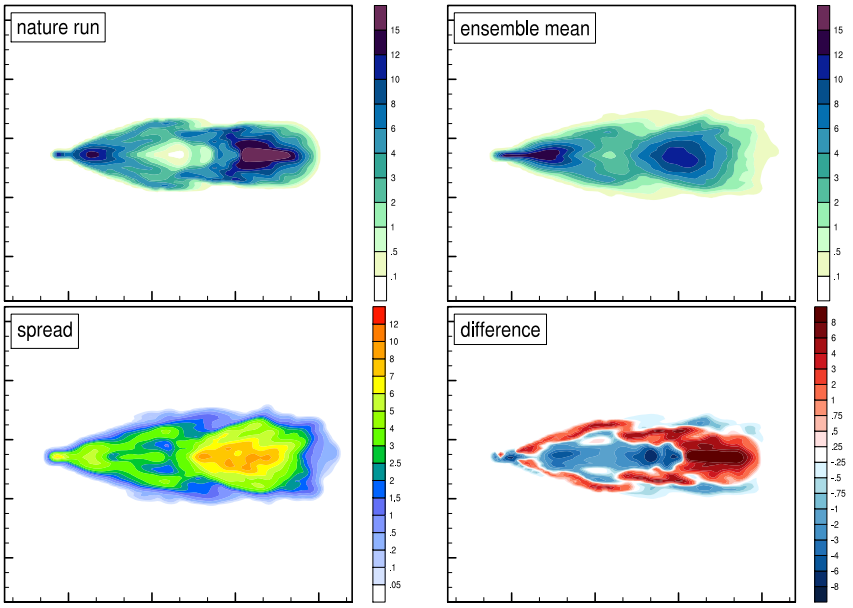


(a) ens014

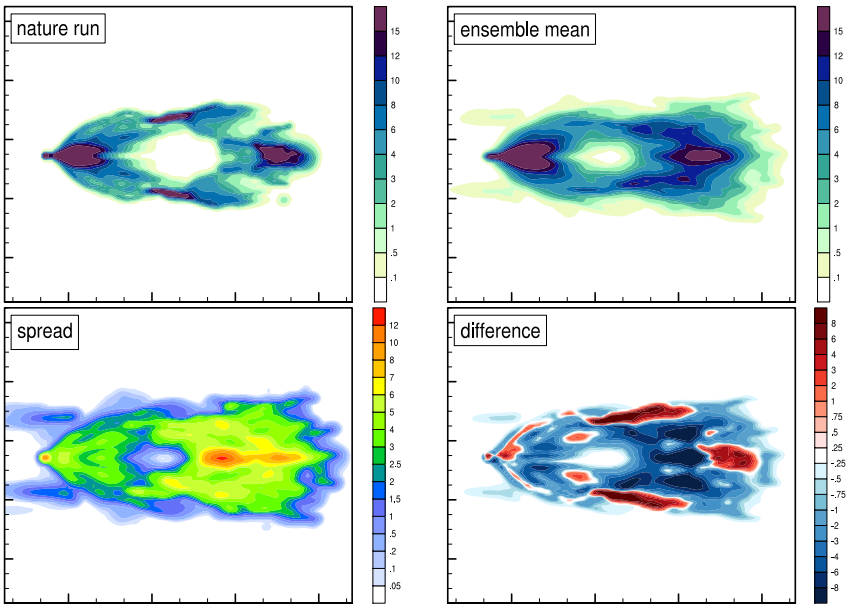


(b) ens015

Figure 48: Ensembles ens014 (a) and ens015 (b). The accumulated surface precipitation in units of $\mathrm{kg\,m^{-2}}$ is plotted in the top left panels for the nature runs and in the top right panels for the ensemble means. The bottom panels exhibit the standard deviation on the left and the differences between the nature runs and the ensemble means on the right (red (blue) colors for larger nature run (ensemble mean) values).

# 4 Summary and Conclusion

The current study presented ensemble simulations of convective storms with the non-hydrostatic atmospheric COSMO model. Different perturbations for the ensemble generation were investigated and their impact on the storm structure and evolution of the different ensemble members and the resulting statistical ensemble characteristics were described.

The storm environment was based on the Payerne sounding at 12 UTC 30 July 2008, a typical Swiss summer convective day. The model was set up in an idealized mode with the sounding used as horizontally homogeneous initial and constant boundary conditions. A flat, lower boundary was specified and the model parameterizations were restricted to turbulence and microphysics. Convection was triggered by a warm temperature anomaly.

In order to find a suitable model setup and to get familiar with the modeling environment, a nature run was simulated first with a high resolution of 1 km mesh grid. It provides a reference, against which the ensemble simulations could be compared. Many characteristic features of convective storms could be identified in this simulation:

- The convective storm consists of many cycles of single updraft-downdraft cells developing and decaying with a lifetime of a few tens of minutes. They interact and trigger further cell life cycles.

- The updrafts cause a vertical component of the vorticity. This vertical vorticity and pressure gradient forces lead to a splitting of the cells in two counter-rotating parts.

- Condensation arises due to lifting of warm, humid air from the lower atmospheric levels and leads to the formation precipitating hydrometeors which cause vigorous downdrafts. The falling, cooler air diverges at the ground and builds a spreading cold pool.

- At the edge of the cold pool, the so-called gust front, convergence and further lifting of warm, humid air occur that favor triggering of new convective cells.

- Precipitation maxima occur preferably at the base updraft-downdraft cells. Close to these locations or right behind the gust front, the surface wind speed reaches its maximal strength.

The ensemble simulations were run using the same model setup as the nature run except for the horizontal mesh size, which was chosen to be 2 km. Perturbations with different amplitudes of wind speed, temperature and humidity, representative for typical observation uncertainties, were applied to the sounding in order to generate different members of ensemble simulations. The ensemble simulations were investigated regarding ensemble mean and spread of integral and isolated storm characteristics, such as accumulated areal precipitation and maximum precipitation intensity. Furthermore, the size of

the precipitation area, maximum wind gusts, and the temporal storm evolution at specific points within the storm track was examined during 5 hours of simulation. The main results and answers to the questions of Section 1.4 can be summarized as follows:

- It was found that wind speed, temperature and humidity are all suited to produce ensemble perturbations for the generation of convective ensemble simulations.
- The ensemble spread is directly proportional to the perturbation amplitude in all cases and all variables.
- Appropriate perturbation standard deviations $\sigma_\phi$ are $2\,\mathrm{m\,s^{-1}}$ for horizontal wind, 0.25 K for temperature, and 2 % for relative humidity.
- Due to the difference in the mesh size, the nature run and the ensemble simulations show systematic differences in wind speed and precipitation: Both, wind and precipitation, were found to be more intense in the 2 km simulations compared to the nature run interpolated to the 2 km grid. This bias seems to be dependent on the intensity of the reference simulation. Weaker simulations show a smaller bias compared to more intense storm simulations.
- *Wind speed perturbations*: The convective storms are affected by the different wind profiles in storm propagation speed and the vertical vorticity of the rotating updrafts. The vertical vorticity is responsible for the splitting of the initial cell. A large vertical vorticity leads to an early splitting and the two cells move rapidly apart and stay close to the gust front which favors the supply of the cell and the generation of new convective updrafts. Ensemble members with weaker vertical vorticity are less intense and produce less precipitation. The differences in the storm speed lead to a horizontally smoothing out of the ensemble mean of accumulated precipitation, the main structures of the storm are, however, well reproduced.
- *Temperature perturbations*: The temperature was perturbed in two different ways: once with relative humidity and once with specific humidity kept constant. The convective storms are highly sensitive to these perturbations. Crucial for these ensembles are the CAPE (mainly determined by the low-level specific humidity) and the vertical vorticity. These quantities are strongly correlated and determine the storm structure. Severe and intense storms are characterized by large CAPE values (caused by a moist low-level atmosphere) and a large vertical vorticity. In the case with constant specific humidity, the CAPE values do not differ much between the ensemble members. In this case, the variations in low-level stability, caused by the different temperature profiles and associated variations in low-level buoyancy and updrafts, are responsible for different storm evolutions.
- *Relative humidity perturbations*: The relative humidity is correlated to the specific humidity when the temperature profile is kept constant. Essential for the convective

storm simulations are again the variations in the low-level specific humidity. They determine the CAPE and control the updrafts of the initial cell. It was found that more intense storms show larger updrafts in the lower atmosphere (below $\sim 500\,\mathrm{hPa}$) which leads to a stronger convergence in the lowest levels, favoring vigorous convection.

- *Combined perturbations*: By combining the horizontal wind speed perturbations with the temperature perturbations, the effects, found in the ensembles with isolated perturbations, interfere and can either lead to an enhancement or a reduction of the storm intensity. A combination of $\sigma_\phi = 1\,\mathrm{m\,s^{-1}}$ and $\sigma_\phi = 0.25\,\mathrm{K}$ results in a skillful ensemble.

- An examination of the passage of the convective storm at a specific fixed point within the track of the storm revealed that the drop in temperature and the increase in surface wind, which mark the arrival of the gust front, as well as the initiating precipitation, are well captured. The ensemble spread illustrates that the exact timing of the storm arrival and intensity is very sensitive to all chosen perturbations and thus difficult to predict.

In summary, the ensemble simulations helped to evaluate the sensitivity of convective storms and the chosen perturbations lead to sensible ensemble simulations. The idealized model setup and the perturbation strategy is judged suitable as a testbed for ensemble data assimilation methods, such as the Ensemble Kalman Filter. In particular, a combined wind speed and temperature perturbation was found beneficial.

In order to judge more thoroughly which sounding variable is the most suitable to perturb for a skillful ensemble, a larger number of cases with different convective environments should be investigated. Moreover, in this work, only perturbations to the environmental profiles have been studied. There are a number of other perturbations that could be added and could be beneficial for ensemble generation, e.g., variations in the horizontal structure of the storm environment or perturbations of the model physics tendencies as a proxy for model error. These topics are subject for future research.

# 5 Acknowledgments

I want to thank all people who supported me and helped to achieve interesting results. A special thank belongs to my two supervisors, i.e., Dr. Daniel Leuenberger, who supervised this thesis at MeteoSwiss and provided all tools needed for this study, and Prof. Dr. Heini Wernli, who enabled this thesis in collaboration with the IACETH. Both made a large contribution to the successful completion of this master thesis. I am also indebted to Dr. André Walser and Dr. Andreas Weigel for useful discussions and expert inputs concerning ensemble verification. And finally, I am grateful to all reviewers of this thesis.

# References

[1] Aksoy, A., D. Dowell, and C. Snyder, 2009: A Multicase Comparative Assessment of the Ensemble Kalman Filter for Assimilation of Radar Observations - part I: Short-Scale Analyses. Mon. Wea. Rev., 137, 1805-1824.

[2] Buizza, R., 2000: *Chaos and Weather Prediction*, ECMWF Lecture Notes.

[3] Byers, H. R. and R. R. Braham, 1949: *The Thunderstorm*, U. S. Dept. of Commerce, Washington.

[4] Doms, G. and U. Schättler, 2002: A description of the nonhydrostatic regional model LM. - Part I: Dynamics and Numerics. Deutscher Wetterdienst (DWD), Offenbach.

[5] Dowell, D. C., L. J. Wicker, 2009: Additive Noise for Storm-Scale Ensemble Data Assimilation, J. Atmos. Oceanic Technol., 26, 911-927.

[6] Evensen, G., 1994: Sequential data assimilation with a nonlinear quasi-geostrophic model using Monte Carlo methods to forecast error statistics, J. Geophys. Res., 99 (C5), 10 143-10 162.

[7] Fiori, E., A. Parodi, and F. Siccardi, 2010: Turbulence Closure Parametrization and Grid Spacing Effects in Simulated Supercell Storms, J. Atmos. Sci., 67, 3870-3890

[8] Hamill, T.M., J.S. Whitaker, and X. Wei, 2004: Ensemble reforecasting: improving medium-range forecast skill using retrospective forecasts. Mon. Wea. Rev., 132, 1434-1447.

[9] Lemon, L. R. and C. A. Doswell, 1979: Severe Thunderstorm Evolution and Mesocyclone Structure as Related to Tornadogenesis, Mon. Wea. Rev., 107, 1184-1197.

[10] Marwitz, J. D., 1972a: The structure and motion of severe hailstorms - part I: supercell storms, J. Appl. Meteor., 11, 166-179.

[11] Marwitz, J. D., 1972b: The structure and motion of severe hailstorms - part II: mult-cell storms, J. Appl. Meteor., 11, 180-188.

[12] Morel, C. and S. Senesi, 2002: A Climatology of Mesoscale Convective Systems over Europe using Satellite Infrared Imagery.II: Characteristics of European Mesoscale Convective Systems.

[13] Schättler, U., G. Doms, C. Schraff, 2009: A Description of the Nonhydrostatic Regional COSMO-Model, Part VII: User's Guide, Deutscher Wetterdienst.

[14] Schiesser, H. H. et al., 1995: The Mesoscale Structure of Severe Precipitation Systems in Switzerland, Mon. Wea. Rev., 123, 2070-2097.

[15] Sivillo, J. E., J. E. Ahlquist, and Z. Toth, 1997: An Ensemble Forecasting Primer, Wea. Forecasting, 12, 809-817

[16] Snyder, C. and F. Zhang, 2003: Assimilation of Simulated Doppler Radar Observations with an Ensemble Kalman Filter*. Mon. Wea. Rev., 131, 1663-1677.

[17] Wallace, J. M. and P. V. Hobbs, 2006: *Atmospheric Science - An Introductory Survey*, 2nd ed., Elsevier Academic Press, Amsterdam.

[18] Weigel, A. P., 2011. *Verification of Ensemble Forecasts*. In: Forecast Verification [eds. I.T. Jolliffe and D.B. Stephenson]. 2nd edition. John Wiley & Sons Ltd. In press.

[19] Weisman, M. L. and J. B. Klemp, 1982: The Dependence of Numerically Simulated Convective Storms on Vertical Wind Shear and Buoyancy, Mon. Wea. Rev., 110, 504-520.

[20] Weisman, M. L. and J. B. Klemp, 1984: The Structure and Classification of Numerically Simulated Convective Storms in Directionally Varying Wind Shears, Mon. Wea. Rev., 112, 2479-2498.

[21] NOAA Ensemble Training, June 29, 2011: `http://www.hpc.ncep.noaa.gov/ensembletraining`

[22] COSMO: `http://www.cosmo-model.org`

[23] Tagesanzeiger, May 24, 2011: `http://www.tagesanzeiger.ch/panorama/vermischtes/Der-Sturm-hat-die-Stadt-halbiert/story/28362757`

# Appendix

In this section, many plots, that are not shown in the main part of the thesis, are gathered for completeness. It allows the comparison of all 15 ensembles which were simulated in the context of this study. The first figures of each ensemble give an idea of the ensemble means, the ensemble spreads, and the differences between the ensemble means and the nature run. The second figures of each ensemble, which contain the panel plots of the accumulated precipitation for all ensemble members after 5 hours of simulation, show the different storm structures and help to estimate the influence of each perturbation. In order to compare the storm intensities, its time evolution, and the uncertainties in prediction, the box plots of the precipitating hydrometeor and the surface wind speed maxima are added as third figures of each ensemble.

## Horizontal Wind Perturbation

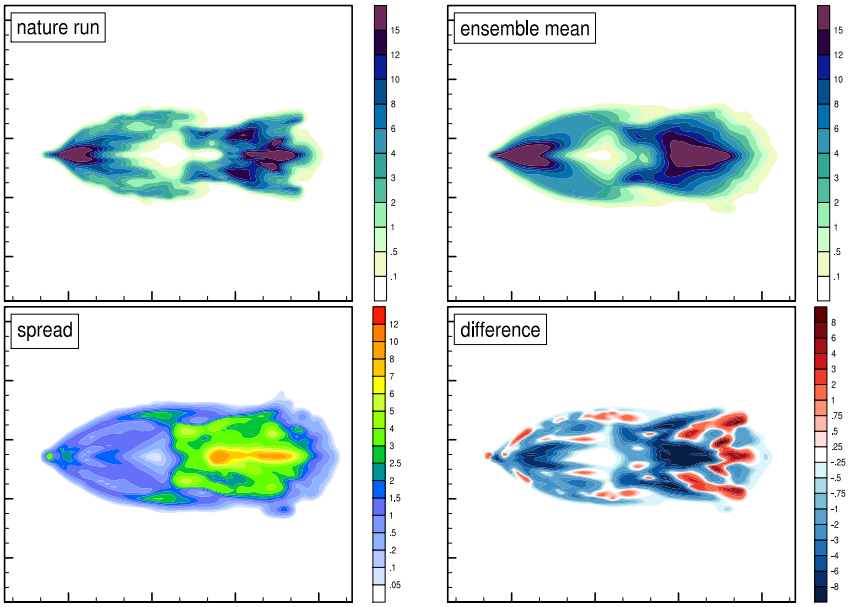


Figure 49: Ensemble ens001. The accumulated surface precipitation in units of $\mathrm{kg\,m^{-2}}$ is plotted in the top left panel for the nature run and in the top right panel for the ensemble mean. The bottom panels exhibit the standard deviation on the left and the differences between the nature run and the ensemble mean on the right (red (blue) colors for larger nature run (ensemble mean) values).

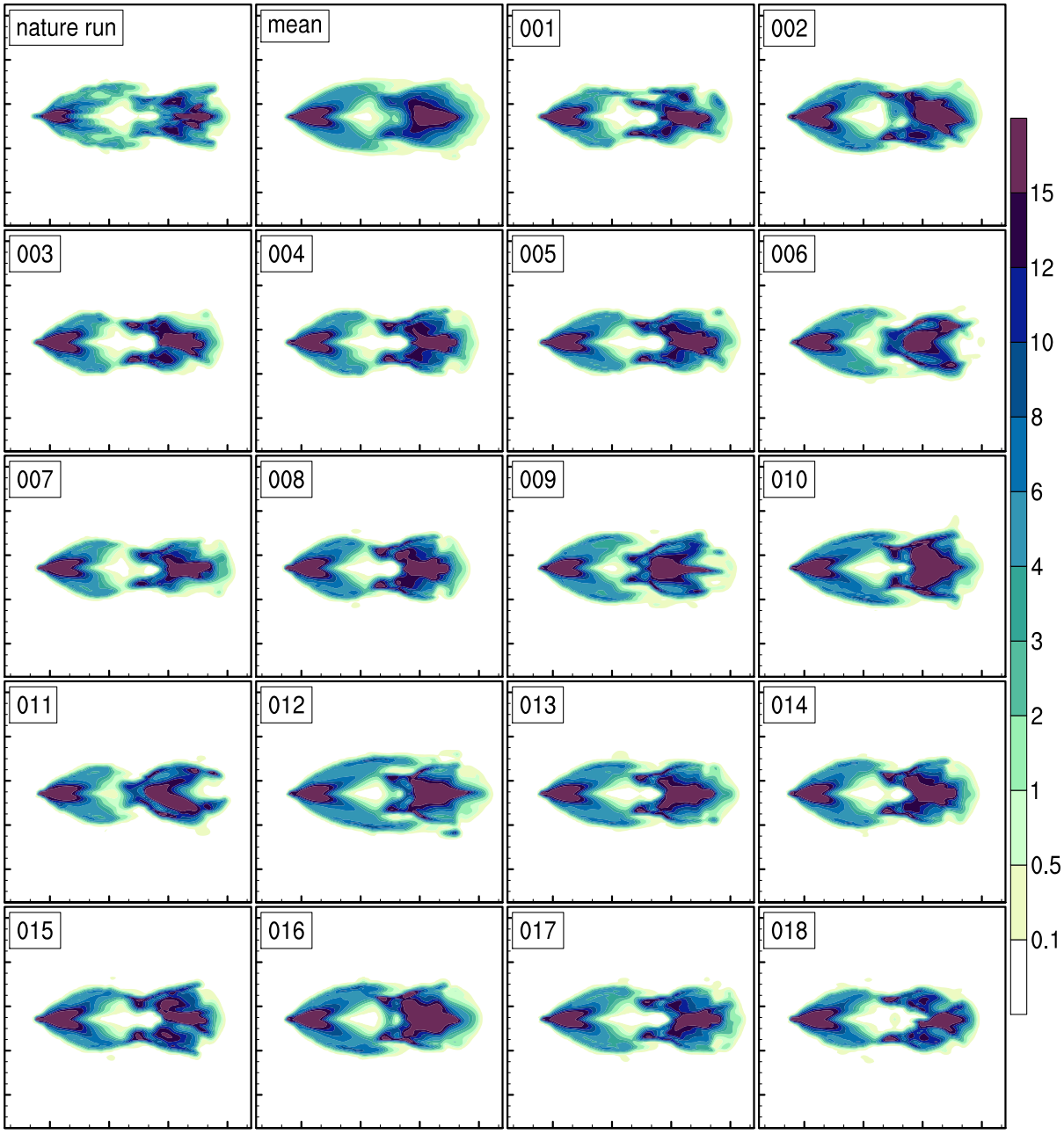


Figure 50: Ensemble ens001. The panels show the accumulated surface precipitation after 5 hours of simulation in units of $\mathrm{kg\,m^{-2}}$ in an area of $75\,\mathrm{km} - 325\,\mathrm{km}$ in x-direction and $50\,\mathrm{km} - 250\,\mathrm{km}$ in y-direction for the nature run, the ensemble mean, and the 18 ensemble members.

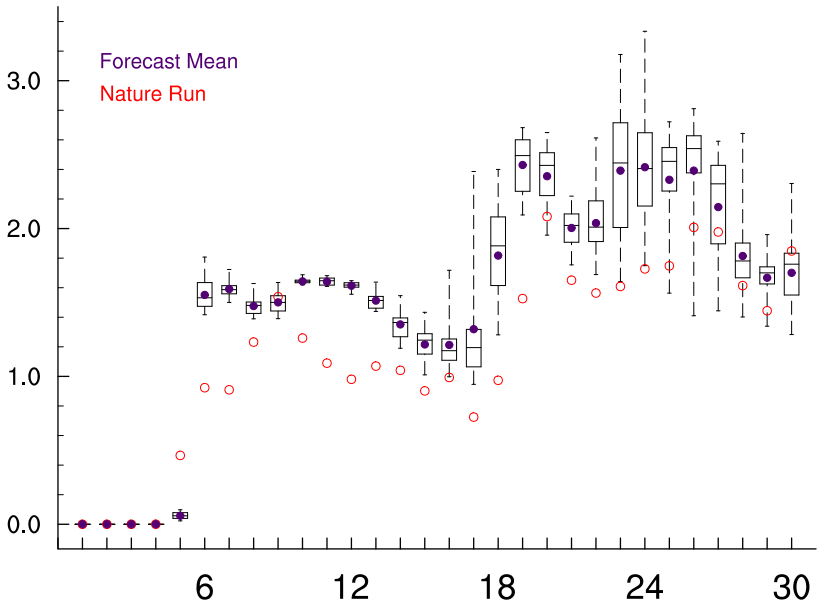


(a) precipitation maxima

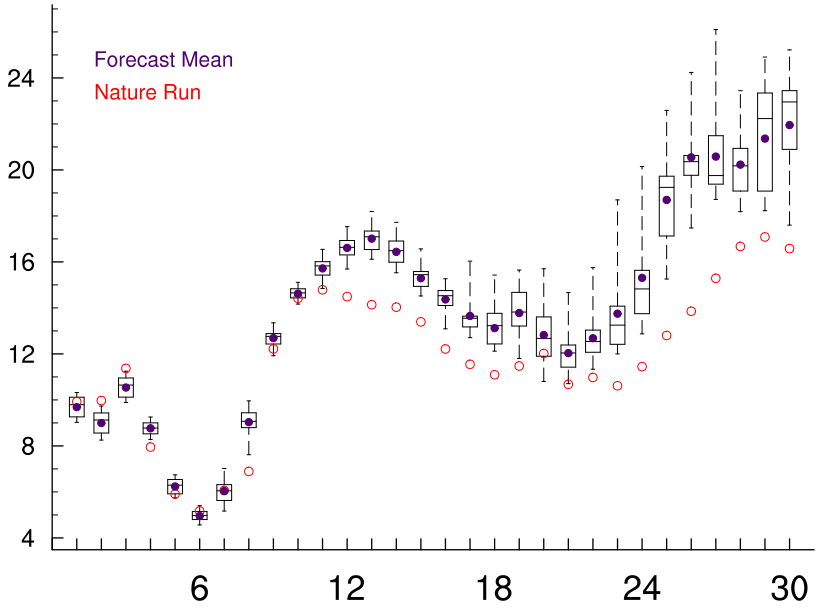


(b) surface wind maxima

Figure 51: Box plot of the precipitating hydrometeors in the lowest level in $\mathrm{g\,kg^{-1}}$ (a) and the surface wind speed maxima in $\mathrm{m\,s^{-1}}$ (b) as a function of time in steps of 10 minutes for the ensemble ens001.

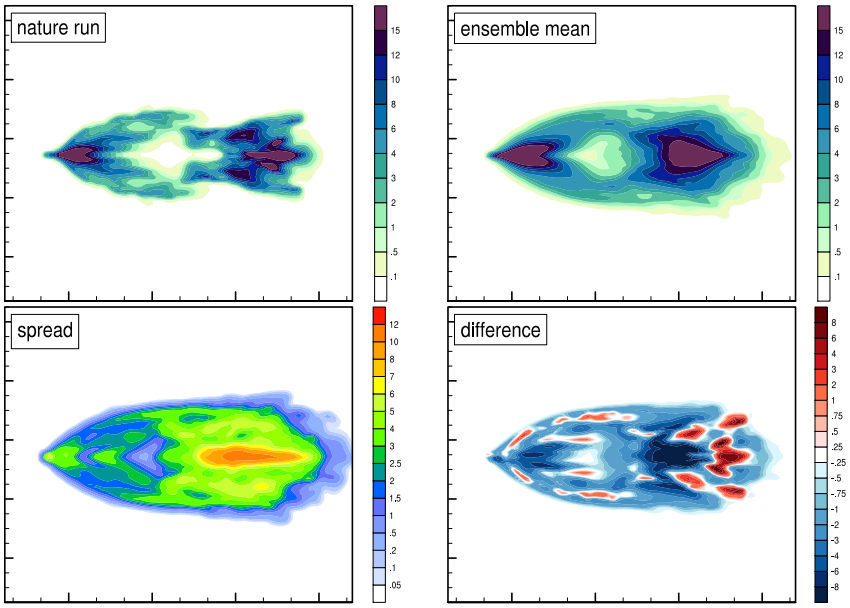


Figure 52: Ensemble ens002. The accumulated surface precipitation in units of $\mathrm{kg\,m^{-2}}$ is plotted in the top left panel for the nature run and in the top right panel for the ensemble mean. The bottom panels exhibit the standard deviation on the left and the differences between the nature run and the ensemble mean on the right (red (blue) colors for larger nature run (ensemble mean) values).

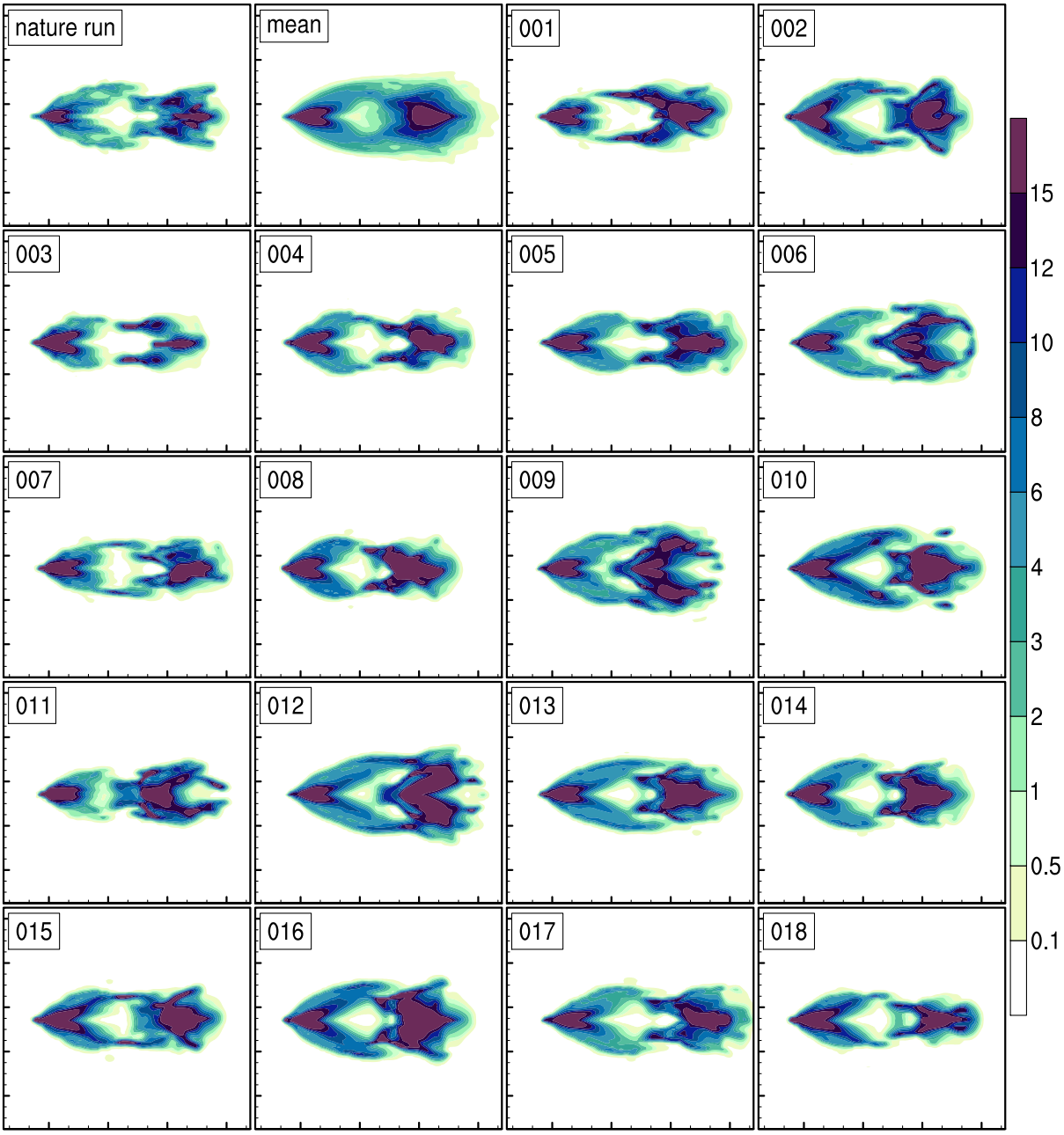


Figure 53: Ensemble ens002. The panels show the accumulated surface precipitation after 5 hours of simulation in units of $\mathrm{kg\,m^{-2}}$ in an area of $75\,\mathrm{km} - 325\,\mathrm{km}$ in x-direction and $50\,\mathrm{km} - 250\,\mathrm{km}$ in y-direction for the nature run, the ensemble mean, and the 18 ensemble members.

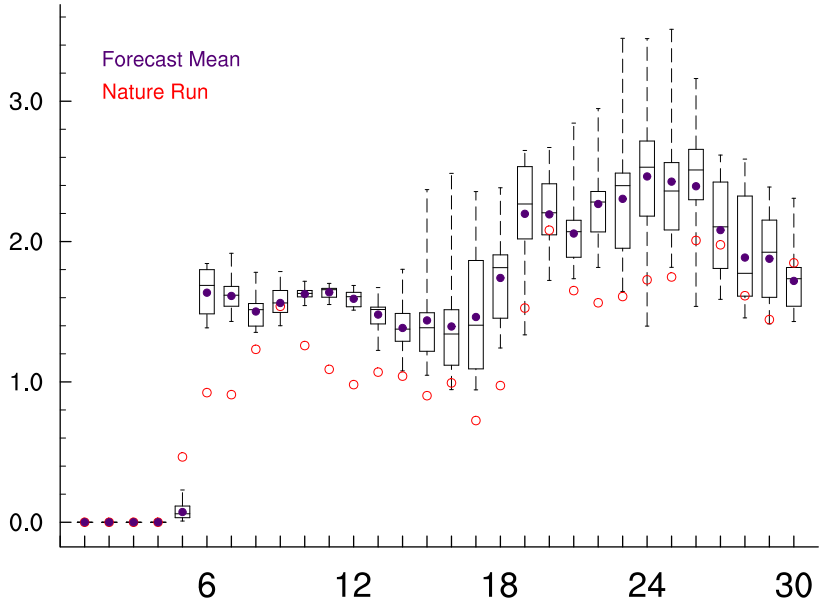


(a) precipitation maxima

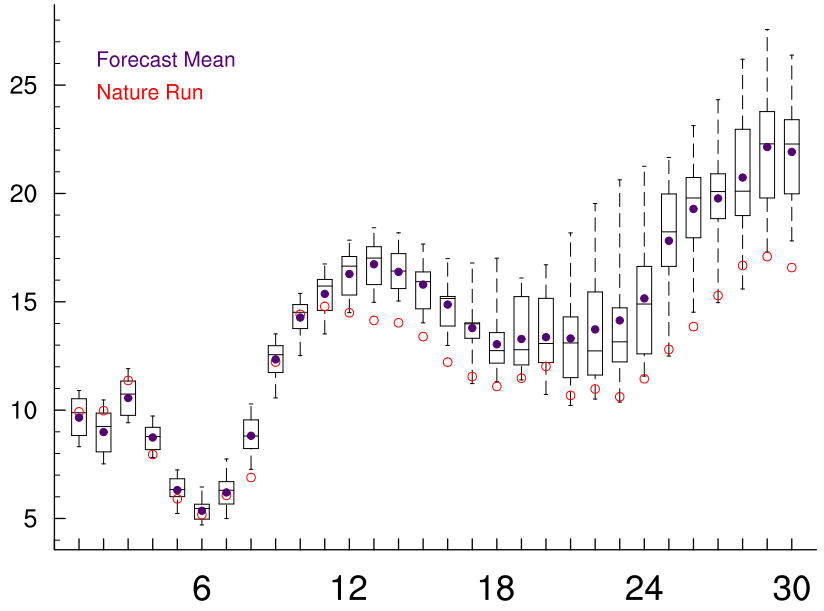


(b) surface wind maxima

Figure 54: Box plot of the precipitating hydrometeors in the lowest level in $\mathrm{g\,kg^{-1}}$ (a) and the surface wind speed maxima in $\mathrm{m\,s^{-1}}$ (b) as a function of time in steps of 10 minutes for the ensemble ens002.

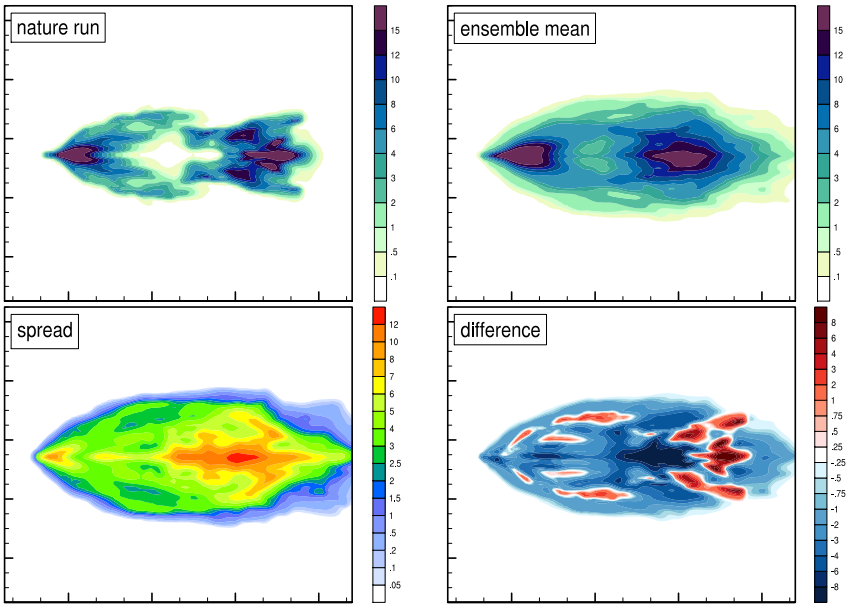


Figure 55: Ensemble ens003. The accumulated surface precipitation in units of $\mathrm{kg\,m^{-2}}$ is plotted in the top left panel for the nature run and in the top right panel for the ensemble mean. The bottom panels exhibit the standard deviation on the left and the differences between the nature run and the ensemble mean on the right (red (blue) colors for larger nature run (ensemble mean) values).

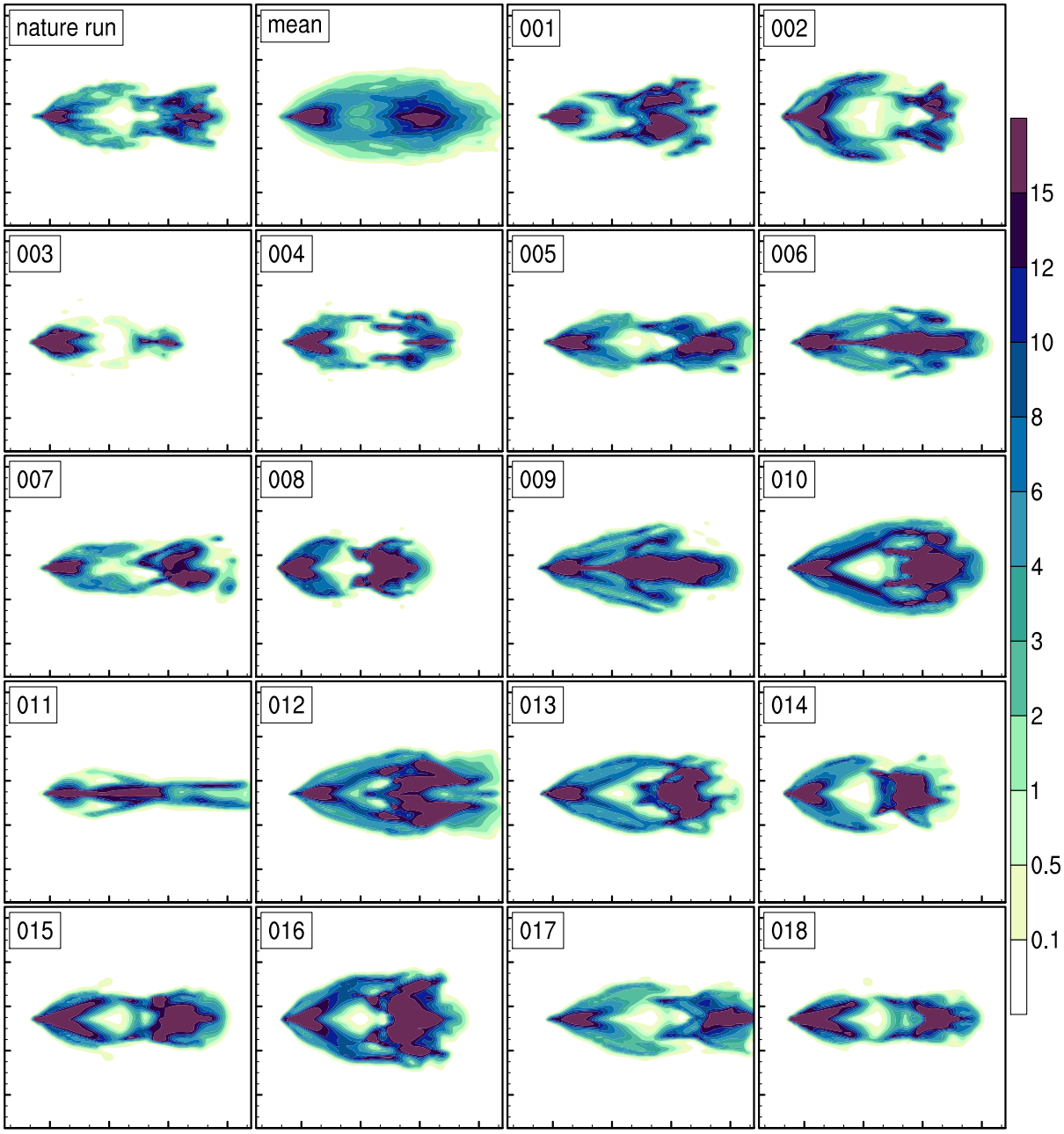


Figure 56: Ensemble ens003. The panels show the accumulated surface precipitation after 5 hours of simulation in units of $\mathrm{kg\,m^{-2}}$ in an area of $75\,\mathrm{km} - 325\,\mathrm{km}$ in x-direction and $50\,\mathrm{km} - 250\,\mathrm{km}$ in y-direction for the nature run, the ensemble mean, and the 18 ensemble members.

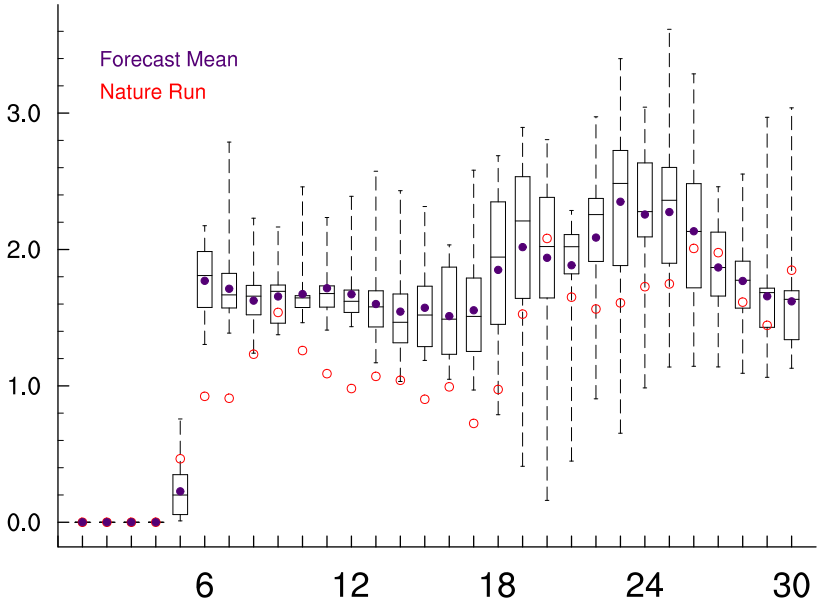


(a) precipitation maxima

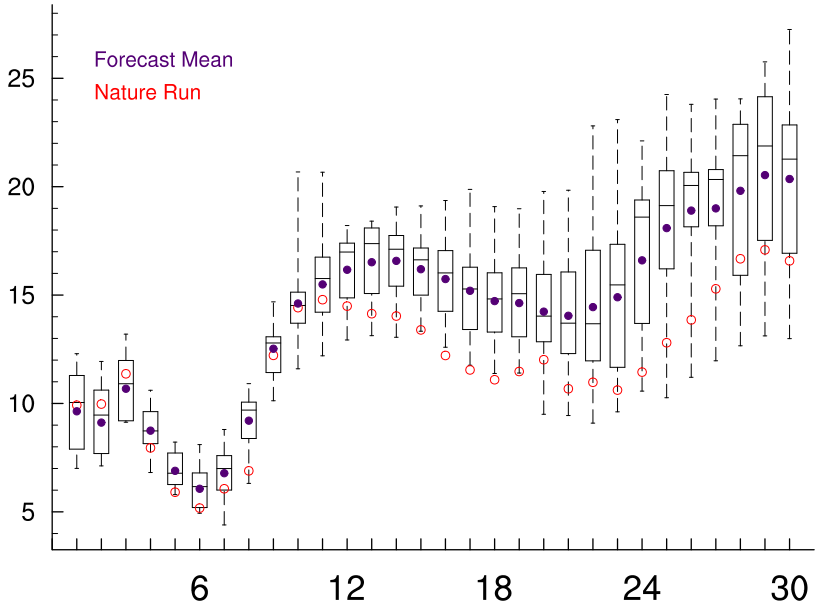


(b) surface wind maxima

Figure 57: Box plot of the precipitating hydrometeors in the lowest level in $\mathrm{g\,kg^{-1}}$ (a) and the surface wind speed maxima in $\mathrm{m\,s^{-1}}$ (b) as a function of time in steps of 10 minutes for the ensemble ens003.

## Temperature Perturbation with Constant Relative Humidity

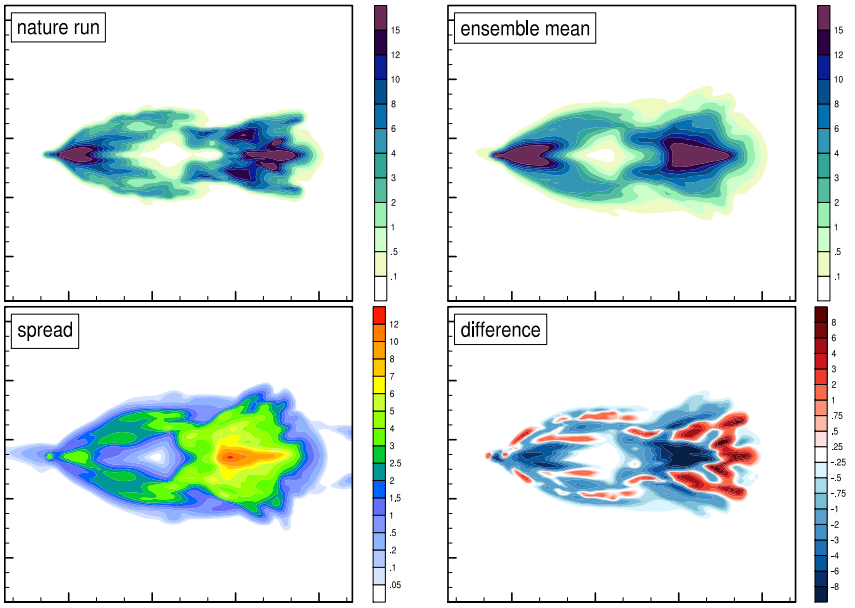


Figure 58: Ensemble ens004. The accumulated surface precipitation in units of $\mathrm{kg\,m^{-2}}$ is plotted in the top left panel for the nature run and in the top right panel for the ensemble mean. The bottom panels exhibit the standard deviation on the left and the differences between the nature run and the ensemble mean on the right (red (blue) colors for larger nature run (ensemble mean) values).

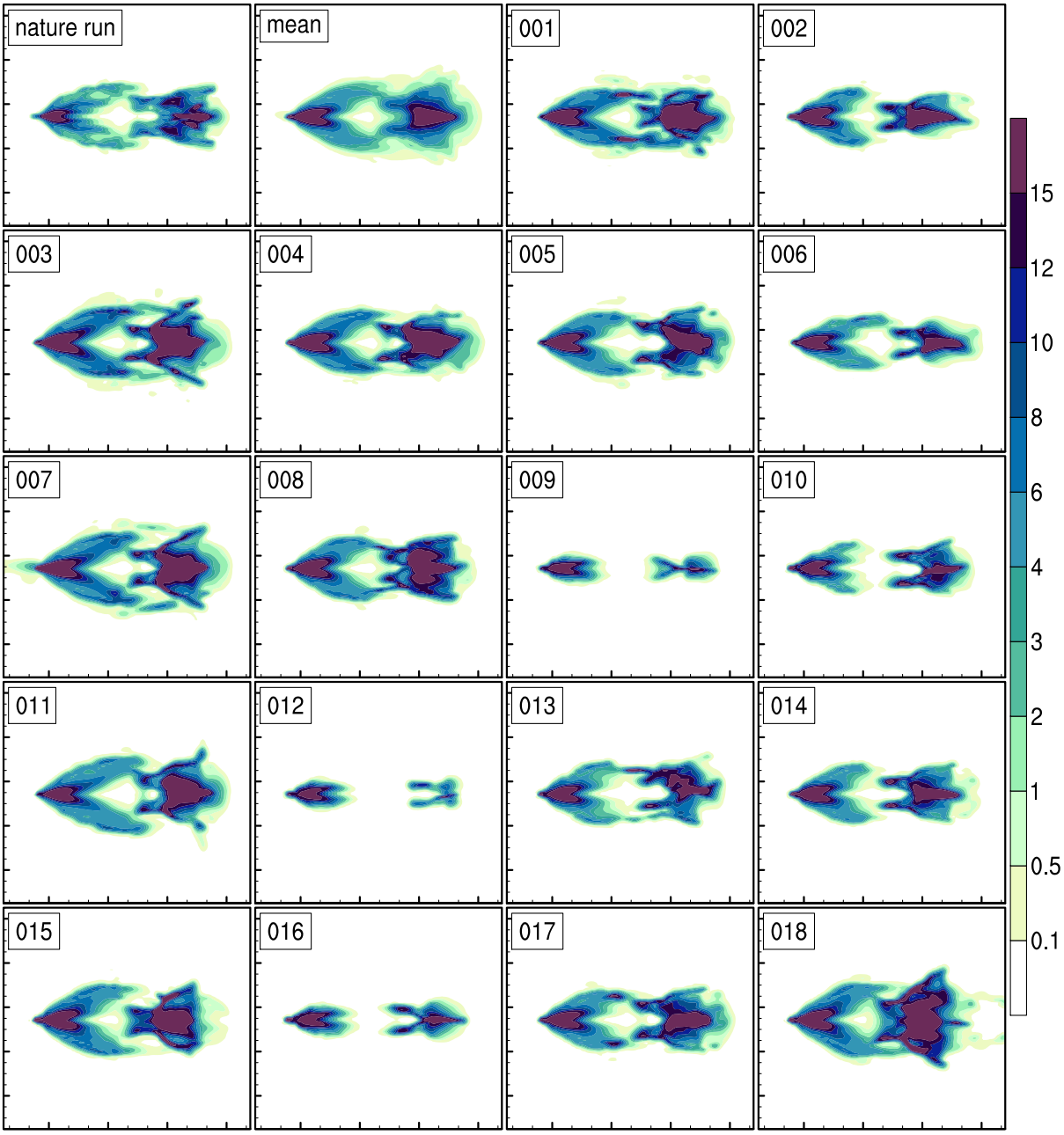


Figure 59: Ensemble ens004. The panels show the accumulated surface precipitation after 5 hours of simulation in units of $\mathrm{kg\,m^{-2}}$ in an area of $75\,\mathrm{km} - 325\,\mathrm{km}$ in x-direction and $50\,\mathrm{km} - 250\,\mathrm{km}$ in y-direction for the nature run, the ensemble mean, and the 18 ensemble members.

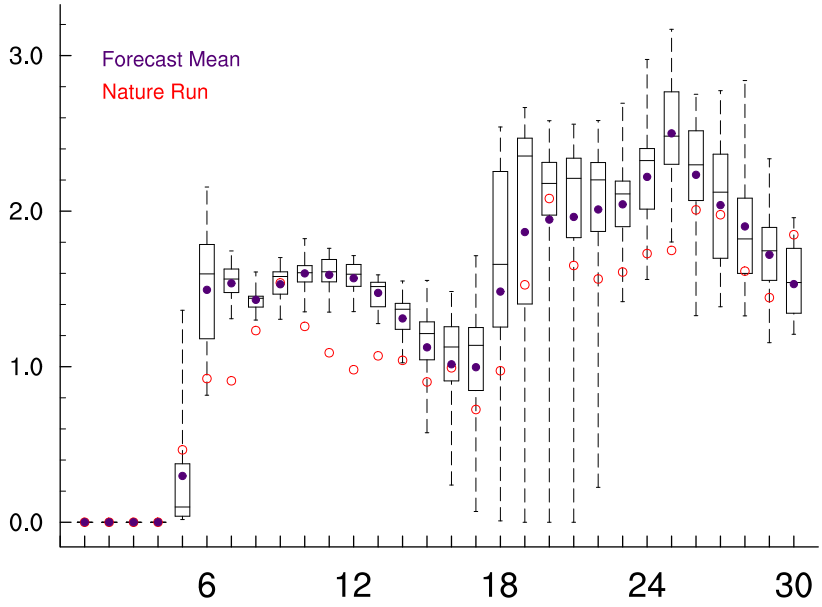


(a) precipitation maxima

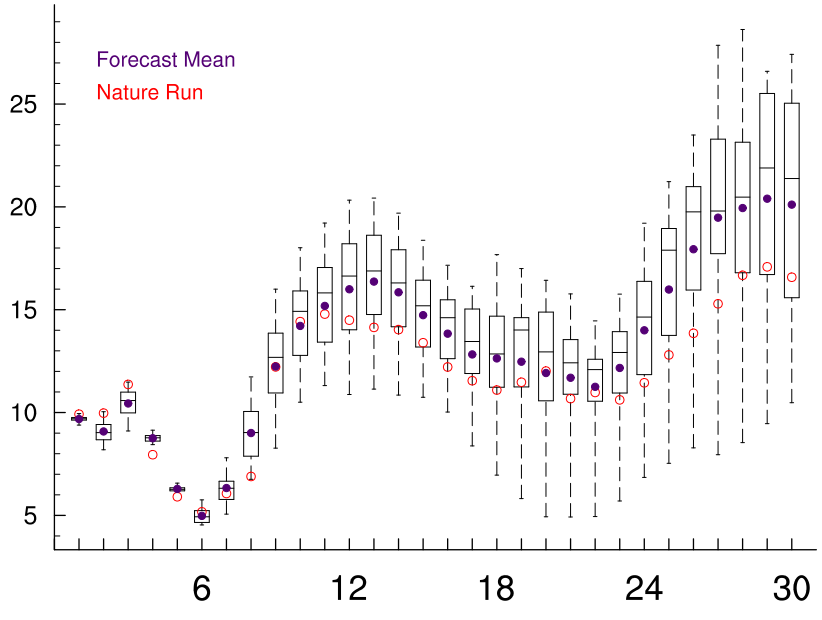


(b) surface wind maxima

Figure 60: Box plot of the precipitating hydrometeors in the lowest level in $\mathrm{g\,kg^{-1}}$ (a) and the surface wind speed maxima in $\mathrm{m\,s^{-1}}$ (b) as a function of time in steps of 10 minutes for the ensemble ens004.

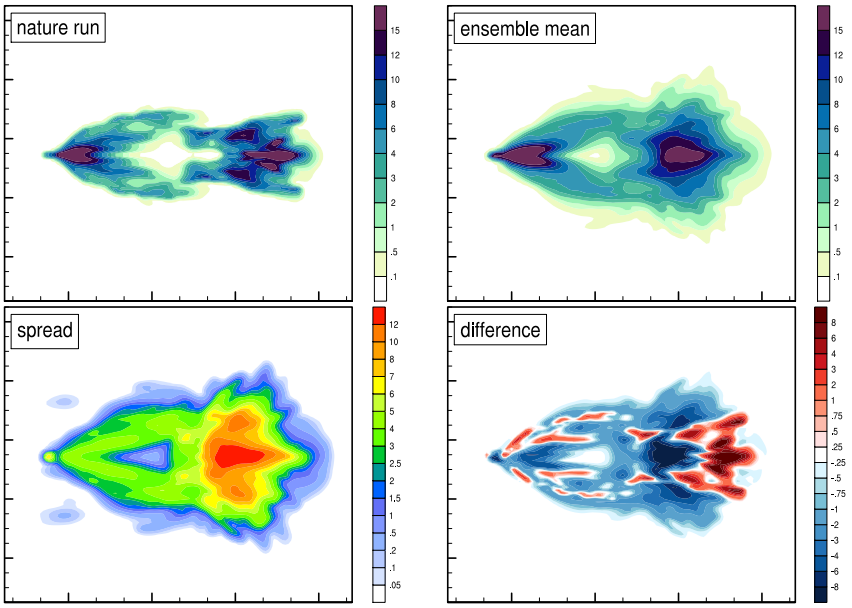


Figure 61: Ensemble ens005. The accumulated surface precipitation in units of $\mathrm{kg\,m^{-2}}$ is plotted in the top left panel for the nature run and in the top right panel for the ensemble mean. The bottom panels exhibit the standard deviation on the left and the differences between the nature run and the ensemble mean on the right (red (blue) colors for larger nature run (ensemble mean) values).

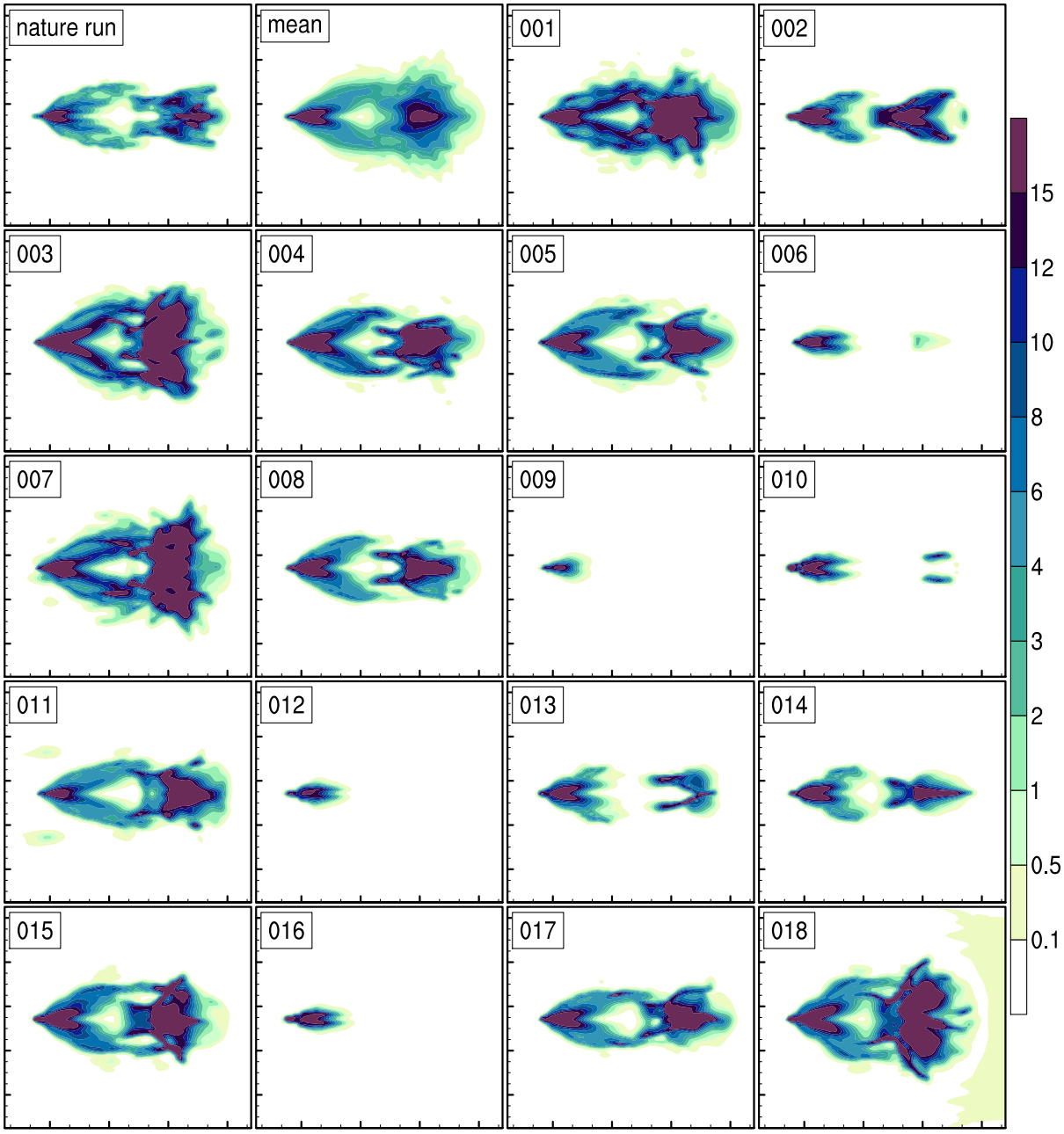


Figure 62: Ensemble ens005. The panels show the accumulated surface precipitation after 5 hours of simulation in units of $\mathrm{kg\,m^{-2}}$ in an area of $75\,\mathrm{km} - 325\,\mathrm{km}$ in x-direction and $50\,\mathrm{km} - 250\,\mathrm{km}$ in y-direction for the nature run, the ensemble mean, and the 18 ensemble members.

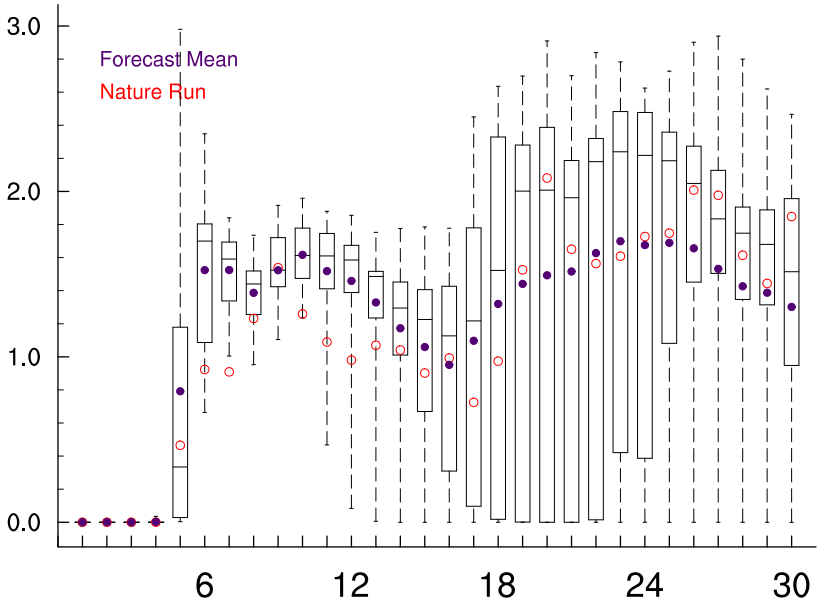


(a) precipitation maxima

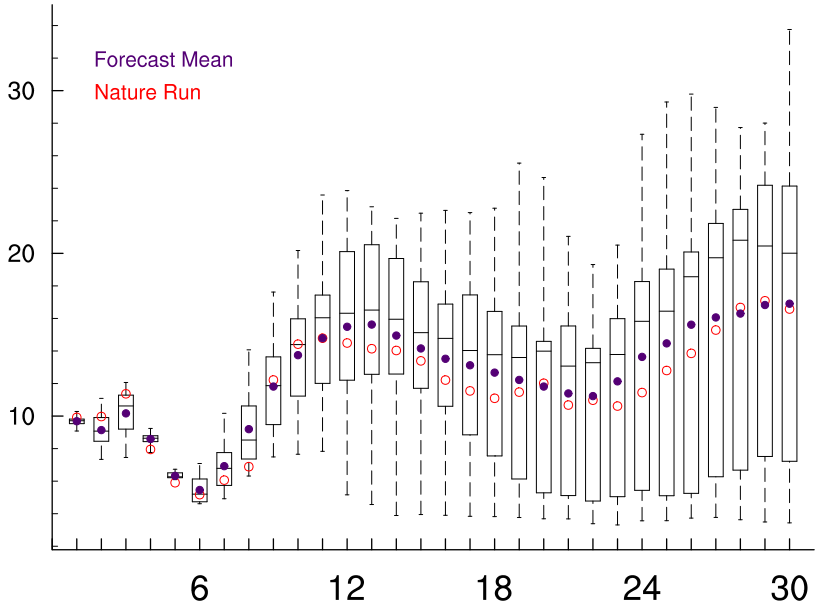


(b) surface wind maxima

Figure 63: Box plot of the precipitating hydrometeors in the lowest level in $\mathrm{g\,kg^{-1}}$ (a) and the surface wind speed maxima in $\mathrm{m\,s^{-1}}$ (b) as a function of time in steps of 10 minutes for the ensemble ens005.

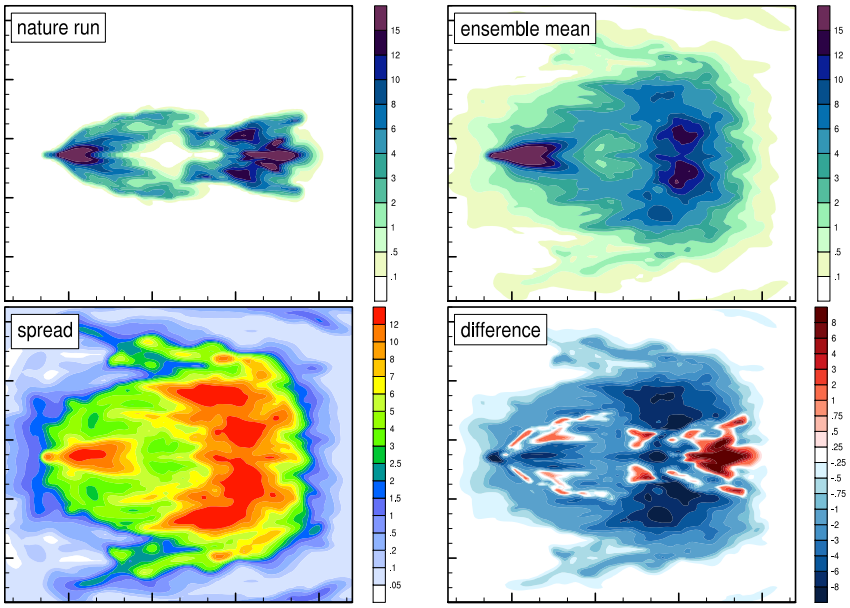


Figure 64: Ensemble ens006. The accumulated surface precipitation in units of $\mathrm{kg\,m^{-2}}$ is plotted in the top left panel for the nature run and in the top right panel for the ensemble mean. The bottom panels exhibit the standard deviation on the left and the differences between the nature run and the ensemble mean on the right (red (blue) colors for larger nature run (ensemble mean) values).

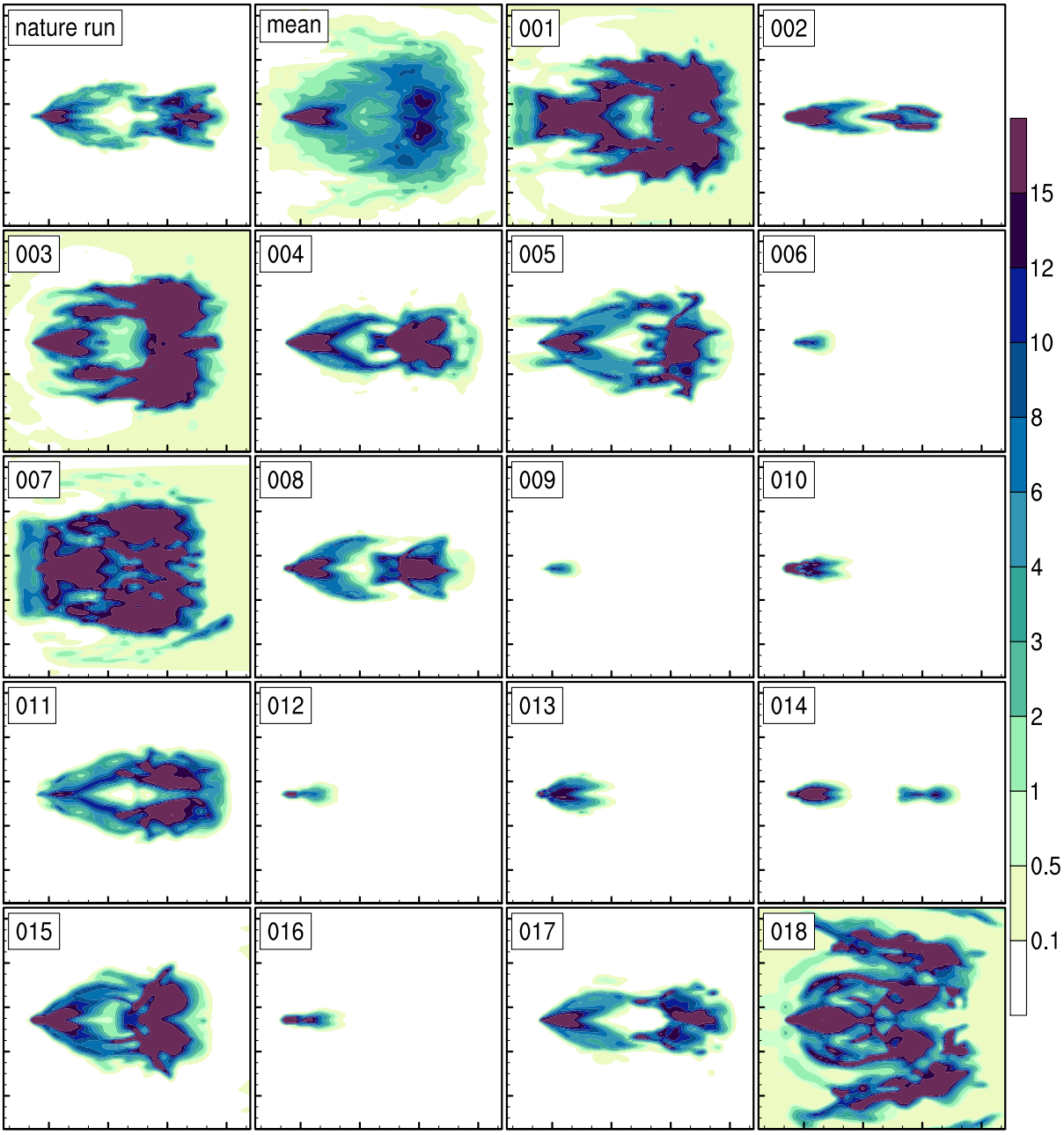


Figure 65: Ensemble ens006. The panels show the accumulated surface precipitation after 5 hours of simulation in units of $\mathrm{kg\,m^{-2}}$ in an area of $75\,\mathrm{km} - 325\,\mathrm{km}$ in x-direction and $50\,\mathrm{km} - 250\,\mathrm{km}$ in y-direction for the nature run, the ensemble mean, and the 18 ensemble members.

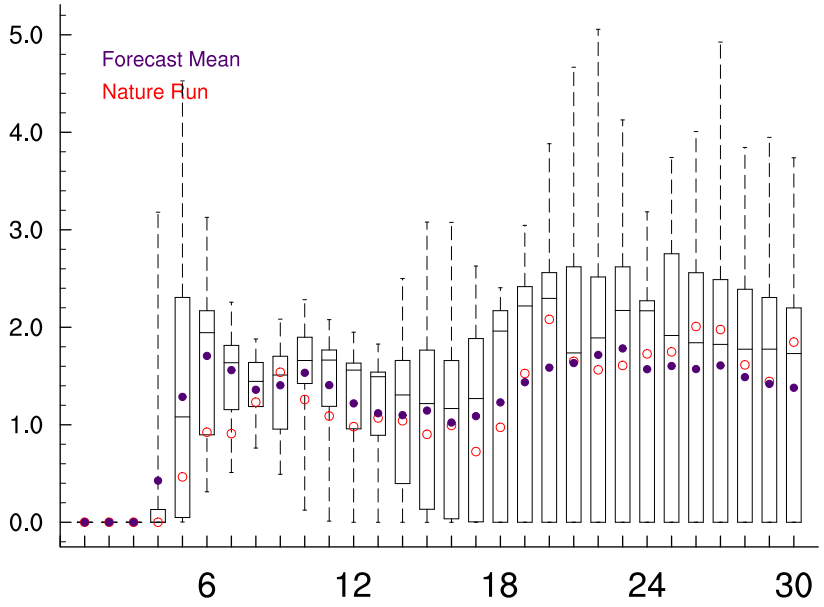


(a) precipitation maxima

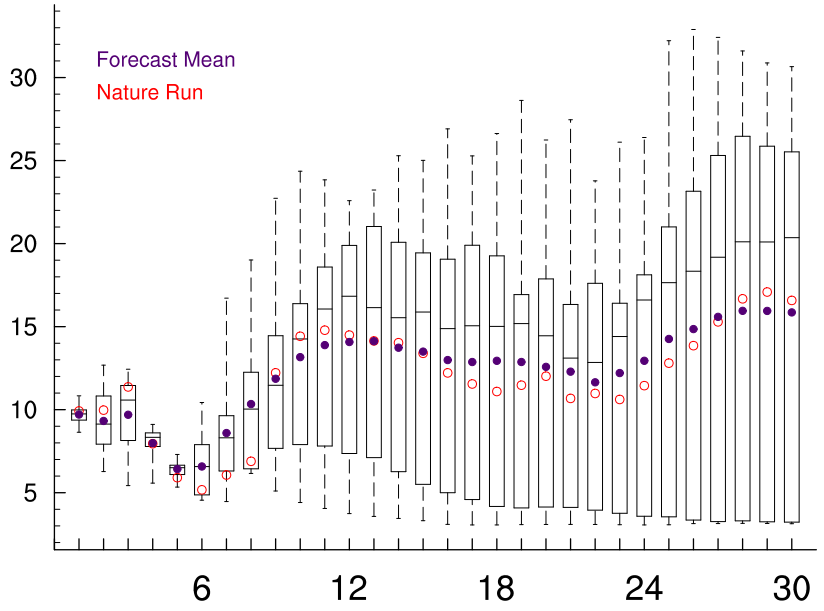


(b) surface wind maxima

Figure 66: Box plot of the precipitating hydrometeors in the lowest level in $\mathrm{g\,kg^{-1}}$ (a) and the surface wind speed maxima in $\mathrm{m\,s^{-1}}$ (b) as a function of time in steps of 10 minutes for the ensemble ens006.

## Temperature Perturbation with Constant Specific Humidity

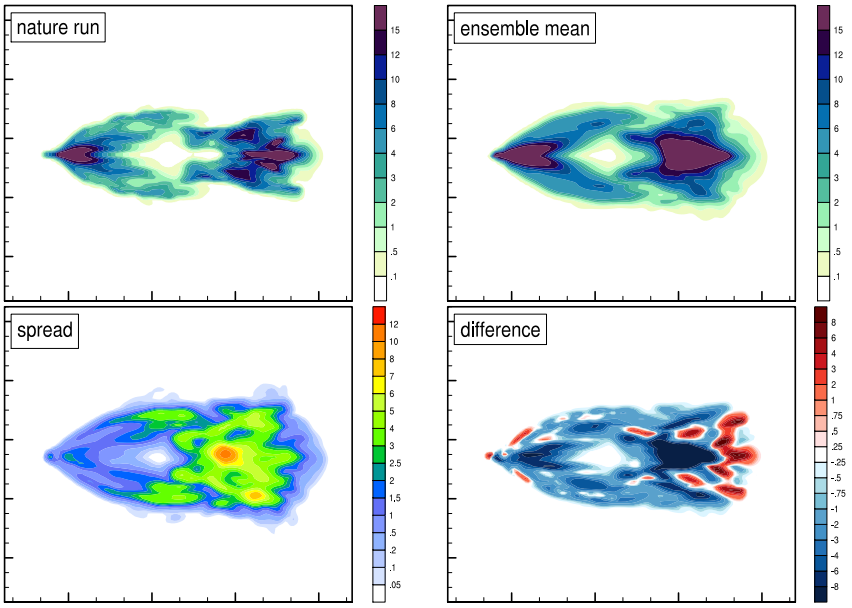


Figure 67: Ensemble ens007. The accumulated surface precipitation in units of $\mathrm{kg\,m^{-2}}$ is plotted in the top left panel for the nature run and in the top right panel for the ensemble mean. The bottom panels exhibit the standard deviation on the left and the differences between the nature run and the ensemble mean on the right (red (blue) colors for larger nature run (ensemble mean) values).

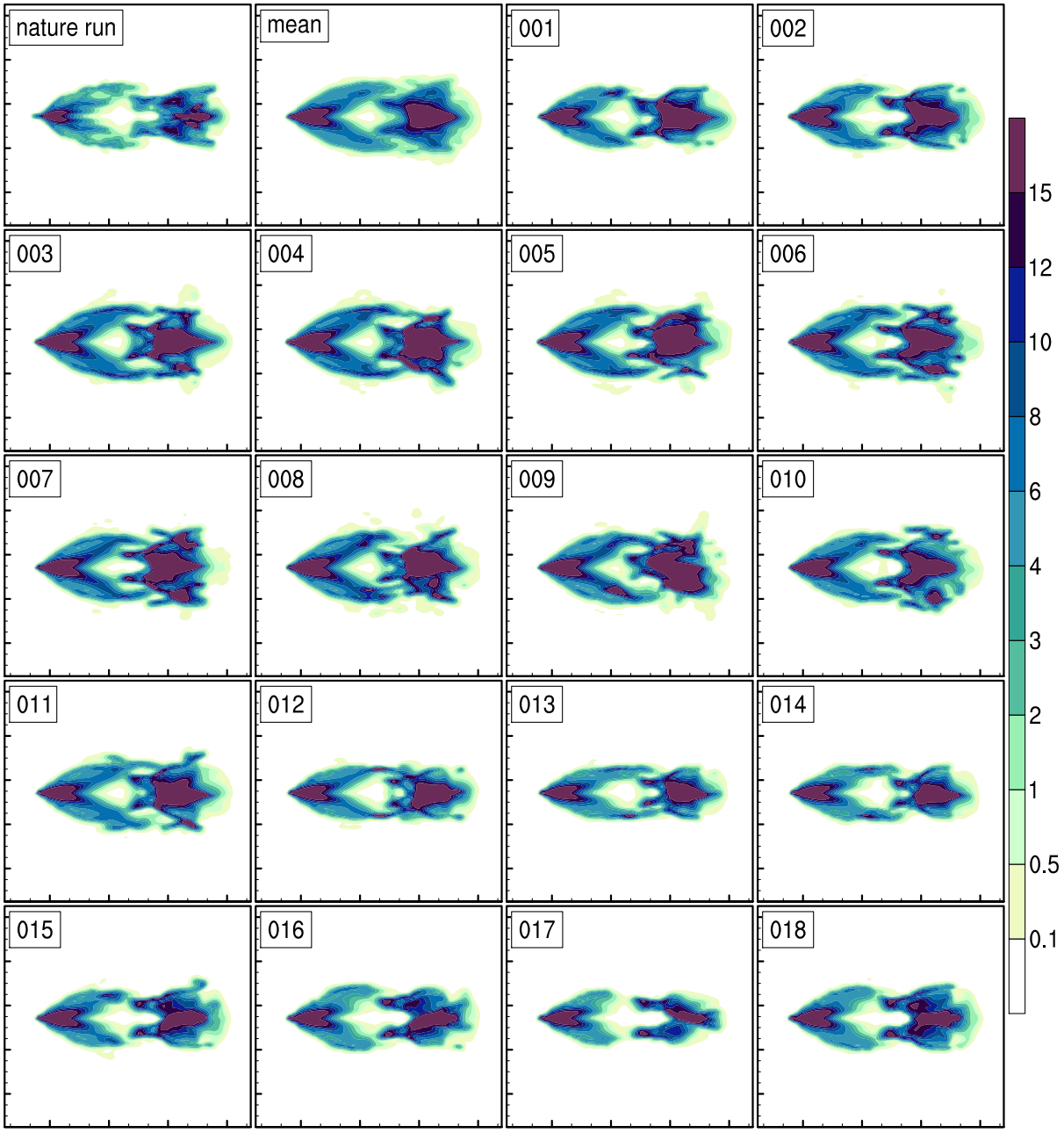


Figure 68: Ensemble ens007. The panels show the accumulated surface precipitation after 5 hours of simulation in units of $\mathrm{kg\,m^{-2}}$ in an area of $75\,\mathrm{km} - 325\,\mathrm{km}$ in x-direction and $50\,\mathrm{km} - 250\,\mathrm{km}$ in y-direction for the nature run, the ensemble mean, and the 18 ensemble members.

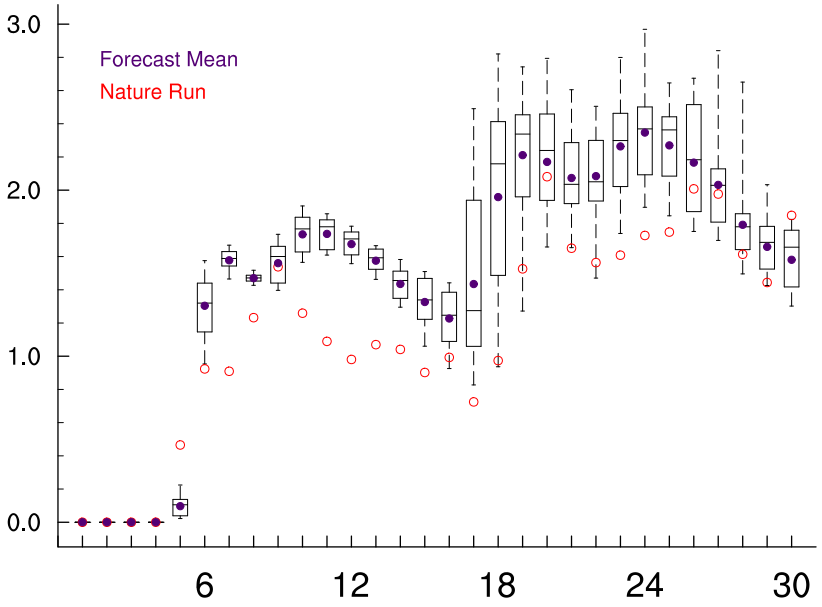


(a) precipitation maxima

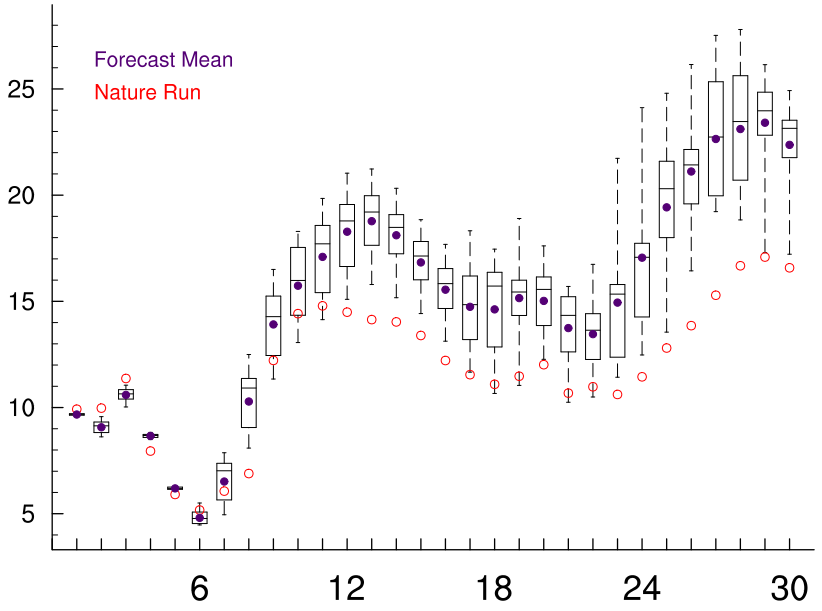


(b) surface wind maxima

Figure 69: Box plot of the precipitating hydrometeors in the lowest level in $\mathrm{g\,kg^{-1}}$ (a) and the surface wind speed maxima in $\mathrm{m\,s^{-1}}$ (b) as a function of time in steps of 10 minutes for the ensemble ens007.

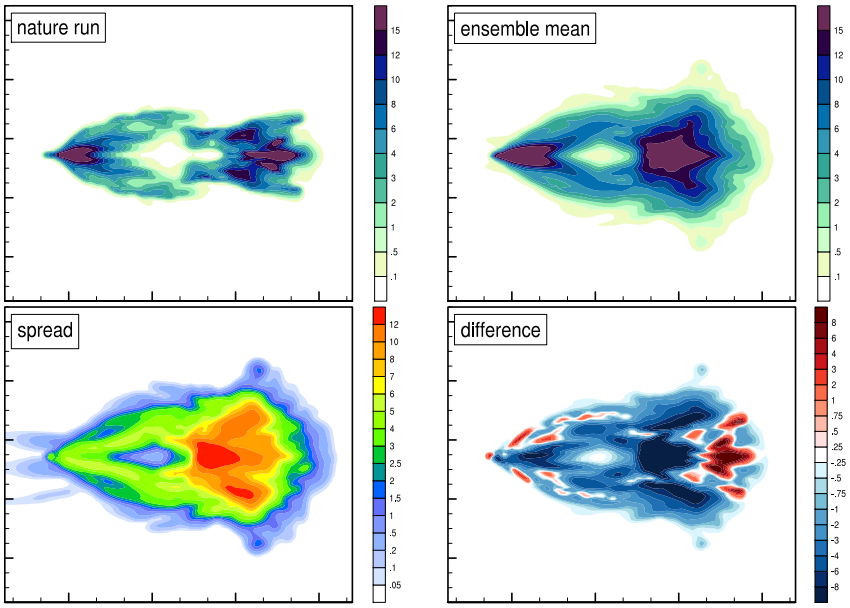


Figure 70: Ensemble ens008. The accumulated surface precipitation in units of $\mathrm{kg\,m^{-2}}$ is plotted in the top left panel for the nature run and in the top right panel for the ensemble mean. The bottom panels exhibit the standard deviation on the left and the differences between the nature run and the ensemble mean on the right (red (blue) colors for larger nature run (ensemble mean) values).

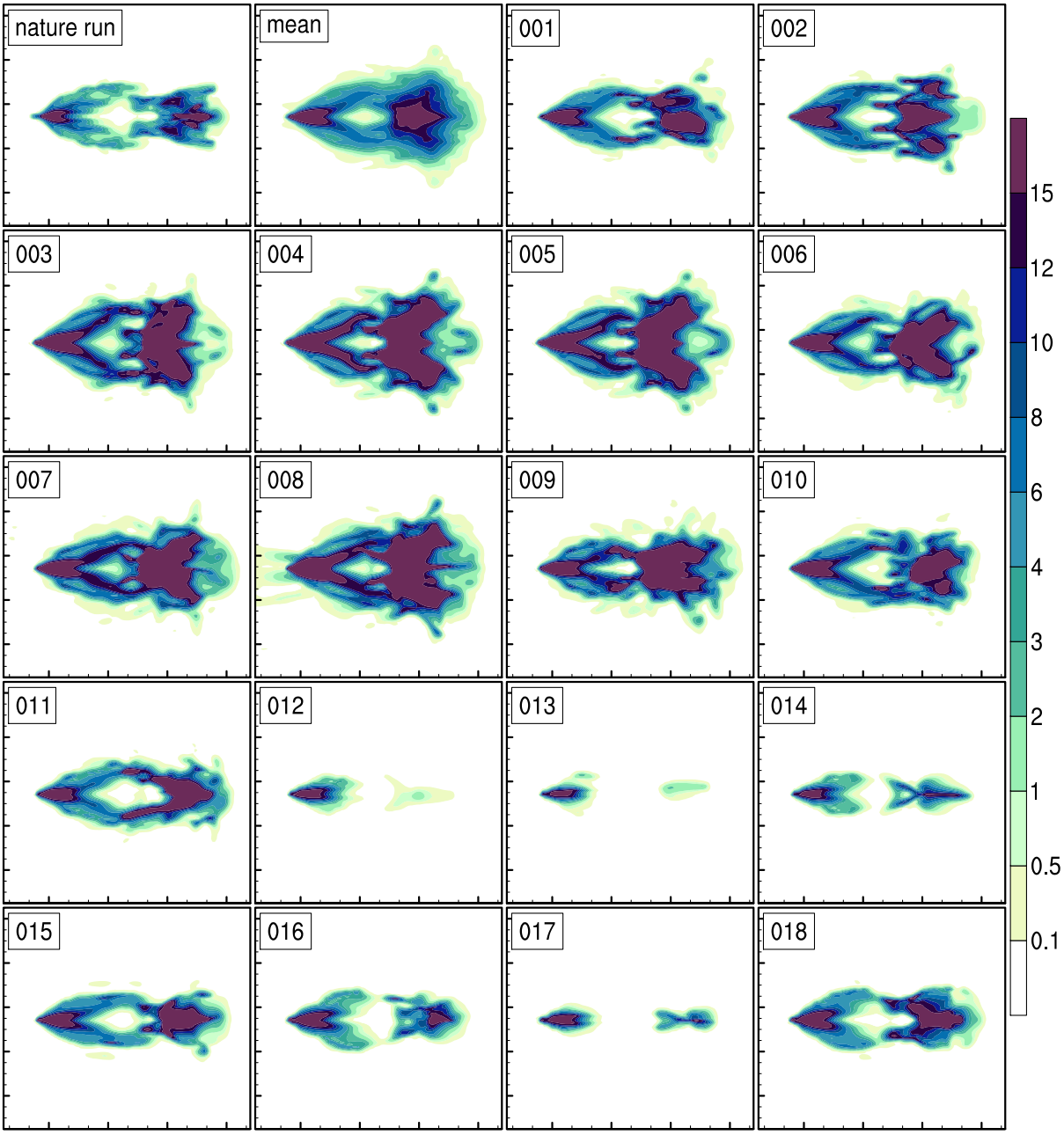


Figure 71: Ensemble ens008. The panels show the accumulated surface precipitation after 5 hours of simulation in units of $\mathrm{kg\,m^{-2}}$ in an area of $75\,\mathrm{km} - 325\,\mathrm{km}$ in x-direction and $50\,\mathrm{km} - 250\,\mathrm{km}$ in y-direction for the nature run, the ensemble mean, and the 18 ensemble members.

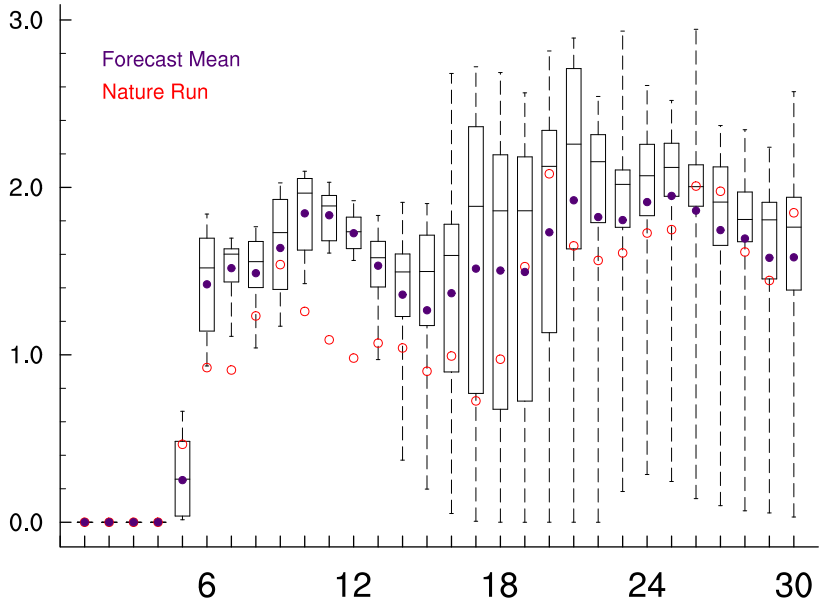


(a) precipitation maxima

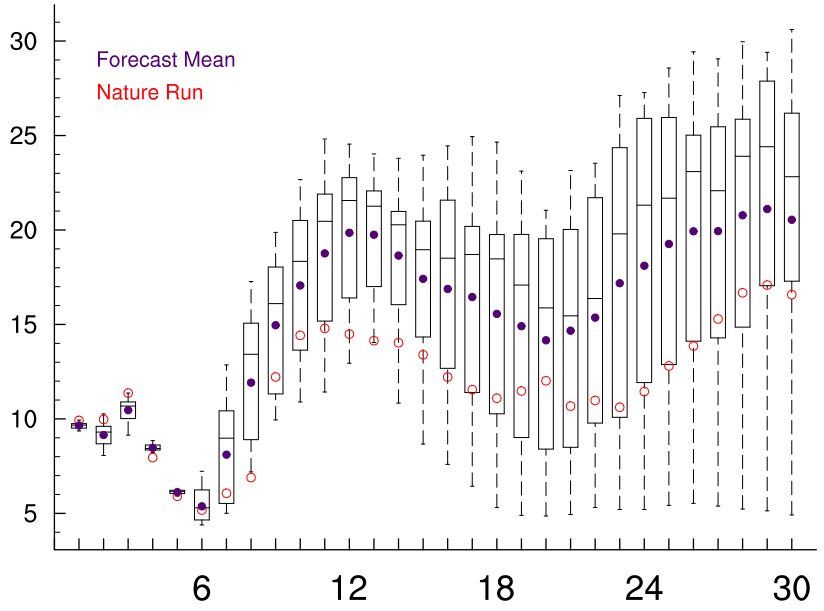


(b) surface wind maxima

Figure 72: Box plot of the precipitating hydrometeors in the lowest level in $\mathrm{g\,kg^{-1}}$ (a) and the surface wind speed maxima in $\mathrm{m\,s^{-1}}$ (b) as a function of time in steps of 10 minutes for the ensemble ens008.

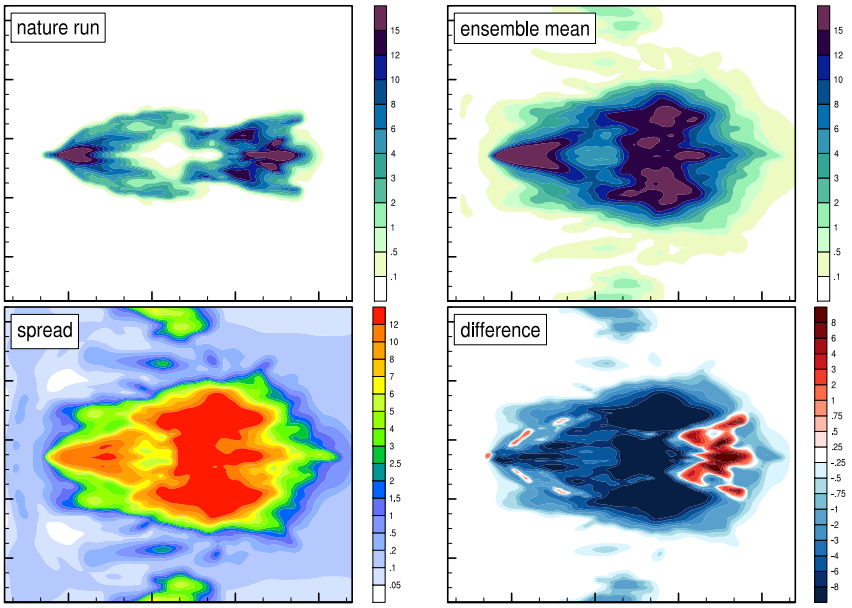


Figure 73: Ensemble ens009. The accumulated surface precipitation in units of $\mathrm{kg\,m^{-2}}$ is plotted in the top left panel for the nature run and in the top right panel for the ensemble mean. The bottom panels exhibit the standard deviation on the left and the differences between the nature run and the ensemble mean on the right (red (blue) colors for larger nature run (ensemble mean) values).

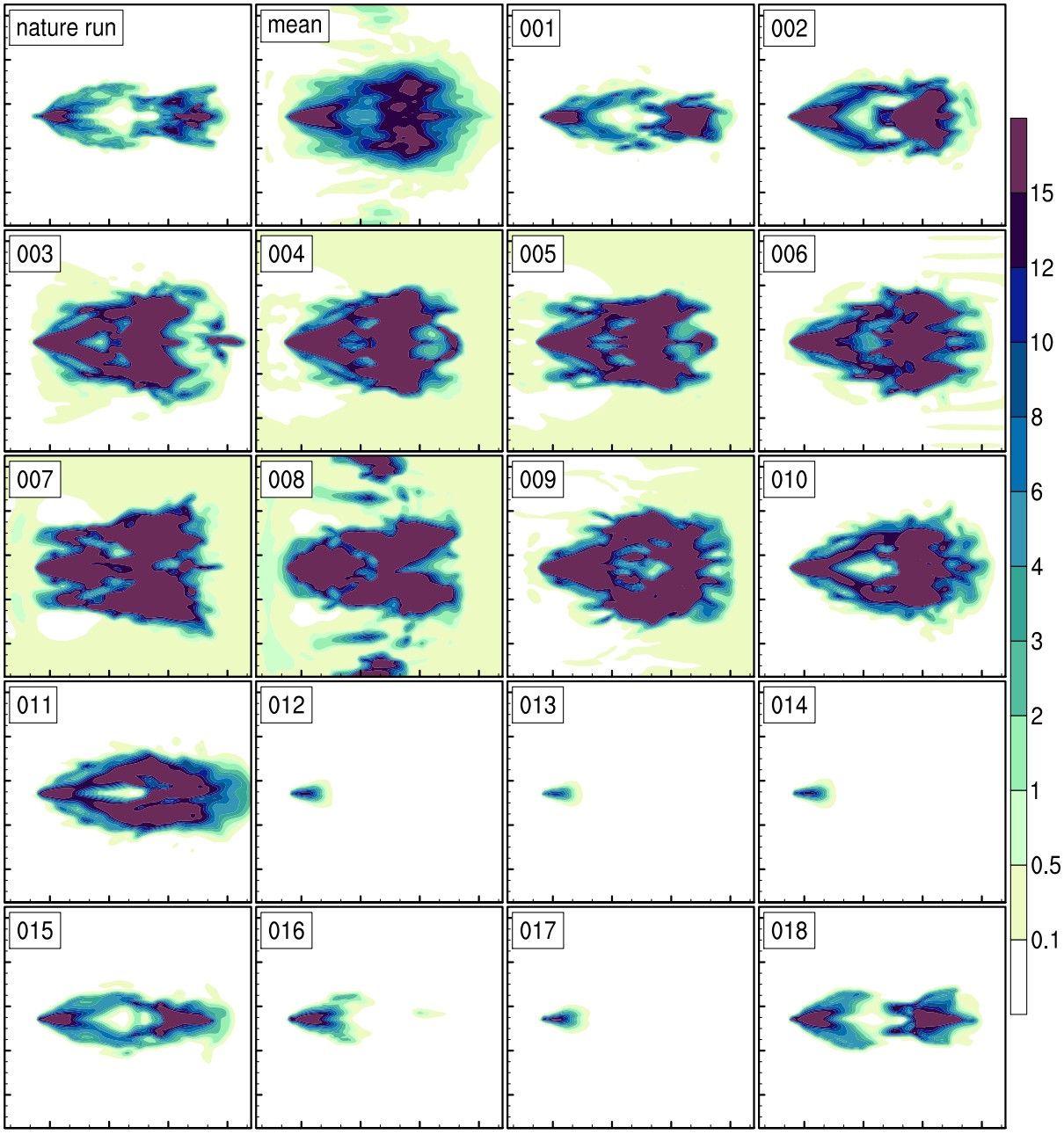


Figure 74: Ensemble ens009. The panels show the accumulated surface precipitation after 5 hours of simulation in units of $\mathrm{kg\,m^{-2}}$ in an area of $75\,\mathrm{km} - 325\,\mathrm{km}$ in x-direction and $50\,\mathrm{km} - 250\,\mathrm{km}$ in y-direction for the nature run, the ensemble mean, and the 18 ensemble members.

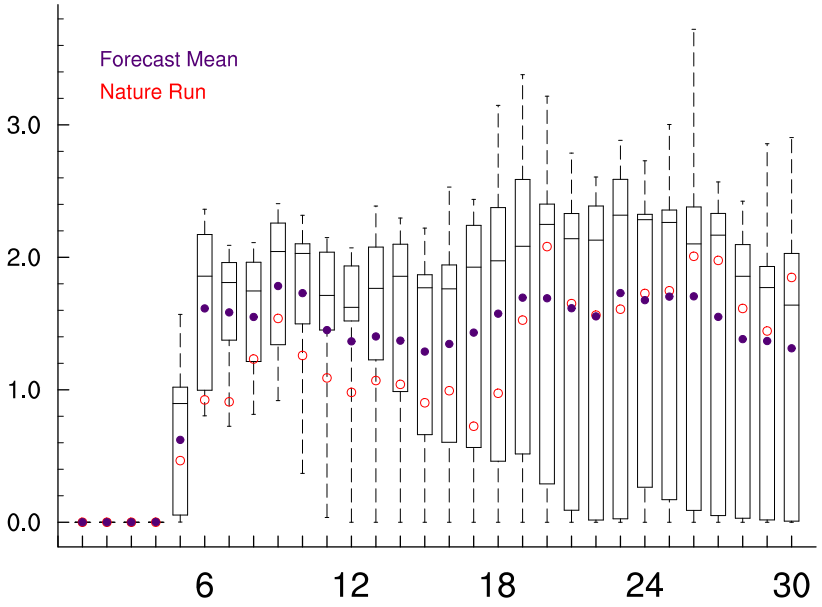


(a) precipitation maxima

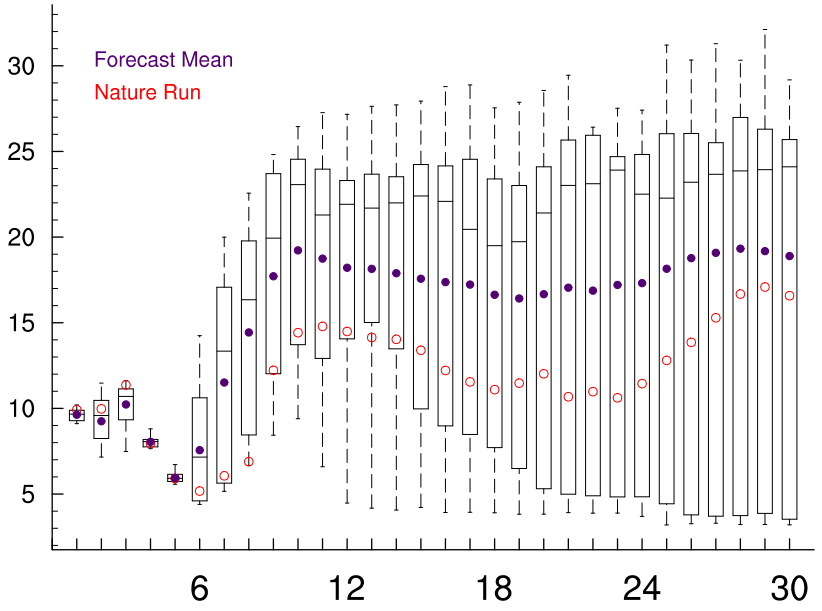


(b) surface wind maxima

Figure 75: Box plot of the precipitating hydrometeors in the lowest level in $\mathrm{g\,kg^{-1}}$ (a) and the surface wind speed maxima in $\mathrm{m\,s^{-1}}$ (b) as a function of time in steps of 10 minutes for the ensemble ens009.

## Relative Humidity Perturbation with Constant Temperature

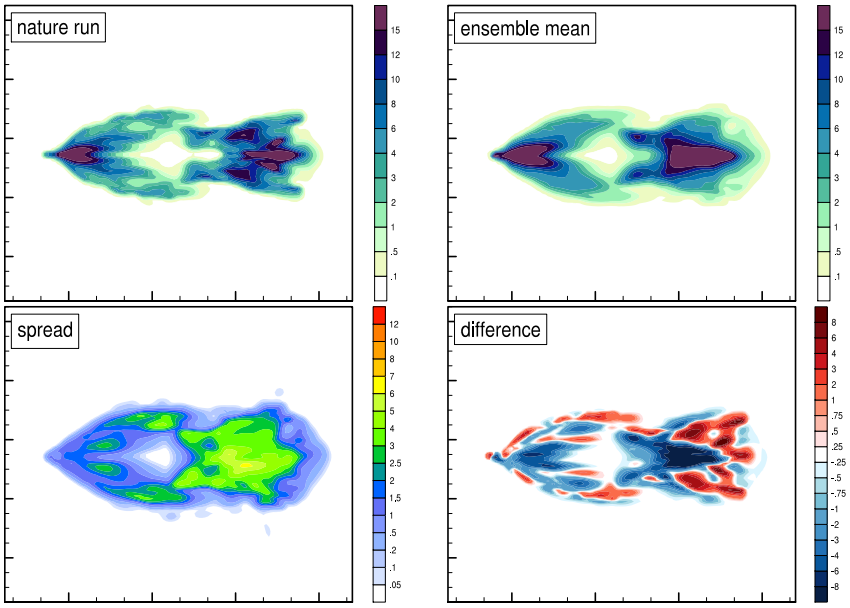


Figure 76: Ensemble ens010. The accumulated surface precipitation in units of $\mathrm{kg\,m^{-2}}$ is plotted in the top left panel for the nature run and in the top right panel for the ensemble mean. The bottom panels exhibit the standard deviation on the left and the differences between the nature run and the ensemble mean on the right (red (blue) colors for larger nature run (ensemble mean) values).

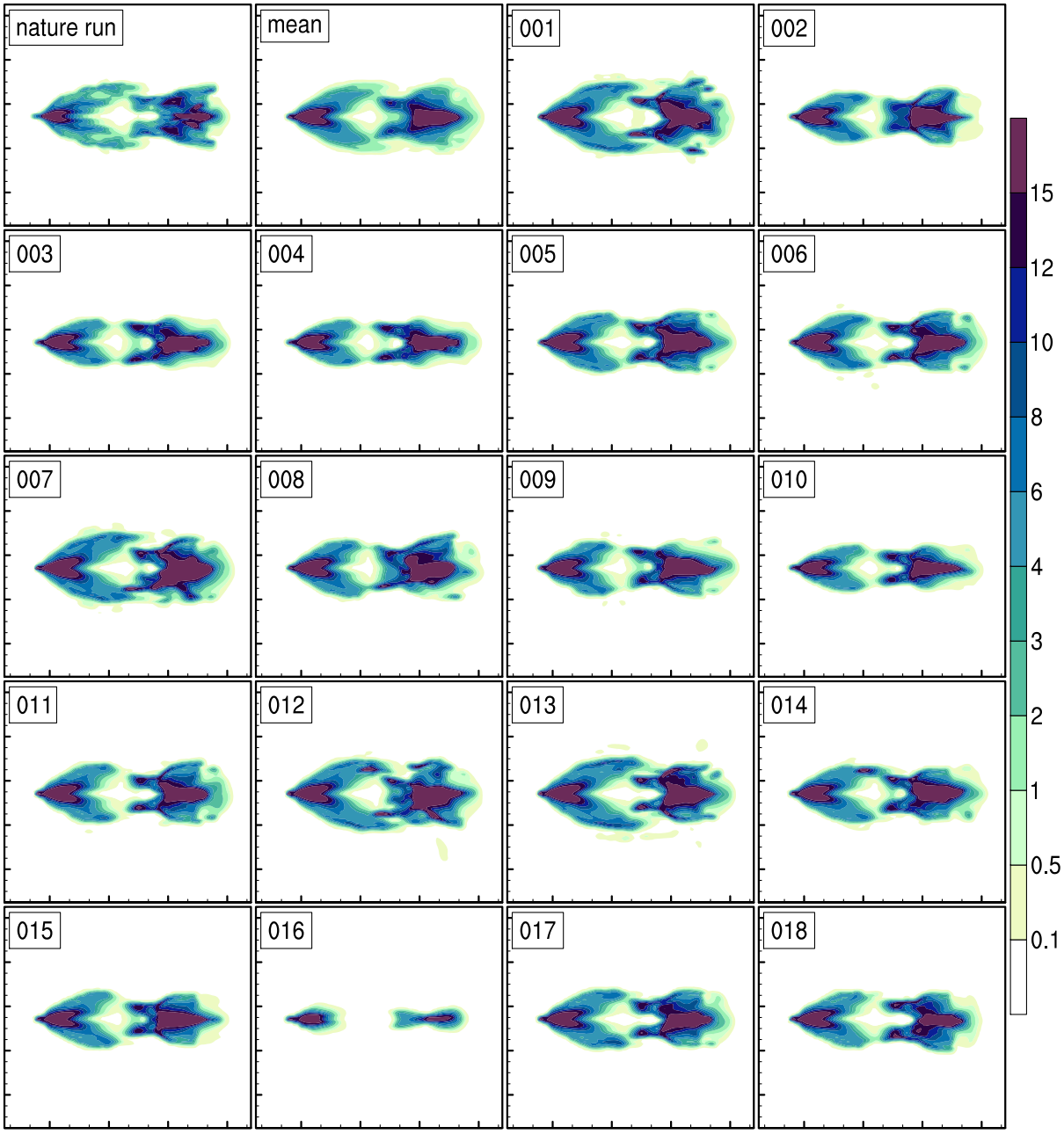


Figure 77: Ensemble ens010. The panels show the accumulated surface precipitation after 5 hours of simulation in units of $\mathrm{kg\,m^{-2}}$ in an area of $75\,\mathrm{km} - 325\,\mathrm{km}$ in x-direction and $50\,\mathrm{km} - 250\,\mathrm{km}$ in y-direction for the nature run, the ensemble mean, and the 18 ensemble members.

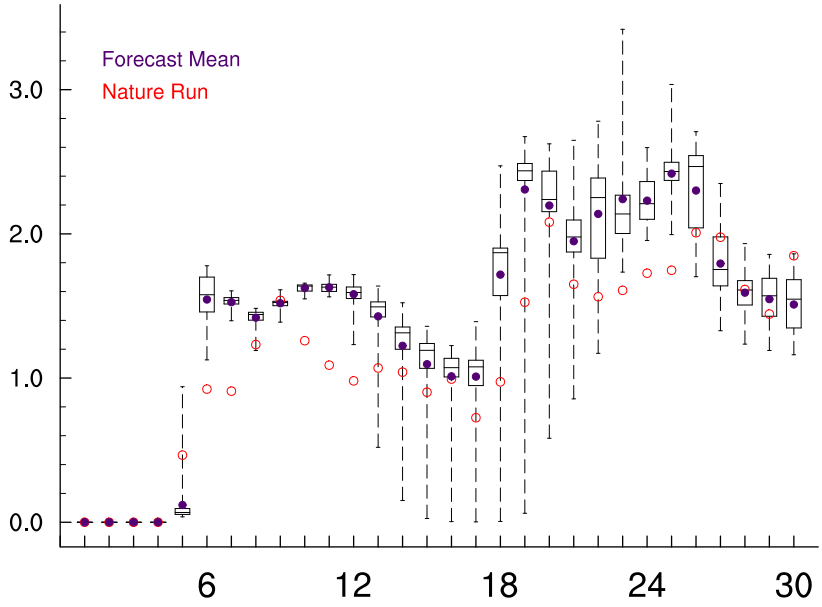


(a) precipitation maxima

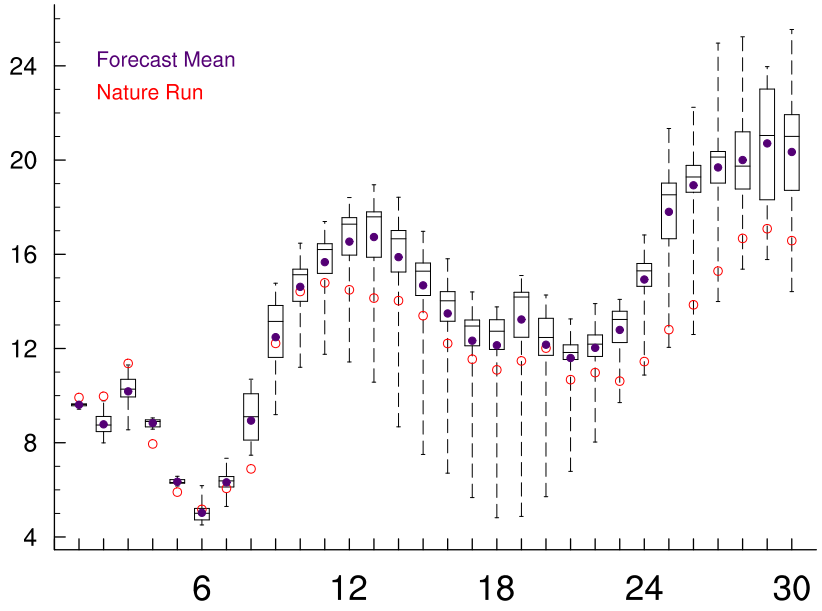


(b) surface wind maxima

Figure 78: Box plot of the precipitating hydrometeors in the lowest level in $\mathrm{g\,kg^{-1}}$ (a) and the surface wind speed maxima in $\mathrm{m\,s^{-1}}$ (b) as a function of time in steps of 10 minutes for the ensemble ens010.

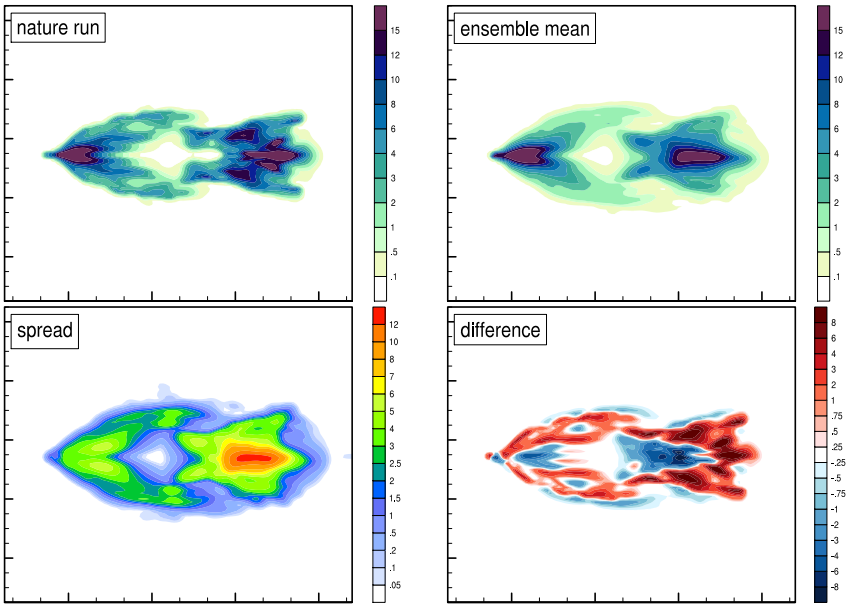


Figure 79: Ensemble ens011. The accumulated surface precipitation in units of $\mathrm{kg\,m^{-2}}$ is plotted in the top left panel for the nature run and in the top right panel for the ensemble mean. The bottom panels exhibit the standard deviation on the left and the differences between the nature run and the ensemble mean on the right (red (blue) colors for larger nature run (ensemble mean) values).

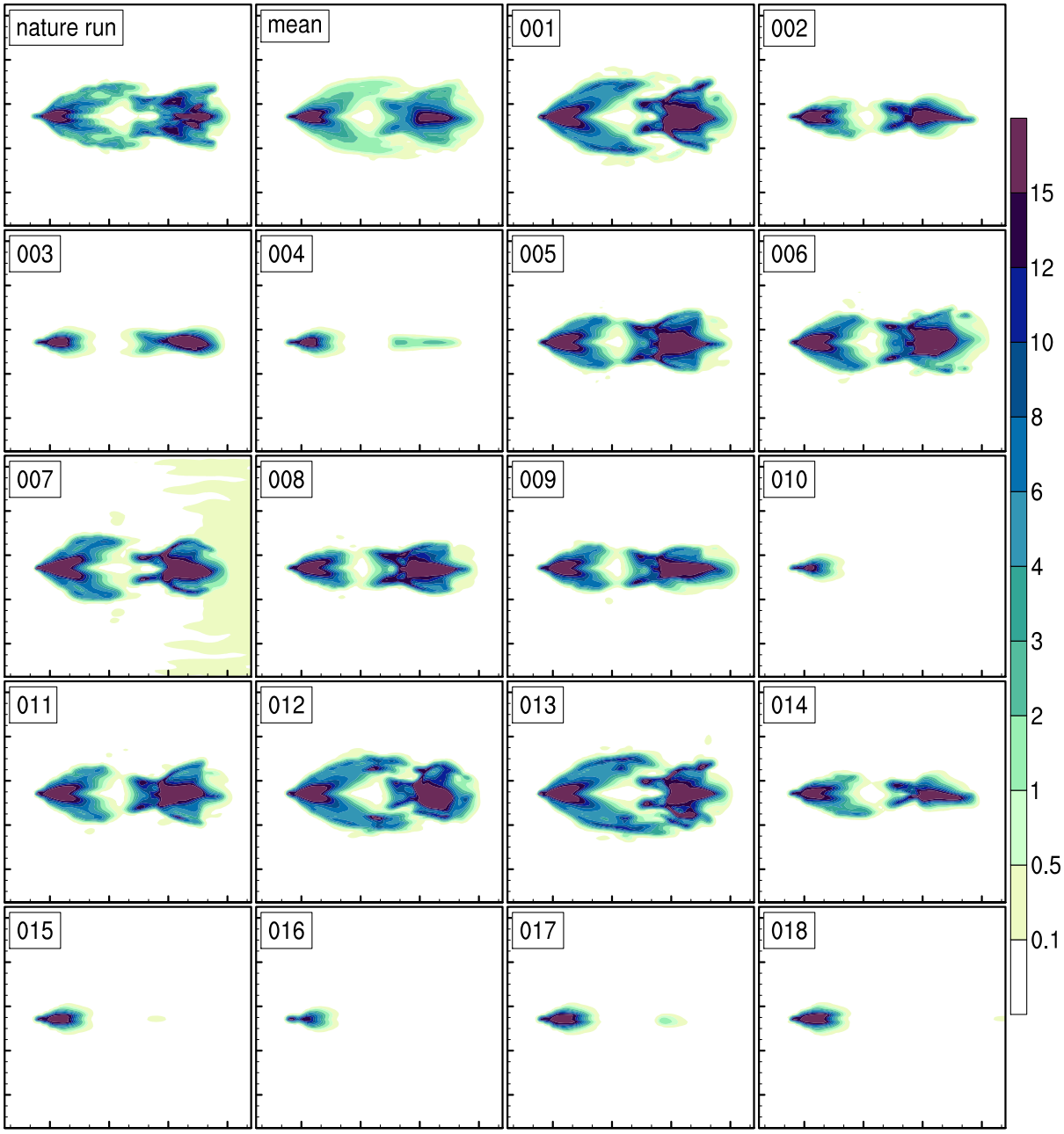


Figure 80: Ensemble ens011. The panels show the accumulated surface precipitation after 5 hours of simulation in units of $\mathrm{kg\,m^{-2}}$ in an area of $75\,\mathrm{km} - 325\,\mathrm{km}$ in x-direction and $50\,\mathrm{km} - 250\,\mathrm{km}$ in y-direction for the nature run, the ensemble mean, and the 18 ensemble members.

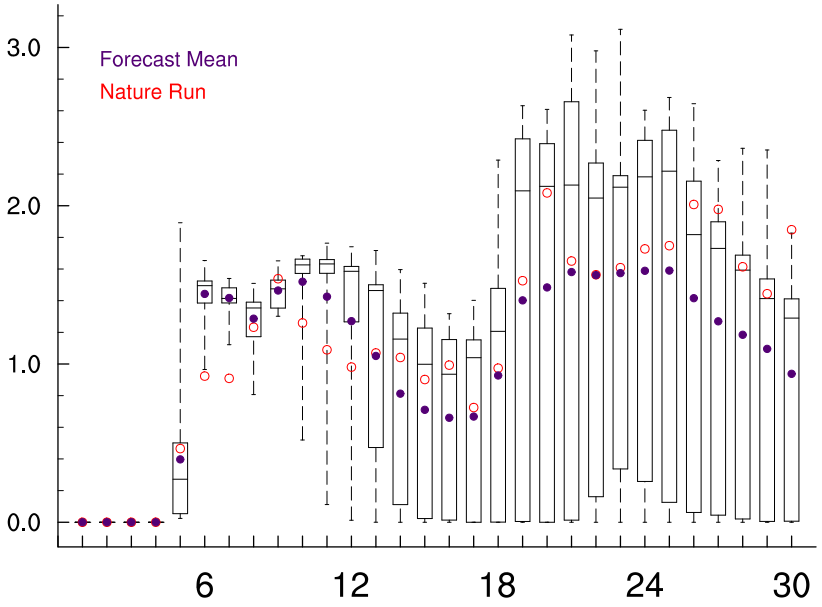


(a) precipitation maxima

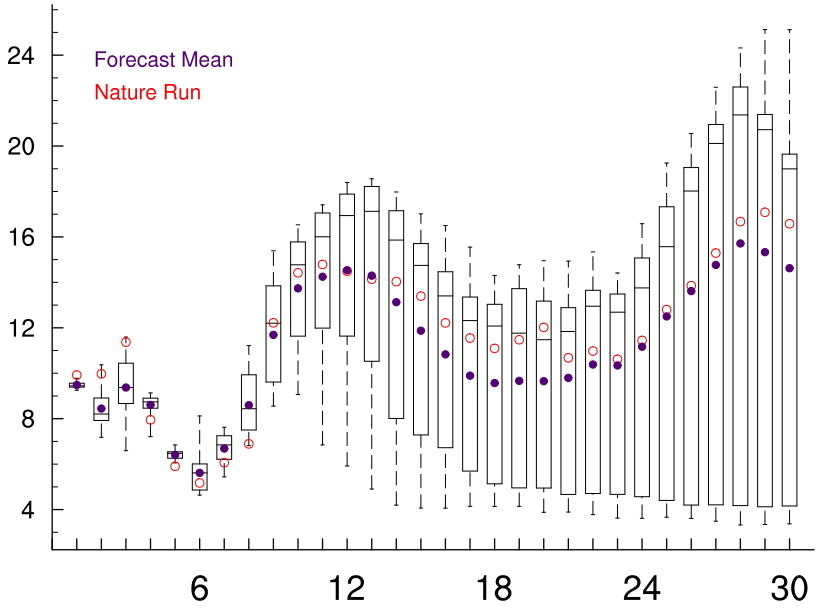


(b) surface wind maxima

Figure 81: Box plot of the precipitating hydrometeors in the lowest level in $\mathrm{g\,kg^{-1}}$ (a) and the surface wind speed maxima in $\mathrm{m\,s^{-1}}$ (b) as a function of time in steps of 10 minutes for the ensemble ens011.

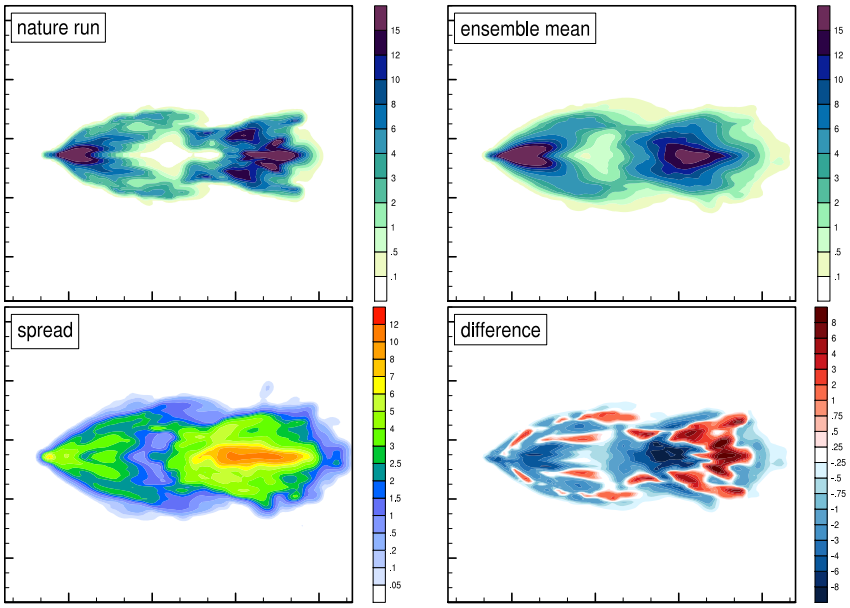


Figure 82: Ensemble ens012. The accumulated surface precipitation in units of $\mathrm{kg\,m^{-2}}$ is plotted in the top left panel for the nature run and in the top right panel for the ensemble mean. The bottom panels exhibit the standard deviation on the left and the differences between the nature run and the ensemble mean on the right (red (blue) colors for larger nature run (ensemble mean) values).

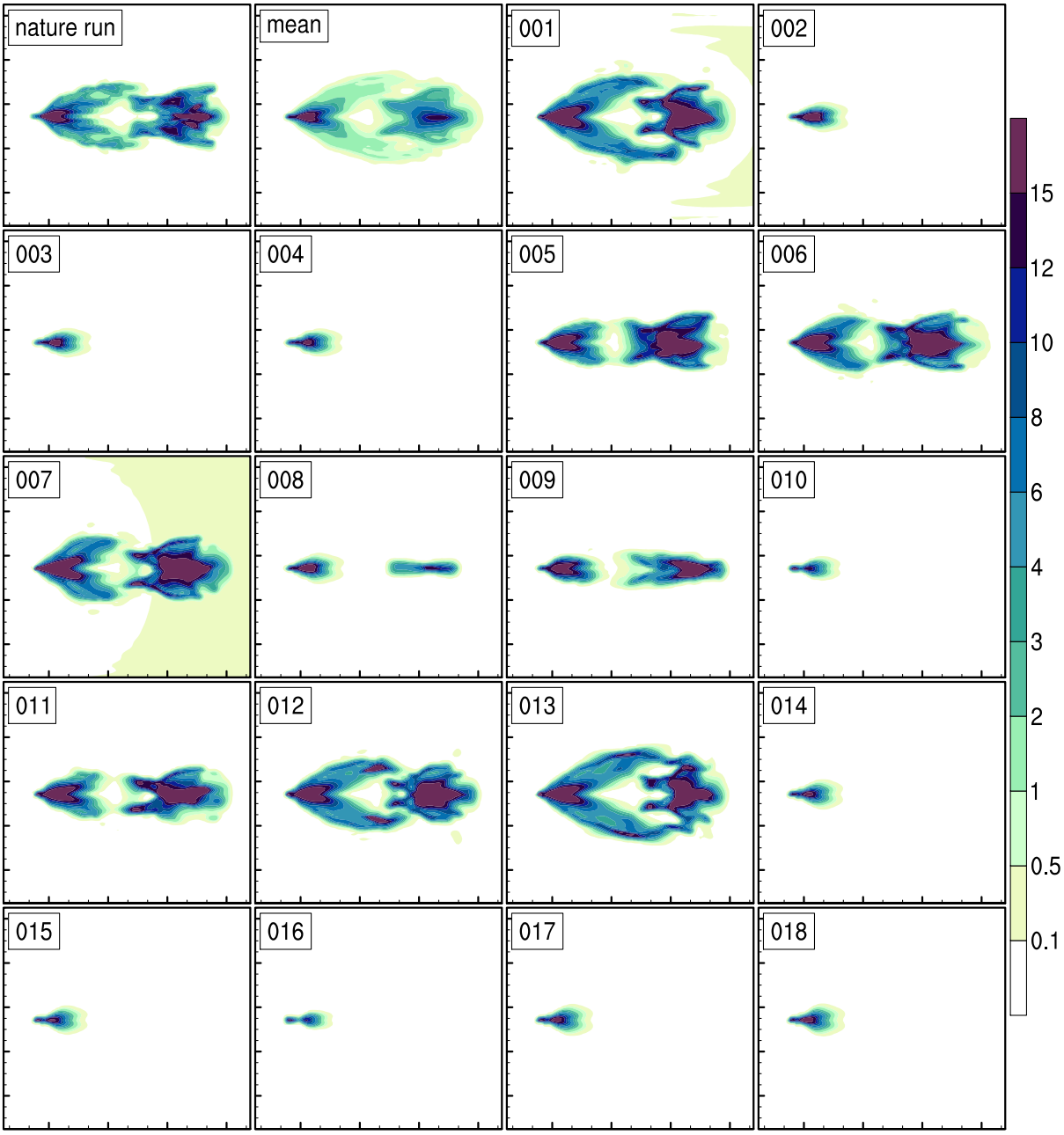


Figure 83: Ensemble ens012. The panels show the accumulated surface precipitation after 5 hours of simulation in units of $\mathrm{kg\,m^{-2}}$ in an area of $75\,\mathrm{km} - 325\,\mathrm{km}$ in x-direction and $50\,\mathrm{km} - 250\,\mathrm{km}$ in y-direction for the nature run, the ensemble mean, and the 18 ensemble members.

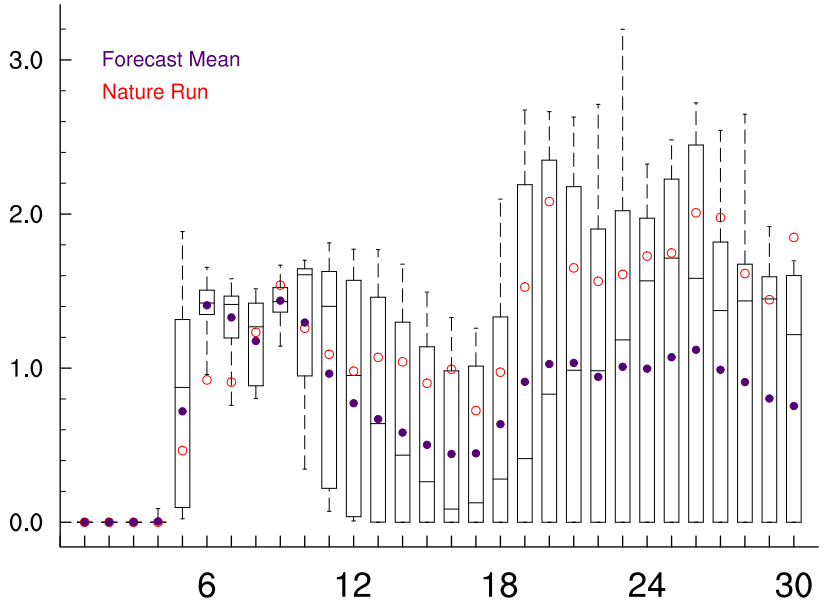


(a) precipitation maxima

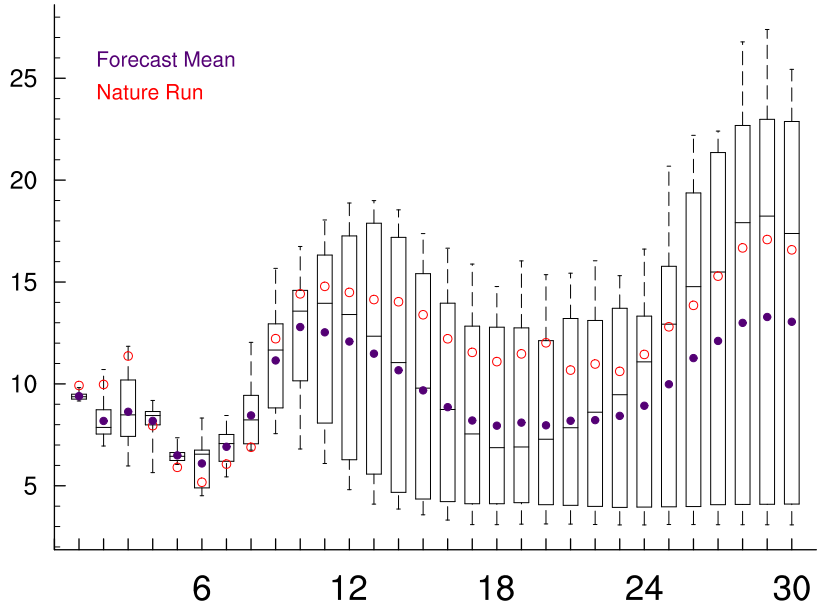


(b) surface wind maxima

Figure 84: Box plot of the precipitating hydrometeors in the lowest level in $\mathrm{g\,kg^{-1}}$ (a) and the surface wind speed maxima in $\mathrm{m\,s^{-1}}$ (b) as a function of time in steps of 10 minutes for the ensemble ens012.

## Temperature and Wind Speed Perturbation

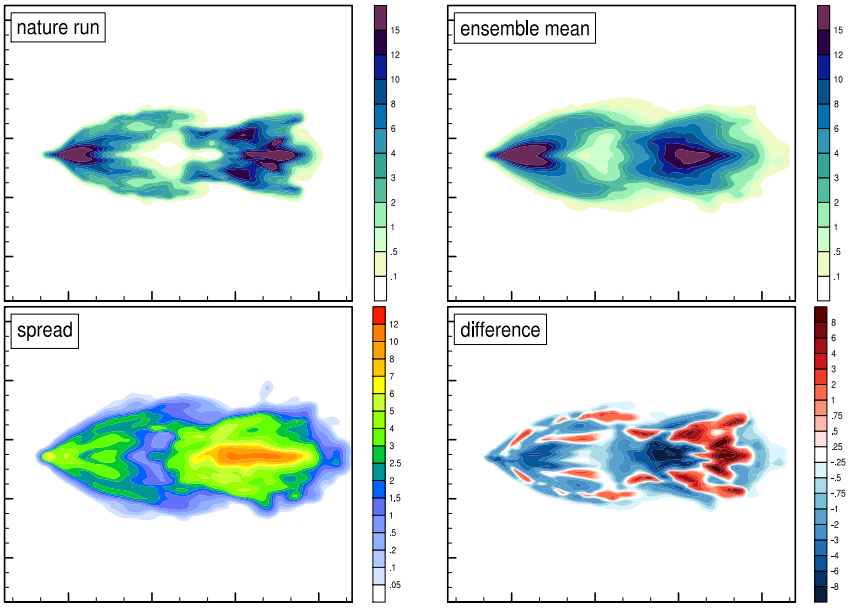


Figure 85: Ensemble ens013. The accumulated surface precipitation in units of $\mathrm{kg\,m^{-2}}$ is plotted in the top left panel for the nature run and in the top right panel for the ensemble mean. The bottom panels exhibit the standard deviation on the left and the differences between the nature run and the ensemble mean on the right (red (blue) colors for larger nature run (ensemble mean) values).

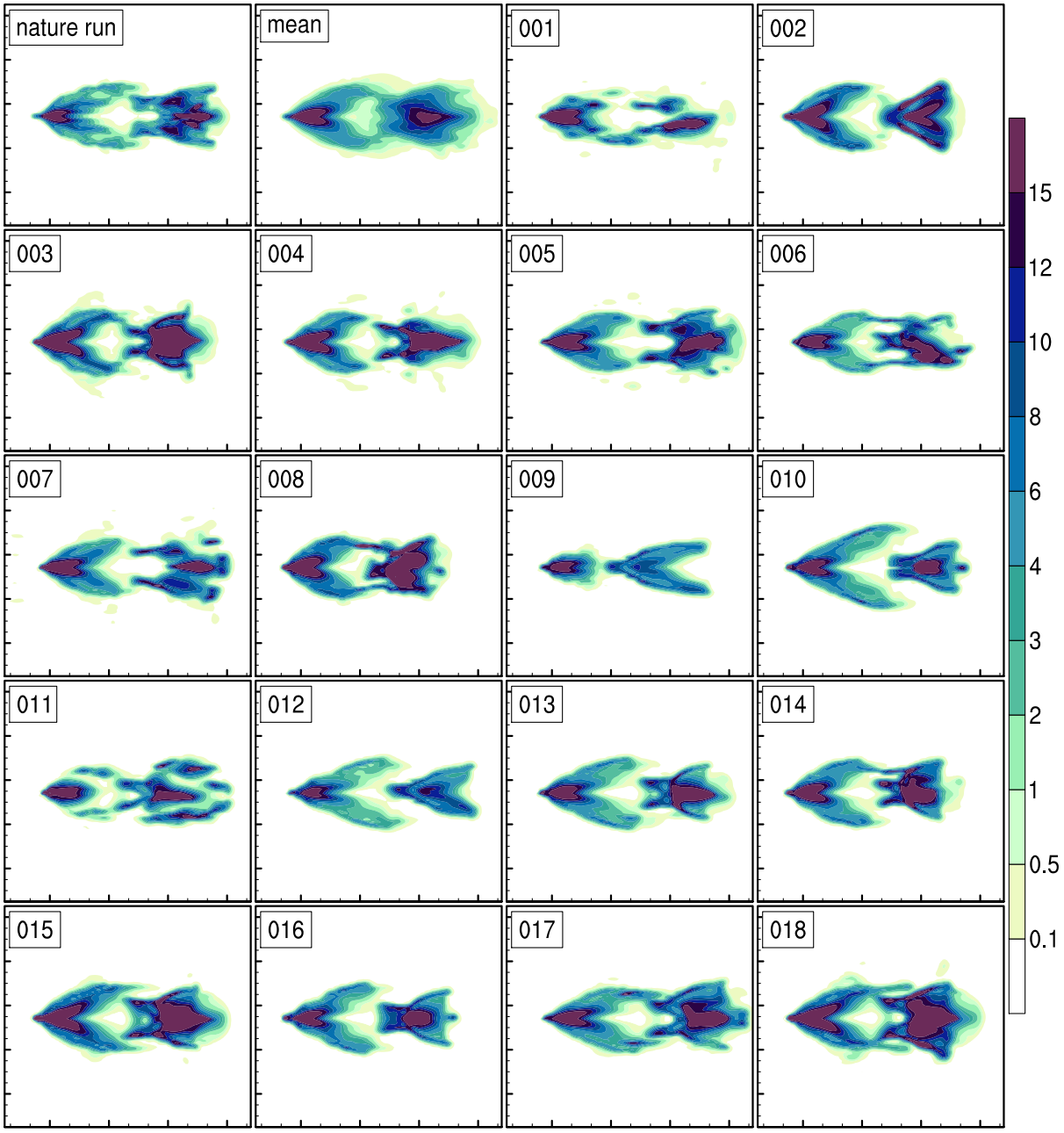


Figure 86: Ensemble ens013. The panels show the accumulated surface precipitation after 5 hours of simulation in units of $\mathrm{kg\,m^{-2}}$ in an area of $75\,\mathrm{km} - 325\,\mathrm{km}$ in x-direction and $50\,\mathrm{km} - 250\,\mathrm{km}$ in y-direction for the nature run, the ensemble mean, and the 18 ensemble members.

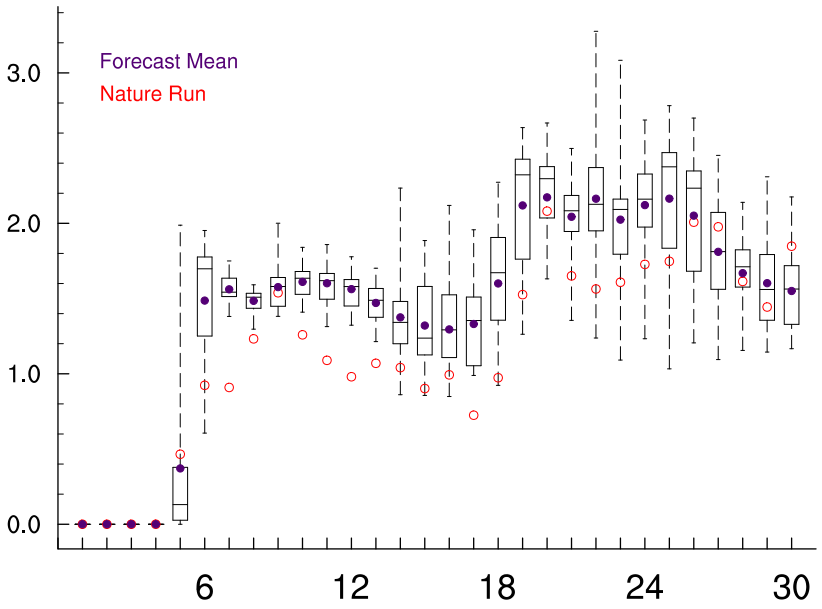


(a) precipitation maxima

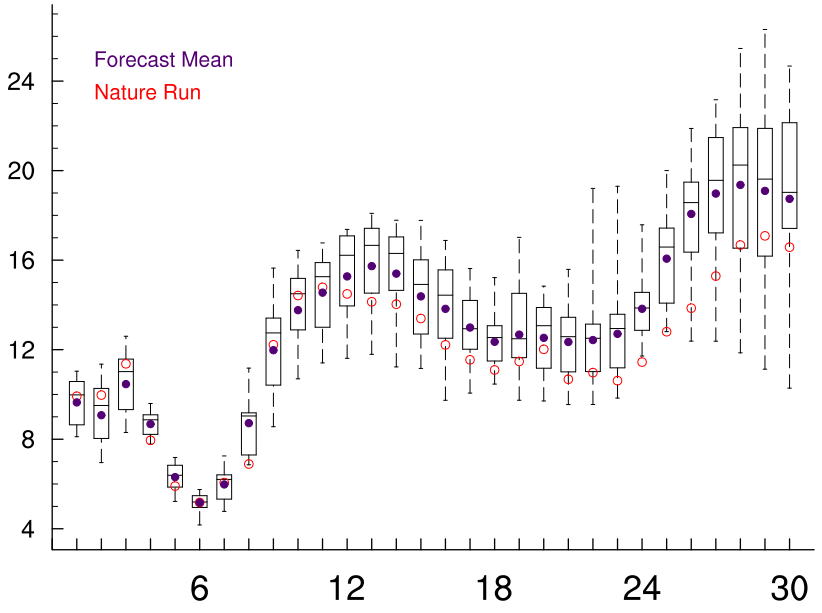


(b) surface wind maxima

Figure 87: Box plot of the precipitating hydrometeors in the lowest level in $\mathrm{g\,kg^{-1}}$ (a) and the surface wind speed maxima in $\mathrm{m\,s^{-1}}$ (b) as a function of time in steps of 10 minutes for the ensemble ens013.

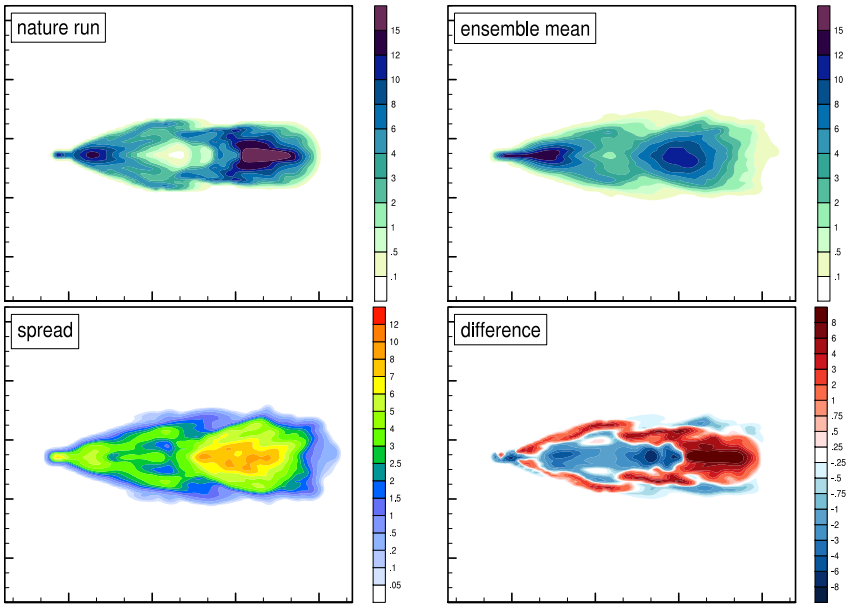


Figure 88: Ensemble ens014. The accumulated surface precipitation in units of $\mathrm{kg\,m^{-2}}$ is plotted in the top left panel for the nature run and in the top right panel for the ensemble mean. The bottom panels exhibit the standard deviation on the left and the differences between the nature run and the ensemble mean on the right (red (blue) colors for larger nature run (ensemble mean) values).

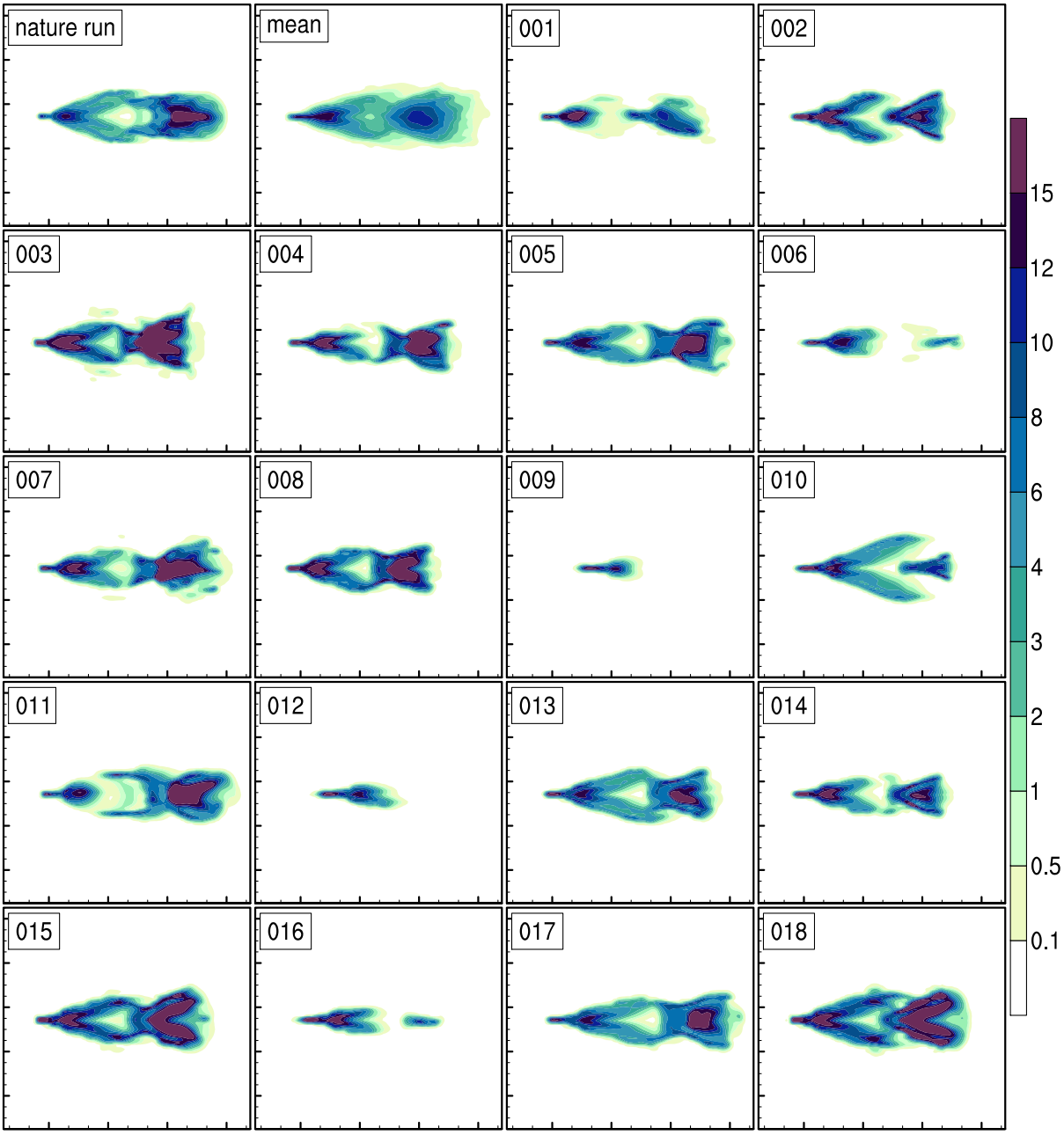


Figure 89: Ensemble ens014. The panels show the accumulated surface precipitation after 5 hours of simulation in units of $\mathrm{kg\,m^{-2}}$ in an area of $75\,\mathrm{km} - 325\,\mathrm{km}$ in x-direction and $50\,\mathrm{km} - 250\,\mathrm{km}$ in y-direction for the nature run, the ensemble mean, and the 18 ensemble members.

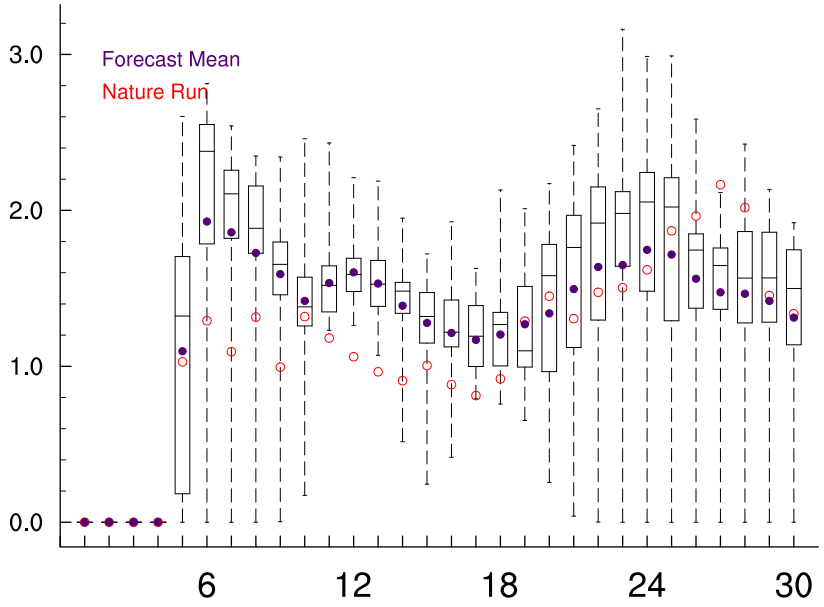


(a) precipitation maxima

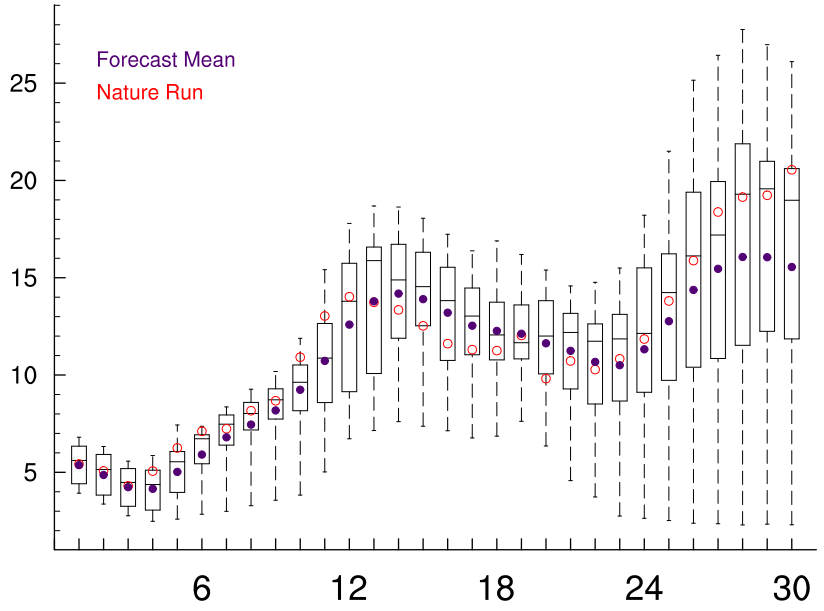


(b) surface wind maxima

Figure 90: Box plot of the precipitating hydrometeors in the lowest level in $\mathrm{g\,kg^{-1}}$ (a) and the surface wind speed maxima in $\mathrm{m\,s^{-1}}$ (b) as a function of time in steps of 10 minutes for the ensemble ens014.

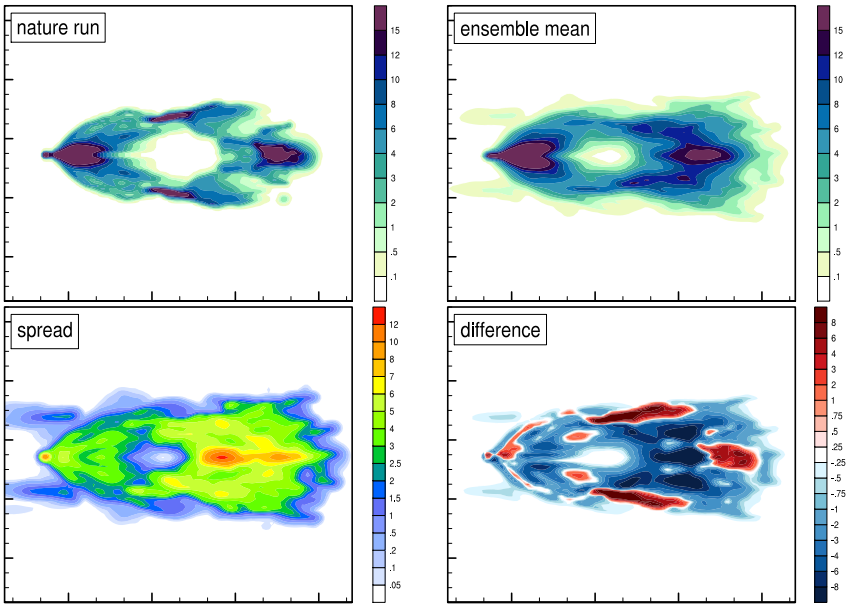


Figure 91: Ensemble ens015. The accumulated surface precipitation in units of $\mathrm{kg\,m^{-2}}$ is plotted in the top left panel for the nature run and in the top right panel for the ensemble mean. The bottom panels exhibit the standard deviation on the left and the differences between the nature run and the ensemble mean on the right (red (blue) colors for larger nature run (ensemble mean) values).

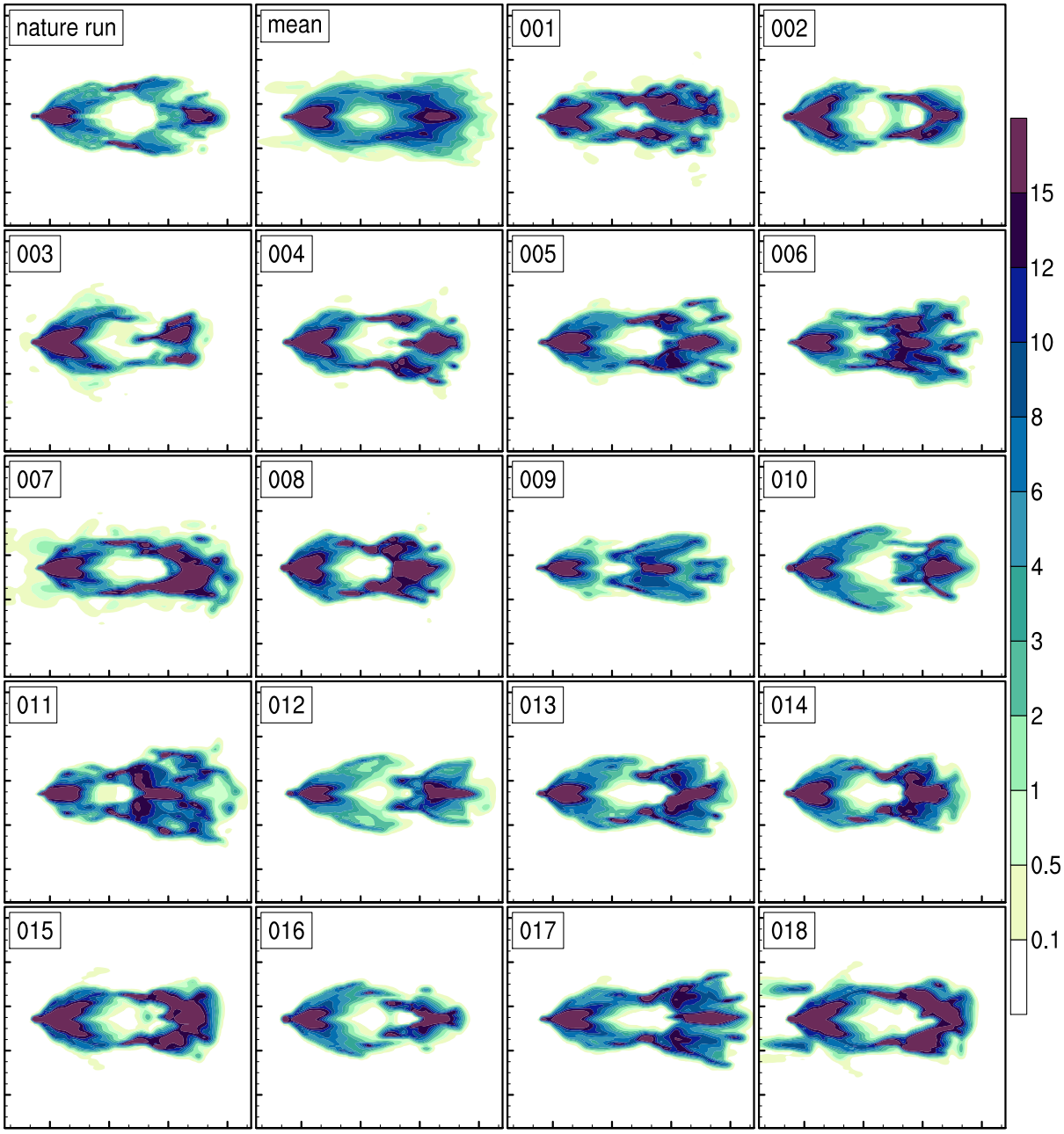


Figure 92: Ensemble ens015. The panels show the accumulated surface precipitation after 5 hours of simulation in units of $\mathrm{kg\,m^{-2}}$ in an area of $75\,\mathrm{km} - 325\,\mathrm{km}$ in x-direction and $50\,\mathrm{km} - 250\,\mathrm{km}$ in y-direction for the nature run, the ensemble mean, and the 18 ensemble members.

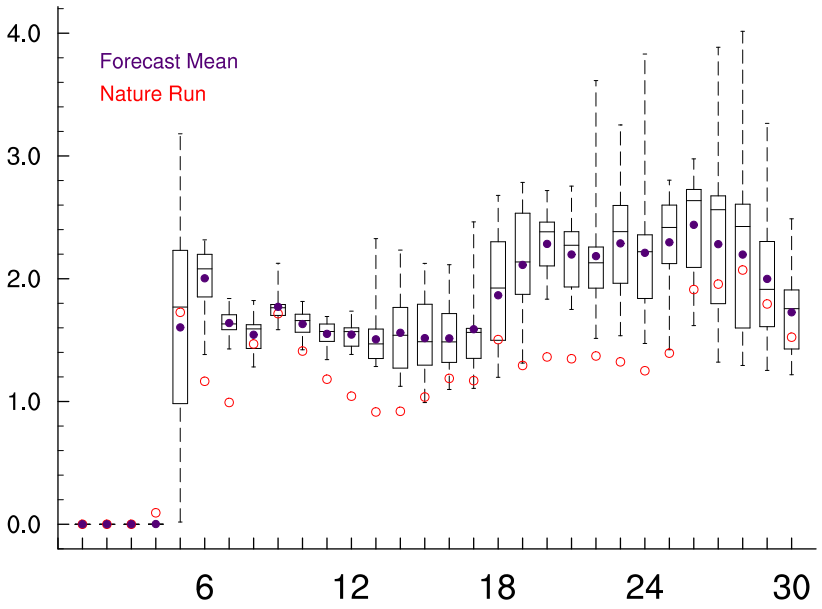


(a) precipitation maxima

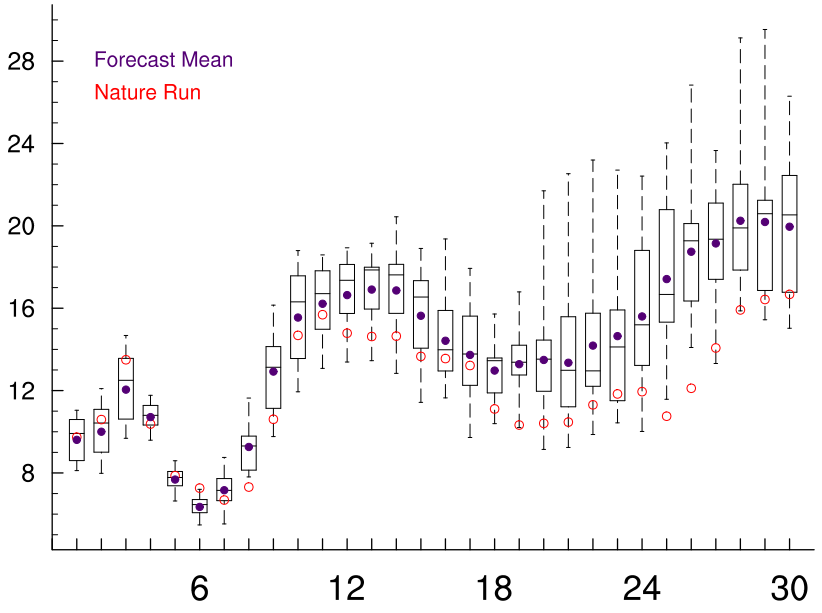


(b) surface wind maxima

Figure 93: Box plot of the precipitating hydrometeors in the lowest level in $\mathrm{g\,kg^{-1}}$ (a) and the surface wind speed maxima in $\mathrm{m\,s^{-1}}$ (b) as a function of time in steps of 10 minutes for the ensemble ens015.

**Veröffentlichungen der MeteoSchweiz**

**86** Walker, D: 2010, Cloud effects on erythemal UV radiation in a complex topography, 106pp, CHF 81.-

**85** Ambühl, J: 2010, Neural interpretation of ECMWF ensemble predictions, 48pp, CHF 68.-

**84** Ambühl, J: 2010, Customer oriented warning systems, 91pp, CHF 78.-

**83** Ceppi, P: 2010, Spatial characteristics of gridded Swiss temperature trends: local and large-scale influences, 82pp, CHF 76.-

**82** Blanc, P: 2009, Ensemble-based uncertainty prediction for deterministic 2 m temperature forecasts, 90pp, CHF 78.-

**81** Erdin R: 2009, Combining rain gauge and radar measurements of a heavy precipitation event over Switzerland: Comparison of geostatistical methods and investigation of important influencing factors, 109pp, CHF 81.-

**80** Buzzi M: 2008, Challenges in Operational Numerical Weather Prediction at High Resolution in Complex Terrain, 186pp, CHF 103.-

**79** Nowak D: 2008, Radiation and clouds: observations and model calculations for Payerne BSRN site, 101pp, CHF 80.-

**78** Arpagaus M, Rotach M, Ambrosetti P, Ament F, Appenzeller C, Bauer H-S, Bouttier F, Buzzi A, Corazza M, Davolio S, Denhard M, Dorninger M, Fontannaz L, Frick J, Fundel F, Germann U, Gorgas T, Grossi G, Hegg C, Hering A, Jaun S, Keil C, Liniger M, Marsigli C, McTaggart-Cowan R, Montani A, Mylne K, Ranzi R, Richard E, Rossa A, Santos-Muñoz D, Schär C, Seity Y, Staudinger M, Stoll M, Vogt S, Volkert H, Walser A, Wang Y, Werhahn J, Wulfmeyer V, Wunram C and Zappa M: 2009, MAP D-PHASE: Demonstrating forecast capabilities for flood events in the Alpine region. Report of the WWRP Forecast Demonstration Project D-PHASE submitted to the WWRP Scientific Steering Committee, 65pp, CHF 73.-

**77** Rossa AM: 2007, MAP-NWS – an Optional EUMETNET Programme in Support of an Optimal Research Programme, 67pp, CHF 73.-

**76** Baggenstos D: 2007, Probabilistic verification of operational monthly temperature forecasts, 52pp, CHF 69.-

**75** Fikke S, Ronsten G, Heimo A, Kunz S, Ostrozlik M, Persson PE, Sabata J, Wareing B, Wichura B, Chum J, Laakso T, Säntti K and Makkonen L: 2007, COST 727: Atmospheric Icing on Structures Measurements and data collection on icing: State of the Art, 110pp, CHF 83.-

**74** Schmutz C, Müller P und Barodte B: 2006, Potenzialabklärung für Public Private Partnership (PPP) bei MeteoSchweiz und armasuisse Immobilien, 82pp, CHF 76.-

**73** Scherrer SC: 2006, Interannual climate variability in the European and Alpine region, 132pp, CHF 86.-

**72** Mathis H: 2005, Impact of Realistic Greenhouse Gas Forcing on Seasonal Forecast Performance, 80pp, CHF 75.-

**71** Leuenberger D: 2005, High-Resolution Radar Rainfall Assimilation: Exploratory Studies with Latent Heat Nudging, 103pp, CHF 81.-

**70** Müller G und Viatte P: 2005, The Swiss Contribution to the Global Atmosphere Watch Programme – Achievements of the First Decade and Future Prospects, 112pp, CHF 83.-

**69** Müller WA: 2004, Analysis and Prediction of the European Winter Climate, 115pp, CHF 34.

**68** Bader S: 2004, Das Schweizer Klima im Trend: Temperatur- und Niederschlagsentwicklung seit 1864, 48pp, CHF 18.-

**Frühere Veröffentlichungen und Arbeitsberichte finden sich unter**
www.meteoschweiz.ch » Forschung » Publikationen

**Arbeitsberichte der MeteoSchweiz**

**235** Weusthoff T: 2011, Weather Type Classification at MeteoSwiss - Introduction of new automatic classification schemes, 38pp, CHF 66.-

**234** Hächler P, Burri K, Dürr B, Gutermann T, Neururer A, Richner H, Werner R: 2011, Der Föhnfall vom 8. Dezember 2006 – Eine Fallstudie, 47pp, CHF 68.-

**233** Wüthrich C, Scherrer S, Begert M, Croci-Maspoli M, Marty C, Seiz G, Foppa N, Konzelmann T, Appenzeller C: 2010, Die langen Schneemessreihen der Schweiz - Eine basisklimatologische Netzanalyse und Bestimmung besonders wertvoller Stationen mit Messbeginn vor 1961, 33pp, CHF 64.-

**232** Willi, M: 2010, Gridding of Daily Sunshine Duration by Combination of Station and Satellite Data, 92pp, CHF 78.-

**231** Scherrer, S: 2010, Die Niederschlagstotalisatoren der Schweiz –Eine basisklimatologische Netzanalyse und Bestimmung besonders wertvoller Stationen, 32pp, CHF 64.-

**230** Michel, D, MW Rotach, R Gehrig, R Vogt: 2010, Experimental investigation of micrometeorological influences on birch pollen emission, 37 pp, CHF 56.-

**229** Philipona R, Levrat G, Romanens G, Jeannet P, Ruffieux D and Calpini B, 2009: Transition from VIZ / Sippicanto ROTRONIC - A new humidity sensor for the SWISS SRS 400 Radiosonde, 37pp, CHF 66.-

**228** MeteoSchweiz: 2009, Klimabericht Kanton Graubünden, 40pp, nur als .pdf erhältlich

**227** MeteoSchweiz, 2009, Basisanalysen ausgewählter klimatologischer Parameter am Standort KKWLeibstadt, 135pp, CHF 88.-

**226** MeteoSchweiz, 2009, Basisanalysen ausgewählter klimatologischer Parameter am Standort KKW Mühleberg, 136pp, CHF 88.-

**225** MeteoSchweiz, 2009, Basisanalysen ausgewählter klimatologischer Parameter am Standort KKW Gösgen, 136 pp, CHF 88.-

**224** MeteoSchweiz, 2009, Basisanalysen ausgewählter klimatologischer Parameter am Standort KKW Beznau, 135pp, CHF 88.-

**223** Dürr B: 2008, Automatisiertes Verfahren zur Bestimmung von Föhn in den Alpentälern, 22pp, CHF 62.-

**222** Schmutz C, Arpagaus M, Clementi L, Frei C, Fukutome S, Germann U, Liniger M und Schacher F: 2008, Meteorologische Ereignisanalyse des Hochwassers 8. bis 9. August 2007, 29pp, CHF 64.-

**221** Frei C, Germann U, Fukutome S und Liniger M: 2008, Möglichkeiten und Grenzen der Niederschlagsanalysen zum Hochwasser 2005, 19pp, CHF 62.-

**220** Ambühl J: 2008, Optimization of Warning Systems based on Economic Criteria, 79pp, CHF 75.-

**219** Ceppi P, Della-Marta PM and Appenzeller C: 2008, Extreme Value Analysis of Wind Observations over Switzerland, 43pp, CHF 67.-

**218** MeteoSchweiz (Hrsg): 2008, Klimaszenarien für die Schweiz – Ein Statusbericht, 50pp, CHF 69.-

**217** Begert M: 2008, Die Repräsentativität der Stationen im Swiss National Basic Climatological Network (Swiss NBCN), 40pp, CHF 66.-

**216** Della-Marta PM, Mathis H, Frei C, Liniger MA and Appenzeller C: 2007, Extreme wind storms over Europe: Statistical Analyses of ERA-40, 80pp, CHF 75.-

**Frühere Veröffentlichungen und Arbeitsberichte finden sich unter**
www.meteoschweiz.ch » Forschung » Publikationen